

Constrained Aerodynamic Optimization of the Flying- V Nose Cone and Center- Body Fairing

Y. Brouwer

Technische Universiteit Delft

Constrained Aerodynamic Optimization of the Flying-V Nose Cone and Center-Body Fairing

by

Y. Brouwer

to obtain the degree of Master of Science at the Delft University of Technology, to be defended
publicly on Thursday April 14, 2022 at 2:00 PM.

Student number : 4488989
Project duration: December 8, 2020 – April 14, 2022
Supervisor: Dr. ir. R. Vos
Thesis committee: Dr. ir. A. Gangoli Rao, TU Delft, Chair
Dr. ir. R. Vos, TU Delft, Supervisor
Dr. ir. S.J. Hulshoff, TU Delft, Examiner

An electronic version of this thesis is available at <http://repository.tudelft.nl/>.

Summary

The unconventional Flying-V aircraft design was developed as an effort to meet the ever-growing demands of the aviation industry, aiming to overcome the plateau in annual fuel consumption reduction. Promising results have already been seen in structural weight, aerodynamic efficiency, high angle-of-attack handling qualities, and noise reduction ascribed to the over-wing installation of the engines.

A nose cone model with interior components was established in a previous effort, together with a center-body trailing edge fairing to reduce the center-body pressure drag seen in the early aerodynamic studies. However, the models proved inadequate in generating designs reliably, hence the need for a redesign. The objective of the study at hand is to establish new parametric models that describe the shapes, perform a drag minimization study at cruise conditions that employs the Reynolds-Averaged Navier-Stokes equations and establish a method that enables such a procedure for graduate projects. In the numerical nose cone optimization, the design space is bound by radar and nose landing gear storage, pilot seating, and windshield size. In addition, the fairing shape is constrained by the size of the galley that it accommodates.

The parametric models are built on the Knowledge Based Engineering platform ParaPy. A total of 24 design parameters are used to design the nose cone shape, and 20 are used for the fairing shape. The parametric models are established in such a way that they can easily be extended with more design variables to increase the complexity of the shapes. The existing Salome-ParaPy interface was extended with the ability to build hybrid meshes that incorporate tetrahedral and prism cells. This allows for spatial discretization suitable for resolving the boundary layer. During the aerodynamic shape optimization, meshes with 5 million cells are used. The optimizer, which employs six processes simultaneously, is coupled with the High Performance Computing 12 cluster at TU Delft to ensure a decrease in computational time for the aerodynamic simulations. In a parallel structure, the computationally costly nose cone constraints are assessed simultaneously with evaluating the forces on the cluster. The fairing constraints are analyzed before calculating the aerodynamic force coefficients.

The aerodynamic shape design is performed at a constant angle-of-attack of 3° , a cruise Mach number of 0.85, and an altitude of 13.000 m. Adding the unoptimized nose cone and fairing shapes increases the drag coefficient by 1.3%. After both optimizations, the drag is reduced by 3.4% compared to the unoptimized design and by 2.1% with respect to the baseline Flying-V. Despite the fact that the shock severity on the center-body is not decreased markedly, the pressure drag sees a significant decrease. Notwithstanding the large curvature of the optimized nose cone, separation is only found on the trailing edge of the optimized shape. The windshield area increases by roughly 50% relative to the windshield of the A350 and the A320.

Preface

Dear reader,

Writing this marks the finish line of my time at the Faculty of Aerospace Engineering at TU Delft. The thesis project that I hereby present has brought me many inspiring moments and unforeseen setbacks. Without the help of great people around me, both academically and personally, I would not have been at the point where I am now; the final project of my master's degree. Going back to the first course of the Flight Performance profile, Advanced Aircraft Design, I already had the opportunity to listen to stories about the Flying-V design process and its features. This inspired me to contact Roelof, who had a project available that fit right up my alley. I want to thank Roelof for the feedback and the brainstorming sessions during our meetings. I have always felt like they were a good mix of discussing academic progress and personal interaction. Moreover, Roelof's feedback at the greenlight review helped a lot with reorienting my focus and knowing what needs to be done to deliver the final product.

I want to thank Ricardo for paving the way for me by doing extensive research in his thesis that I could quickly adopt and for bringing me up to speed on SU2. From then onward, Alexander van Zuijlen helped me to get a general understanding of running aerodynamic analyses at the HPC12 cluster, and I want to thank him for that. I also want to acknowledge Vincent for giving feedback on my code and advancing it by adding parallel computing capabilities. A heavy-duty PC was needed to run the optimizer, for which I need to thank Tomas Sinnige. The computer in his office was of great help during the optimization process. Another person who contributed to the process's smooth running is Akshay Raju Kulkarni. I want to thank him for introducing me to web-hosting ParaPy objects to generate a great number of aircraft designs without a large memory requirement. The last person that I want to thank for his contribution to the computational side of this thesis is Max Baan from ParaPy. He was there a lot at the beginning of my thesis to help with problems experienced with ParaPy. Particularly, our series of meetings to decipher unexpected behavior with generating hybrid meshes was very useful.

Throughout my thesis writing, I have received great help from Nando van Arnhem. I want to thank him for his quick and extensive responses when I had a complicated aerodynamics question. Another person that was always there when I wanted to brainstorm about all things thesis-related is Godert. Special thanks go to him for always being critical, bright, a sparring partner, and good company.

As a final note, I want to thank the people close to me who have been present during the whole process. First, I thank all my friends that were there to listen to my accomplishments and frustrations while trying to drag me out of thesis mode for a night. Second, I want to thank my parents and sister for always being there for me. Even though losses were experienced in the family during the final stages of my thesis, they never failed to keep my spirit high. Finally, I want to thank my loving and caring girlfriend, Tessa. During the whole process, she always believed in me, was there to support me, and projected her abundant love on me. Without the help of all the people mentioned before, academics, friends, family, and girlfriend, I could not have finished the master's thesis. I will, therefore, forever be grateful for them.

*Y.Brouwer
Rotterdam, April 2022*

Contents

Summary	iii
List of Tables	ix
List of Figures	xi
List of Symbols	xiii
List of Abbreviations	xv
List of Subscripts	xvii
1 Introduction	1
1.1 Problem Statement	1
1.2 Research Questions & Objectives	4
1.3 Relevance	5
1.4 Document Outline	5
2 Background	7
2.1 Swept Wing Root Aerodynamics	7
2.1.1 Realigning the Isobars at the Root.	7
2.2 Runway Visual Requirements	8
3 Methodology	11
3.1 Nose Cone and Fairing Parametric Model	11
3.1.1 Nose Cone	11
3.1.2 Fairing.	13
3.2 Design Workflow	14
3.3 Component Repositioning	15
3.4 Optimization Definition	16
3.4.1 Nose Cone Optimization Problem Statement	16
3.4.1.1 Outside View	17
3.4.1.2 Pilot Constraints	18
3.4.1.3 Radar Constraints	18
3.4.1.4 NLG Constraints	19
3.4.2 Fairing Optimization Problem Statement	19
3.4.3 Optimization Algorithm	20
3.5 Aerodynamic Analysis	21
3.5.1 Aerodynamics Solver.	21
3.5.2 Numerical Domain	21
3.5.3 Spatial Discretization	22
4 Verification and Validation	25
4.1 Domain Size	25
4.2 Grid Density Convergence	25
4.3 Boundary Layer Solving	27
4.4 RANS Solver Validation	27
5 Results and Discussion	31
5.1 Design Stages	32
5.2 From Baseline to Unoptimized Design	33
5.3 Windshield Optimization	36
5.4 Nose Cone Optimization	37
5.5 Fairing Optimization	40

5.6	Coupled Performance	40
5.7	Mesh Density Sensitivity	43
6	Conclusions and Recommendations	45
6.1	Recommendations	45
A	Additional Pressure Distributions	47
B	Realistic Windshields	53
	Bibliography	55

List of Tables

2.1	List of modifications to apply to the inboard wing as proposed by Obert.	9
2.2	Approach and ILS categories with corresponding minimal values for RVR, DH and visual segment	9
2.3	The minimal required overnose angles for all bad weather approach categories.	10
4.1	Pitching moment and drag coefficient errors with respect to the force coefficients calculated on a numerical domain with dimensions equal to {4000, 2000, 4000} m with 19.1×10^6 volume elements.	25
5.1	Flight conditions used as inputs for SU2 RANS simulations.	31
5.2	Reference values used throughout the calculations.	31
5.3	Overview of the nose cone design vector of the UO configuration.	32
5.4	Overview of the fairing design vector of the UO configuration.	32
5.5	Overview of the nose cone design vector bounds of the windshield optimization.	32
5.6	Overview of the nose cone design vector bounds of the nose cone optimization.	33
5.7	Overview of the fairing design vector bounds of the fairing optimization.	33
5.8	Comparison of the aerodynamic force coefficients of the baseline, UO and optimized designs. Calculated at $M = 0.85$, $\alpha = 3^\circ$, $Re = 8.4 \times 10^7$	34
5.9	Overview of the nose cone design vectors of the UO and the NCO designs.	36
5.10	Windshield dimensions and pilot view parameters of the different nose cone configurations.	36
5.11	Overview of the fairing design vector of the FO configuration.	40
5.12	Comparison of the aerodynamic force coefficients of the baseline, UO and optimized designs. Calculated at $M = 0.85$, $\alpha = 3^\circ$, $Re = 8.4 \times 10^7$ and a volume mesh with 10 Million cells.	43

List of Figures

1.1	Front view of the conceptual design of the Flying-V aircraft ¹	2
1.2	Example of a minimal required windshield and a realistic windshield, which are modeled using the method from section 3.2.1 from van der Pluijm.	3
1.3	Cross-section of the conceptual FV wing root, including nose cone, cockpit interior components and center-body galley ²	3
2.1	Isobars on finite swept wings. The dotted lines depict the isobars according to the simple sweep theory and the solid lines are the actual isobars.	8
2.2	Drawing of the definitions needed for determining the required overnose angle.	10
3.1	Overview of the parameterization steps performed to generate the nose cone geometry.	12
3.2	Overview of the parameterization steps performed to generate the fairing geometry.	13
3.3	Workflow diagram of the nose cone optimization.	14
3.4	Workflow diagram of one function evaluation in the fairing optimization.	16
3.5	Workflow diagram of the repositioning of the radar, NLG and pilots.	16
3.6	Visualization of the repositioning of the radar, NLG and pilot including margins.	17
3.7	Floor plan of the FV with trapezoidal cabin. The colored regions denote parts of the galley that are affected by the constraints.	20
3.8	Visualization of the numerical domain, including dimensions and boundary conditions.	22
3.9	Example of required domain size study using the method of van Arnhem et al.	22
3.10	Visualization of the eddy viscosity ratio at the trailing edge of the wing root.	23
3.11	Detail of the inflation layer around the aircraft geometry and the interface between the prisms and the tetrahedrons.	24
4.1	Variation of the aerodynamic force coefficients with respect to varying mesh triangle and tetrahedron sizes and number of mesh cells.	26
4.2	Comparison of pressure distributions between surface meshes with 0.14 m and 0.10 m maximum triangle sizes.	27
4.3	Overview of the distribution of the first layer height with histogram and detail of trailing edge at outboard wing.	28
4.4	Error with respect to the smallest recorded growth factor. Throughout the evaluations, n_{layer} is allowed to vary and the total thickness of 25 cm is kept constant.	28
4.5	Pressure distributions of the SU2 RANS validation study using the ONERA M6 wing geometry.	29
4.5	Pressure distributions of the SU2 RANS validation study using the ONERA M6 wing geometry.	30
5.1	Comparison of the baseline, UO and optimized designs upper surface pressure distribution. Calculated at $M = 0.85$, $\alpha = 3^\circ$, $Re = 8.4 \times 10^7$. $C_p^* = -0.3$	34
5.2	Pressure distributions of baseline design and UO design at two spanwise stations. Calculated at $M = 0.85$, $\alpha = 3^\circ$, $Re = 8.4 \times 10^7$. $C_p^* = -0.3$	35
5.3	Upper surface skin friction coefficients of baseline design and UO design at two spanwise stations. Calculated at $M = 0.85$, $\alpha = 3^\circ$, $Re = 8.4 \times 10^7$	35
5.4	Comparison of the pressure distributions of the three nose cone designs. Calculated at $M = 0.85$, $\alpha = 3^\circ$, $Re = 8.4 \times 10^7$. $C_p^* = -0.3$	37
5.5	Pressure distributions of UO, WO and NCO designs at different spanwise stations. Calculated at $M = 0.85$, $\alpha = 3^\circ$, $Re = 8.4 \times 10^7$. $C_p^* = -0.3$	38
5.6	Upper surface skin friction coefficients of UO, WO and NCO designs at two spanwise stations. Calculated at $M = 0.85$, $\alpha = 3^\circ$, $Re = 8.4 \times 10^7$	38

5.7	Overview of three different nose cone configurations.	39
5.8	Pressure distributions of UO and FO designs at two spanwise stations. Calculated at $M = 0.85$, $\alpha = 3^\circ$, $Re = 8.4 \times 10^7$. $C_p^* = -0.3$	41
5.9	Upper surface skin friction coefficients of UO and FO designs at two spanwise stations. Calculated at $M = 0.85$, $\alpha = 3^\circ$, $Re = 8.4 \times 10^7$	41
5.10	Pressure distributions of CO, WO and NCO designs at two different spanwise stations. Calculated at $M = 0.85$, $\alpha = 3^\circ$, $Re = 8.4 \times 10^7$. $C_p^* = -0.3$	42
5.11	Upper surface skin friction coefficients of CO, WO and NCO designs at two spanwise stations. Calculated at $M = 0.85$, $\alpha = 3^\circ$, $Re = 8.4 \times 10^7$	42
5.12	Pressure distributions of CO design with comparison of coarse and fine mesh. Calculated at $M = 0.85$, $\alpha = 3^\circ$, $Re = 8.4 \times 10^7$ and $S_{ref} = 398 \text{ m}^2$. $C_p^* = -0.3$	43
A.1	Pressure distributions of baseline design and UO design at different spanwise stations. Calculated at $M = 0.85$, $\alpha = 3^\circ$, $Re = 8.4 \times 10^7$. $C_p^* = -0.3$	48
A.2	Pressure distributions of UO, WO and NCO designs at different spanwise stations. Calculated at $M = 0.85$, $\alpha = 3^\circ$, $Re = 8.4 \times 10^7$. $C_p^* = -0.3$	49
A.3	Pressure distributions of UO and FO designs at different spanwise stations. Calculated at $M = 0.85$, $\alpha = 3^\circ$, $Re = 8.4 \times 10^7$. $C_p^* = -0.3$	50
A.4	Pressure distributions of CO, WO and NCO designs at different spanwise stations. Calculated at $M = 0.85$, $\alpha = 3^\circ$, $Re = 8.4 \times 10^7$. $C_p^* = -0.3$	51
A.5	Pressure distributions of CO design with comparison of coarse and fine mesh. Calculated at $M = 0.85$, $\alpha = 3^\circ$, $Re = 8.4 \times 10^7$ and $S_{ref} = 398 \text{ m}^2$. $C_p^* = -0.3$	52
B.1	Picture of UO cockpit layout with realistic windshield.	53
B.2	Picture of WO cockpit layout with realistic windshield.	54
B.3	Picture of NCO cockpit layout with realistic windshield.	54

List of Symbols

Latin Symbol	Description	Unit
A_{WS}	Windshield area	(m ²)
C_D	Drag coefficient	(-)
C_{Dp}	Pressure drag coefficient	(-)
C_{Df}	Friction drag coefficient	(-)
C_L	Lift coefficient	(-)
C_m	Pitching moment coefficient	(-)
C_p	Pressure coefficient	(-)
C_p^*	Critical pressure coefficient	(-)
$f(\vec{X})$	Objective function	(-)
$g(\vec{X})$	Inequality constraint	(-)
$h(\vec{X})$	Equality constraint	(-)
h_{eye}	Design eye point height	(m)
h_{ON}	Overnose windshield pane height	(m)
L/D	Lift-to-drag ratio	(-)
l_{VP}	Viewpoint distance	(m)
M	Mach number	(-)
n_{layer}	Number of prism layers	(-)
P	Pressure	(Pa)
Re	Reynolds number	(-)
S_{ref}	Reference area	(m ²)
S_{wet}	Wetted area	(m ²)
T	Temperature	(K)
v	Calibrated airspeed	(m/s)
V	Volume	(kg/m ³)
\vec{X}	Design vector	(-)
\vec{X}_0	Initial guess of design vector	(-)
x_{CG}	x -position of center of gravity	(m)
x_{CoP}	x -position of center of pressure	(m)
x/c	Chordwise position	(-)
y^+	First cell width	(-)

Greek Symbol	Description	Unit
α	Angle-of-attack	(deg)
$\alpha_{approach}$	Approach angle-of-attack	(deg)
$\alpha_{overnose}$	Over-the-nose angle	(deg)
β	Angle-of-sideslip	(deg)
δ_{99}	99% boundary layer thickness	(m)
ϵ	Error	(%)
η	Spanwise station	(-)
μ	Viscosity	(kg/m/s)
ρ	Density	(kg/m ³)
σ	Standard deviation	(-)
ϕ_{ON}	Overnose angle	(deg)
ϕ_{VP}	Viewpoint angle	(deg)

List of Abbreviations

Abbreviation	Description
AoA	Angle-of-Attack
BL	Boundary Layer
BWB	Blended-Wing-Body
CO	Combined Optimized shapes
CFD	Computational Fluid Dynamics
CST	Class-Shape Transformation
DE	Differential Evolution
DEP	Design Eye Point
DH	Decision Height
EA	Evolutionary Algorithm
EASA	European Union Aviation Safety Agency
FAA	Federal Aviation Administration
FO	Fairing Optimized
FPB	Front Pressure Bulkhead
FV	Flying-V
FW	Flying Wing
HPC	High Performance Computing
HSS	HalfSpaceSolid
ILS	Instrument Landing System
JST	Jameson-Schmidt-Turkel Method
KBE	Knowledge-Based Engineering
NCO	Nose Cone Optimized
NLG	Nose landing gear
OML	Outer Mold Line
PDE	Partial Differential Equation
RANS	Reynolds-Averaged Navier-Stokes
RVR	Runway Visual Range
SA	Spalart-Allmaras
SU2	Stanford University Unstructured
UO	Unoptimized
VS	Visual Segment
WO	Windshield Optimized

List of Subscripts

Subscript	Description
F	Fairing
HSS	HalfSpaceSolid
l	Lower
min	Minimal
NC	Nose cone
NLG	Nose landing gear
real	Realistic
TE	Trailing edge
u	Upper
VP	Viewpoint
∞	Freestream

Introduction

From the advent of the B-47 bomber until present day, swept-wing aircraft design has been drawn towards the usage of “tube-and-wing” configurations [1]. Over time, innovations for each of the disciplines that come together in an aircraft design reduced the fuel consumption of typical transonic aircraft by 100% [2]. Despite the increasing importance of restrictions on aircraft emissions and noise pollution as well as the increase in commercial aviation industry [2], yearly fuel reduction has reached a plateau [3]. Therefore, to comply with future needs of airliners, a momentous change has to happen in aircraft design.

An opportunity for decreasing fuel consumption can be found in the concepts of flying wings (FWs) and blended-wing-bodies (BWBs). FWs have been a part of aircraft design for more than a century; the first true FW design being accredited to Igo Etrich in 1909 [4]. Pioneers, like Junkers in 1910, already saw the potential for tailless aircraft that omit the use of large non-lifting tubular bodies. A variety of military FWs have been designed by the Horten brothers, Lippisch, von Kármán and Northrop [4, 5] throughout aviation history until the B-2 bomber in 1988. Despite the advantages, FWs are not regarded as a conventional design today [6], as challenges kept arising that prevented FWs from making it to the drawing board for transport aircraft.

In 1988, the interest in long-haul aircraft was sparked by Dennis Bushnell at the NASA Langley Research Center [1]. This invoked a series of efforts at McDonnell Douglas on a large passenger aircraft BWB [1, 7, 8]. Not only did the pioneers envision these unconventional configurations to be prominent in very large transports in the future [9–11], they also saw the potential for BWB and FW transport aircraft with a passenger number equal to today’s wide-body aircraft, because of their fuel efficiency, reduced wetted area for equal payload and favorable structural weight [2, 12–15].

Benad [16] came up with a new pure flying wing design at the Technische Universität Berlin, as part of a design exercise posed by the Future Project Office at Airbus GmbH. His flying wing design was named the Flying-V (FV). The research by Benad was taken on by Roelof Vos’ team at TU Delft. In a series of efforts, a parametric model of the aircraft was conceived [17], the planform was optimized [3, 18, 19], the structural design was performed [20], aerodynamic studies of the flow over the Flying-V have been conducted [21–23] and wind tunnel tests [24–29] were conducted. Figure 1.1 is an excerpt from recent renderings of the aircraft concept. By no means is this the exact geometry of the parametric model, but an adequate representation of the main features is present.

1.1. Problem Statement

The current state of the FV aircraft is that of an FW aircraft without the incorporation of a feasible nose cone shape that is able to accommodate a pilot and a copilot, hereafter denoted by ‘pilots’, the nose landing gear (NLG) and weather radar. In order to add to the complexity of the current design and progress towards a more accurate representation of the FV aircraft, a nose cone that can house the aforementioned components and is aerodynamically favorable has to be designed. Van der Pluijm [30] instituted a parametric model of the outer geometry of the nose cone as well as models for the interior cockpit components that are incorporated within the geometry. However, the parametric model by van der Pluijm suffered from large oscillations in the polynomials that described the geometry, resulting in

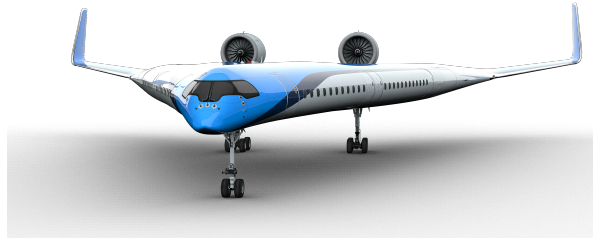


Figure 1.1: Front view of the conceptual design of the Flying-V aircraft¹.

a largely infeasible design space, as can be seen in Appendix E from his report. In order to facilitate aerodynamic shape optimization, in this study, a nose cone parametric model needs to be established with increased robustness.

Van der Pluijm [30] provides a method to model the minimum required windshield shape. This windshield is based on the following requirements:

- The pilots should have a sufficient view of the surroundings, during taxiing, takeoff, approach and landing, but also cruise flight. This is called the compartment view. The angles from the design eye point (DEP), which is the location of the assumed pilot's eye, are taken from U.S. Federal Aviation Administration (FAA) AC 25.773-1 [31] recommendations. The European Union Aviation Safety Agency (EASA) recommends the same standards [32].
- The windshield should provide for sufficient overnose view to adhere to approach requirements. The FV aircraft should be able to perform bad weather approaches up until CAT IIIA. These exact nature of these requirements is outlined in section 2.2. The part of the windshield that is strictly needed to acquire the overnose view, is denoted by the overnose windshield pane.
- The overnose angle needs to be guaranteed at sideslip angles according to recommendations from EASA in CS 25.177(c) [32]. Therefore, the overnose windshield pane needs to have sufficient lateral width.

An example of the minimal windshield from van der Pluijm's method [30] is depicted in Figure 1.2a. The area of this minimal windshield is denoted as A_{WS} . An additional windshield requirement from CS 25.775(b) and (c) regulations [32] states that the windshield should not be penetrable at birdstrike, nor should the pilots be endangered by any fragments of shattered glass. To minimize the possibility of these events, at this stage of the design, A_{WS} should be minimized. An actual structural assessment of the compliance with these regulations is beyond the scope of this study. Moreover, in Figure 1.2a the parameter h_{ON} is drawn. It denotes the overnose windshield pane height and is measured by the difference between the maximum and minimum z -coordinate of the most inboard edge of the pane. To prevent limiting the design space of the cockpit interior largely, h_{ON} should also be minimized to ensure that the overnose windshield pane does not reach under the dashboard, which would render it unusable. For the sake of brevity, the combination of h_{ON} and A_{WS} are indicated throughout this report as the 'windshield dimensions'. Apart from a minimal windshield, he also built a module to calculate a realistic windshield. This shape is used in this report to compare the resulting geometry to reference aircraft. Figure 1.2b portrays an example of such a windshield.

Two previously established principles form the basis for improving the root aerodynamics of the FV. It was already established by Faggiano et al. [3] that the flow on the rear end of the center-body caused an increase in pressure drag, which is an artifact of the pressure distribution on the root of swept wings. A more detailed explanation of this phenomenon is given in section 2.1. Furthermore, it was also shown that an inboard shockwave occurred at the wing root. Therefore, apart from optimizing the aerodynamic shape of the front of the center-body by altering the nose cone, the downstream center-body also requires improvement. Van der Pluijm [30] established a parametric model of a center-body trailing edge fairing that can be used to alleviate the aforementioned phenomena. The parametrized fairing model of van der Pluijm suffered from the same aforementioned oscillations. Again, the reader

¹Render by E. Wallet. <https://www.tudelft.nl/lr/flying-v/>. (Accessed on 04/12/2020).

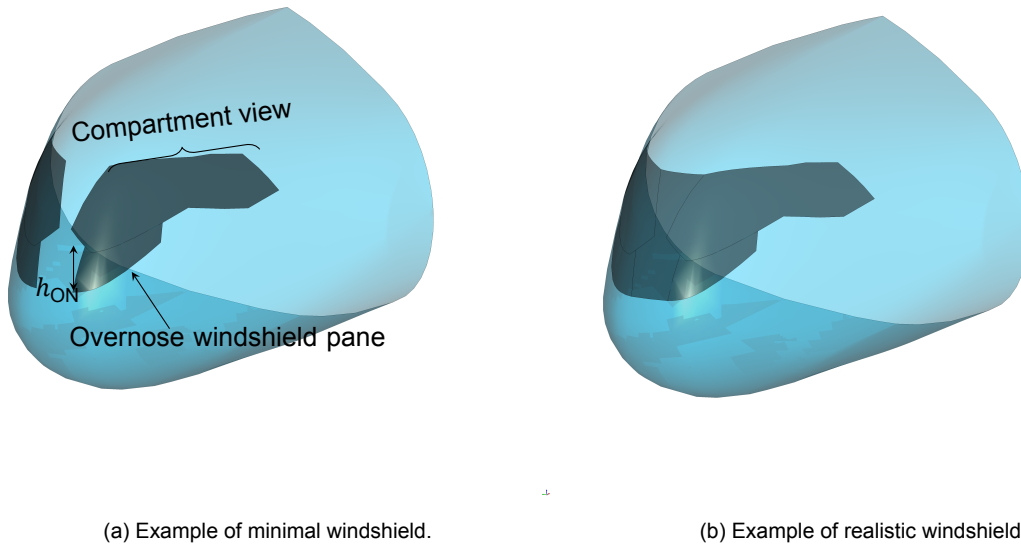


Figure 1.2: Example of a minimal windshield and a realistic windshield, which are modeled using the method from section 3.2.1 from van der Pluijm [30].

can refer to Appendix E of his work for a sample from the design space. To allow for aerodynamic shape optimization and thereby improving the rear center-body aerodynamics, an improved fairing parametric model that generates feasible designs for a larger part of the design space has to be established in this study.

A requirement that was not introduced by van der Pluijm [30] is the inclusion of a galley in part of the fairing. The center-body accommodates a galley, which can be seen in the cross-section at the FV wing root in Figure 1.3. The fairing should therefore be shaped in such a way that sufficient headroom is available both for the flight crew and the galley carts. The exact nature of the corresponding design requirements is elaborated in section 3.4.

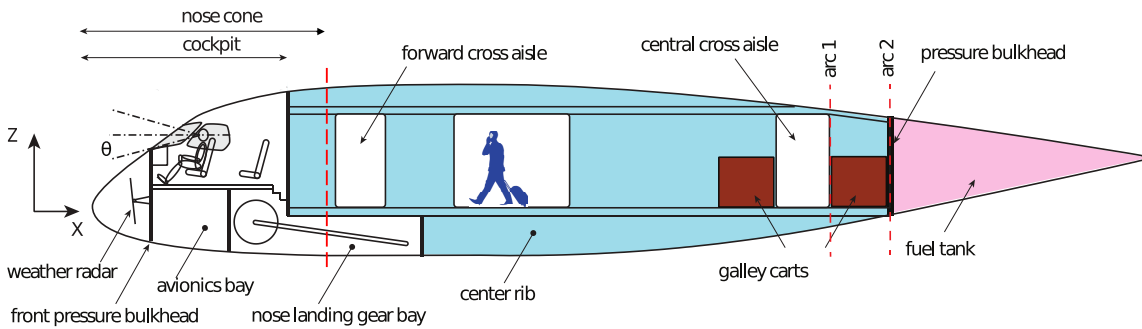


Figure 1.3: Cross-section of the conceptual FV wing root, including nose cone, cockpit interior components and center-body galley².

From the artistic mockup and the previous work done by van der Pluijm [30] on the nose cone it can be seen that to comply with the constraints, the crown, which denotes upper curved part of the nose cone, could potentially be highly curved. Therefore, it can be hypothesized that the overspeeds that correspond to the high curvature potentially terminate in a shock wave which causes shock-induced

²Modified from graphic by R. Vos. (Acquired on 28/03/2020).

boundary layer separation. Furthermore, the fairing is added to the aircraft to alleviate the center-body pressure drag and reduce the shock strength. Consequently, it is deemed a requirement to accurately map the shockwaves that occur on the wing. Moreover, behind the shock, the viscous, slow flow close to the wing surface, denoted by the boundary layer, thickens. To accurately estimate the effect of altering the shock location, the decambering effect of the thick boundary layer behind it should be taken into consideration. The Reynolds-Averaged Navier-Stokes (RANS) equations model viscosity and therefore the boundary layer. Additionally, the inclusion of the boundary layer allows for separation modeling, as opposed to the Euler equations used in the optimization by Faggiano [3]. Accordingly, the RANS method is selected for the numerical optimizations in this study.

1.2. Research Questions & Objectives

Based on the problem statement, the main research objective is derived, which reads:

“To design a nose cone and a center-body trailing edge fairing by performing an aerodynamic optimization that includes a RANS solver and an automated unstructured mesher, bounded by pilot visibility, radar- and nose gear storage, and galley dimensions.”

From the main objective, a set of sub-objectives can be extracted. These are as follows:

- To establish a parametric model that describes an arbitrary nose cone design.
- To establish a parametric model that describes an arbitrary fairing design.
- To couple the FV geometric model with an automated mesher that generates RANS-compatible grids.
- To institute a design method that enables the use of RANS equations.
- To design a nose cone by performing a numerical optimization.
- To design a fairing by performing a numerical optimization.

The objectives stated above correspond to the research question that is answered in the present study:

“What is the optimal shape of the Flying-V nose cone and fairing that minimizes aerodynamic drag, while complying with all requirements on pilot visibility, nose landing gear- and radar storage, and galley dimensions?”

In turn, the main research question can also be subdivided into a variety of questions that are assessed in this report. These sub-questions are as shown below:

- Are the RANS equations feasible for use in shape optimization for graduate student studies on the FV geometry?
- How can the nose cone geometry be parametrized?
- How can the fairing geometry be parametrized?
- What cockpit requirements concerning pilot visibility and radar- and NLG storage influence the nose cone shape?
- What center-body galley requirements influence the fairing shape?
- What is the optimal nose cone shape, disregarding the aerodynamics?
- What nose cone shape minimizes the drag coefficient while complying with all requirements and limiting the windshield dimensions?
- What fairing shape minimizes the drag coefficient, while complying with all requirements?

Utilizing these research objectives and questions, the problem posed in section 1.1 is addressed and a greater understanding of the nose cone and fairing shape needs is created.

1.3. Relevance

The study at hand provides an insight into the change of the aerodynamics when a representative nose cone that complies with all cockpit requirements is added to the existing geometry from Oosterom [19]. The parametric model established for the nose cone is added to the overall FV geometric model, which enables the future evolution of its shape. Moreover, a shape that can be used to decrease the center-body pressure drag in future research is constructed and parametrized, which prepares the FV for further reductions in the drag coefficient at design iterations hereafter.

Furthermore, establishing a method that enables the use of the RANS equations reinforces the development of the entire FV project. Using RANS, aerodynamic optimizations with higher fidelity than previously done can be performed. The inclusion of the boundary layer adds to the accuracy and predictability of the aerodynamic force coefficients used as figures of merit in the shape optimization and therefore the design state of the FV.

Finally, as was previously mentioned in the thesis report of van der Pluijm [30], the aerodynamic optimization of a nose cone shape and the simultaneous arrangement of an adequate cockpit interior cannot be found in current literature. The combination of the procedures that are seen in this study adds to the body of knowledge regarding transonic nose cone and cockpit design.

1.4. Document Outline

In the remainder of the report, the research questions are answered. To provide the reader with a sufficient basis to understand the concepts that are fundamental to the method used and the interpretation of the results, required precognition is presented in chapter 2. The method that is used to answer the questions is outlined in chapter 3. The parametric models of both the nose cone and the fairing shapes are discussed, as well as the design workflow, the mathematical optimization statement, and the aerodynamic analysis. Subsequently, the verification and validation of the aerodynamic analysis module are shown in chapter 4, after which the designs of the nose cone and fairing are presented and the aerodynamics thereof are discussed in chapter 5. Finally, the answers to the research questions are summarized in chapter 6, as well as recommendations for future research regarding the center-body shape of the FV.

2

Background

This chapter serves to provide the reader with helpful background theory used to assess nose cone and center-body design features. To begin with, a short introduction to aerodynamics at the wing root for swept-wing aircraft and example modifications to overcome this are given in section 2.1. After this, the recommendations from regulatory authorities at the approach flight phase and their implications on the overnose angle that needs to be cut out by the windshield are presented in section 2.2.

2.1. Swept Wing Root Aerodynamics

This section provides the reader with background on the aerodynamic implications inherent to finite swept wings. However, to understand these effects, theoretically infinite sheared wings need to be understood. According to Vos and Farokhi [33], on an infinite wing, the isobars are parallel to the leading edge of the wing. This means that the isobars are swept as well, as shown by the dotted lines in Figure 2.1. The swept isobars can be explained using simple sweep theory. According to this theory, the flow velocity at the leading edge of an infinite swept wing can be decomposed into a perpendicular component, v_{\perp} , and a component parallel to the leading edge, v_{\parallel} . The parallel component stays aligned with the leading edge and does not cross the wing. The perpendicular component crosses the wing orthogonally to the leading edge. This streamline component sees the curvature and contributes to the wing's pressure distribution.

On a finite wing, however, for the symmetry between the pressure distributions on the port and starboard wings to hold, the streamline on the root should not experience any pressure gradient that deviates from the freestream direction [33]. This can only hold when the isobars at the root are perpendicular to the freestream velocity, similar to the isobars seen on a straight wing. This means that the swept isobars from the majority of the wing must join with the unswept inboard isobars at the root. These curved isobars can be seen as the solid lines at the root of the wing in Figure 2.1.

Vos and Farokhi [33] indicate a variety of disadvantageous aerodynamic properties connected to the aft-curving of the isobars at the wing root. These are as follows:

- The suction peak is shifted aft, and the overall suction is concentrated around the rear part of the section. This results in a net drag on the wing.
- The magnitude of the suction peak is decreased.
- The shock occurs more aft as overspeeds are higher at the rear root airfoil than at mid-semispan stations.
- A steeper adverse pressure gradient occurs behind the shock.

2.1.1. Realigning the Isobars at the Root

Swept wing roots can be modified to match the pressure distribution at the wing root with the rest of the wing to improve the aerodynamic predictability and reduce the pressure drag at the root. In a series of efforts by Küchemann and Weber [34–36], a variety of wing root geometries were experimentally

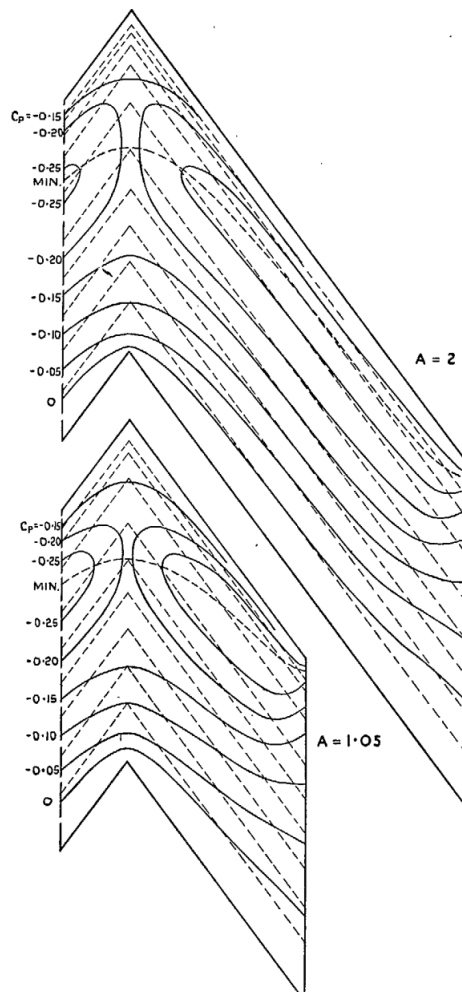


Figure 2.1: Isobars on finite swept wings. The dotted lines depict the isobars according to the simple sweep theory and the solid lines are the actual isobars [34].

assessed. As a result, it was shown that to match the zero-lift pressure distribution at the wing root with the mid-semispan, the thickness of the front part of the airfoil had to be increased, to shift the suction peak forward. Furthermore, the thickness of the rear of the airfoil had to be decreased, to relieve the aft loading. These modifications improve the velocity distribution due to thickness.

The modifications as mentioned above were only applicable at maximum AoAs of 4° [36]. To improve the pressure distribution at the root at higher AoAs, the so-called velocity distribution due to lift needs improvement [33]. Küchemann [35] showed that increasing the incidence angle of the leading edge and applying negative camber to the wing section resulted in a good resemblance between mid-semispan and root wing sections.

Obert [37] summarizes the findings that improve the wing root pressure distribution. He proposes the use of these guidelines until 30-40% semispan. The modifications are tabulated in Table 2.1.

2.2. Runway Visual Requirements

During the approach maneuver, pilots need to acquire a sufficient view of the runway to proceed to land. The description of the requirements is given in AMC1 SPO.OP.215 recommendations by EASA [38]. The relation between approach requirements and the overnose viewing angle has been described in section 3.2.1 in the thesis work by van der Pluijm [30] already. However, in this report, a revised strategy is presented.

In bad weather conditions, fog or precipitation can limit the range of pilots' visibility. The runway visual range (RVR) is the distance over which a pilot on the centerline can see the runway light. De-

Table 2.1: List of modifications to apply to the inboard wing as proposed by Obert [37].

Modification	Reason
Increase the thickness of the forward root section and decrease the thickness of the rear root section	To obtain similar chordwise upper-surface pressure distributions due to thickness along the span
Increase the thickness-to-chord-ratio of the root section	To obtain identical chordwise upper-surface pressure distributions due to thickness along the span
Decrease positive camber or apply negative camber on the root section	To adapt the pattern of the chordwise upper-surface pressure distribution due to lift to that of the basic airfoil section
Increase the incidence of the root section	To obtain identical chordwise upper-surface pressure distributions due to lift along the span

pending on the magnitude of the RVR, different Instrument Landing Systems (ILS) need to be used. ILSs exist in three categories, CAT I, CAT II, and CAT III, where the latter can be subdivided into IIIA, IIIB, and IIIC. Depending on the RVR measured on the runway, the pilots must use a specified ILS [39]. The approach categories and the corresponding RVRs are tabulated in Table 2.2.

Table 2.2: Approach and ILS categories with corresponding minimal values for RVR, DH and visual segment

Category	RVR (m)	DH (m)	Visual reference	Visual segment (m)
I	550	60	Any light or marking on the runway	0
II	300	30	Three consecutive centerline lights	45
IIIA	175	<30 or no DH	Three consecutive centerline lights	45
IIIB	50	<15 or no DH	One centerline light	15

Depending on the type of ILS, a certain Decision Height (DH) is allowed. The decision height is the altitude at which a certain number of visual references should be visible, and the magnitudes that correspond to the different approach categories can be seen in Table 2.2. If the pilots cannot see the prescribed visual references, they decide to perform a go-around or land elsewhere. In the foggiest situations, where CAT IIIA and CAT IIIB are appropriate, it is allowed to have zero DH. DH is measured from the lowest point of the aircraft to the runway.

The visual segment (VS) can be deduced based on the visual references required to land. The visual segment is the length on the runway that the pilots need to be able to see to acquire the visual reference at DH. It can be seen that the visual segment is limited by the RVR and the blind area looking at Figure 2.2. The blind area is the part of the external view that is cut off by the aircraft's nose. Under the assumption that the centerline lights have a 15 m spacing in between them and that in order to always have one light in sight, a minimum of an entire 15 m segment needs to be visible, the visual segment lengths are added to Table 2.2. As for CAT I approaches, anything on the runway counts as a visual reference, the required visual segment is assumed to be zero. Furthermore, CAT I approaches are not limiting the overnose angle design when increasing the visual segment length.

To calculate the required overnose angle for each of the ILSs, the landing AoA has to be determined. The approach lift coefficient, $C_{L_{app}}$ is taken from Oosterom [19] to be equal to 0.73. This value is found to occur at 15.4° in the lift curve from the flight test [40]. Assuming a glideslope of 3° , the required pitch angle, θ at approach, equals 12.4° .

It can be derived from the graph in Figure 2.2 that the overnose angle can be calculated using Equation 2.1:

$$\phi_{ON} = \theta + \tan^{-1} \left(\frac{h_{eye}}{RVR - VS} \right) \quad (2.1)$$

In this equation ϕ_{ON} is the overnose angle h_{eye} is the height of the DEP. This value is the sum of the contributions of DH, the size of the main landing gear that determines the lowest point of the aircraft, from which the DH is measured, and the pilot seating height. The method for calculating these

quantities is taken from section 3.2.1 in the report by van der Pluijm [30] and depends mainly on the pitch angle. The values used in this study are 12.5 m from the main gear to the pilot seat and 1.1 m from the pilot seat to the DEP.

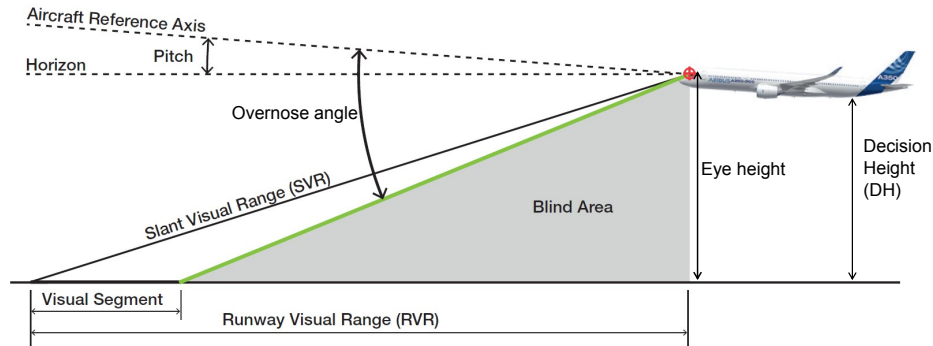


Figure 2.2: Drawing of the definitions needed to determine the required overnose angle [41].

The overnose angle is calculated using the acquired values from Table 2.2 and the relation in Equation 2.1. The minimal required overnose angles that correspond to the bad weather approaches are tabulated in Table 2.3. These values are based on the minimal RVR that can be flown with the ILSs, as air traffic control allows landing at that minimal RVR with the corresponding ILS. A DH of 15 m is assumed to allow for a decision before the flare maneuver is initiated. The flaring maneuver is potentially added in future research¹.

Table 2.3: The minimal required overnose angles for all bad weather approach categories.

Approach	Required overnose angle (deg)
CAT I	21.6
CAT II	22.3
CAT IIIA	25.1
CAT IIIB	52.3

As per the requirements in section 1.1 it is stated that the aircraft should comply with requirements for ILSs up until CAT IIIA. It can therefore be seen that the ϕ_{ON} at CAT IIIB is not limiting in this design case. As the lift curve from the flight test [40] is recorded in untrimmed flight, it is expected that the actual lift curve in trimmed flight is flatter. Using the governing ϕ_{ON} for CAT IIIA ILS in Table 2.3 together with added leeway, the design overnose angle is equal to 26°.

¹Personal correspondence with R. Vos on 10/02/2022.

3

Methodology

This chapter serves as a presentation of the method employed to reach an optimal design for the nose cone and the fairing. A parametric model of the FV geometry has already been established in previous studies. This representation of the aircraft was built on the ParaPy platform [42]. ParaPy, being a library for Python, offers its users the possibility to build Knowledge Based Engineering (KBE) applications and provides them with a variety of pre-built classes representing often-needed geometry. Particularly interesting for the research at hand is the API for Salome Mesh [43] which allows for automatic unstructured mesh generation and the ability to build interfaces with the Stanford University Unstructured (SU2) aerodynamic solver [44]. These virtues of the KBE platform are of importance for numerical optimization. The addition of the nose cone and fairing to the current aircraft parametric model is presented in section 3.1. Subsequently, the design workflow of the numerical optimization is outlined in section 3.2. section 3.3 briefly states how the radar, NLG, and the pilots, are repositioned at their optimal position during each function evaluation in section 3.3. The formal optimization statement for both of the components, as well as the choice of optimization algorithm in section 3.4. The section concludes with an overview of the aerodynamic method and all decisions that were made regarding the spatial discretization and the numerical setup in section 3.5.

3.1. Nose Cone and Fairing Parametric Model

The parametric models for the nose cone and fairing are presented in this section. Both shapes rely on the same principles and ParaPy classes. Detailed insight in the theory behind the native ParaPy classes used in this study is deemed beyond the scope of this report.

3.1.1. Nose Cone

In the remainder of the text, the term nose cone is used consistently to denote the aerodynamic shape and cockpit is used to indicate the internal shape with radome and pilot seating. The same methods as those described in section 3.1.1 of van der Pluijm [30] are used in this report to cut part of the wing out to create space for the nose cone. The nose cone is then attached to the resulting wing geometry. Both the nose cone's starboard- and port halves are attached to the wing, perpendicular to the cabin. This ensures ease of integration into the existing aircraft geometry and provides the possibility to manufacture the cabin with straight ends, as was intended by Hillen [17].

A successful parametric model should generate non-erratic designs for most of the design space. Furthermore, it should not rely on mathematical relations that manifest as large fluctuations in the geometry for some design vectors. However, it should still provide the user with sufficient design freedom to arrive at the optimal geometry. With this notion, a method was conceived to parameterize the nose cone, which is similar to the CST method [45], which is widely applied to parameterize airfoils. The CST method is based on the tuning of the Bernstein coefficients. However, unlike the parameters that Faggiano et al. [3] and Hillen [17] used in their parameterization of the FV planform, CST coefficients do not bear any physical meaning. They are merely dimensionless factors to change the airfoil contour.

For the parameterization of the nose cone in this report a linear combination of B-splines is used, because, in contrary to the CST method, a nose cone shape could be generated with a smaller amount

of design variables. ParaPy has a native class dedicated to the generation of these `BSplineCurves`. The curves start and end in allocated points but tend towards the control points in between, rather than being forced through them. This ensures that the curves allow for generating complex shapes while avoiding large convex and concave structures that are prevalent when forcing the curves through points.

The basis for the parametric model is formed by several instances of the class `NoseConeCurve`. An example of an instance of this class is given in Figure 3.1a. As mentioned before, the curve is a B-spline, which moves past several control points and is attached to fixed start and endpoints. The start and endpoints of the curves are attached to the wing. The x - and z -coordinates of these points, $(x_{\text{anchor}_u}, z_{\text{anchor}_u})$ and $(x_{\text{anchor}_l}, z_{\text{anchor}_l})$ are therefore fixed for constant y -position. The other x - and z -coordinates of the control points are the parameters that are altered during the optimization. In Figure 3.1a, three pairs of free coordinates are shown. However, the model can easily be extended by adding more points as inputs.

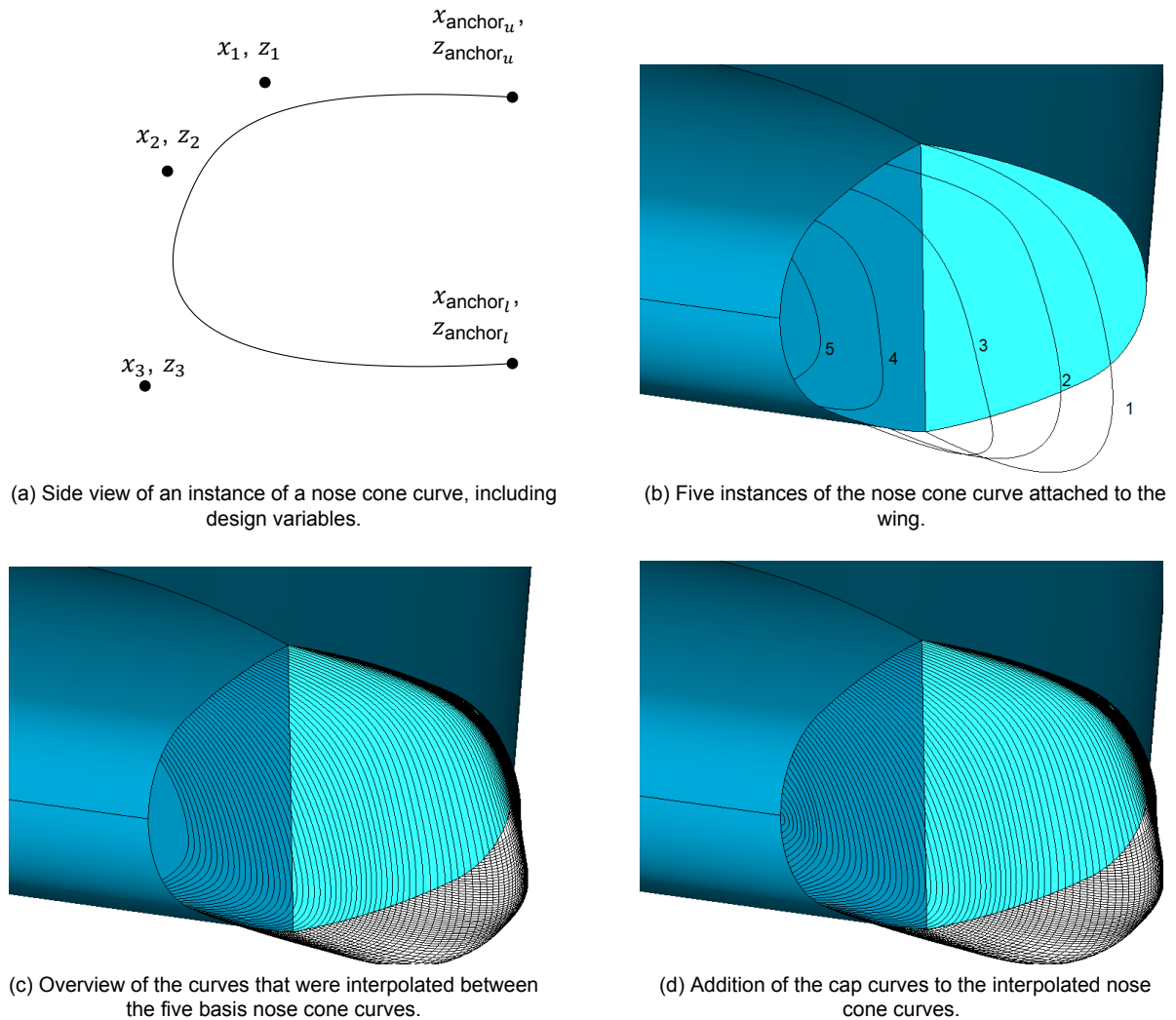


Figure 3.1: Overview of the parameterization steps performed to generate the nose cone geometry.

Figure 3.1b displays an example of the attachment of cockpit curves to the FV, in which five instances of `CockpitCurve` class are fixed to the wing. The points of the starboard curves are mirrored through the $x - z$ plane. A spanwise B-spline interpolation is done to create a large number of nose cone curves through the points of the curves and the mirrored curves. Again, for the interpolation B-splines are chosen, rather than a polynomial rail as was done in van der Pluijm [30], to omit the possibility of erratic behavior. A depiction of the cockpit curves created has been given in Figure 3.1c.

The control points are linearly interpolated from the most outboard curve towards the point where

the attachment edge crosses the wing leading edge. These interpolated points are used to create additional cockpit curves that close off the attachment edge with the wing, as shown in Figure 3.1d. With this collection of cockpit curves, an instance of the native `LoftedShell` class is used to represent the cockpit geometry.

3.1.2. Fairing

As the fairing should fit all three family members, the fairing space should be based on the most conservative in space, namely the FV-800. From the FV-800 floor plan in Appendix B in Oosterom [19], an allowed fairing semi-span of 1.48 m is measured between the engine pylons. Looking at section 3.1.1 in van der Pluijm [30], the fairing shape was built with the cross-sections that govern the outer geometry inclined at an angle. In the present study, the sections are aligned parallel to the freestream flow direction. This reduces any unnecessary flow disturbances by introducing edges to the geometry perpendicular to the flow.

Like the cockpit parameterization, the fairing geometry is built from several B-spline curves. The class `FairingCurve` is depicted in Figure 3.2a. This class combines two B-splines: one for the upper surface and one for the lower surface. Both of the B-splines have an anchor point on the wing. The two curves share the other anchor point. This point marks the trailing edge of the fairing. As both B-splines have (x_{TE}, z_{TE}) as an anchor point, the curves create a sharp trailing edge, which is the motivation for using two splines to create the fairing curve.

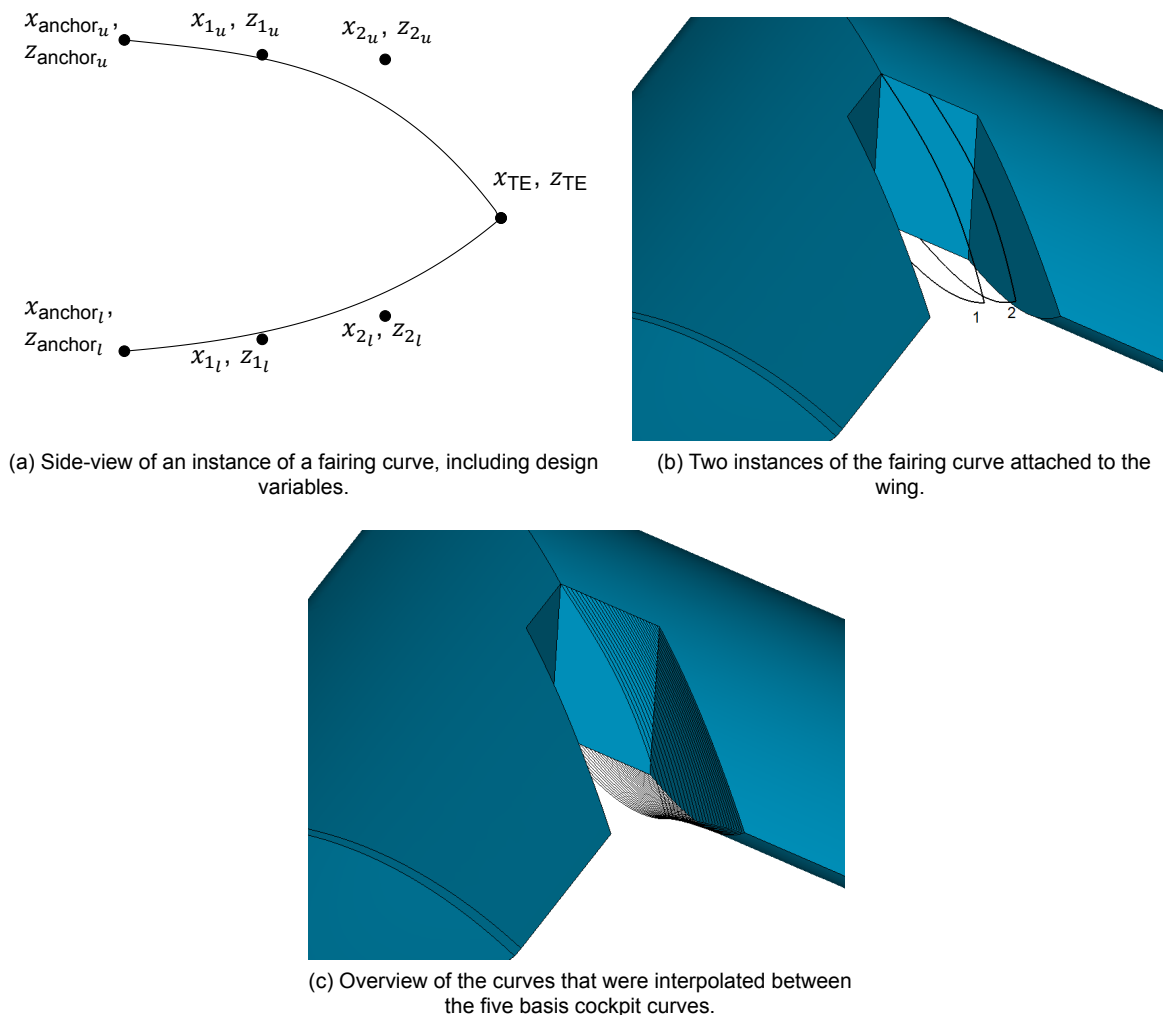


Figure 3.2: Overview of the parameterization steps performed to generate the fairing geometry.

In Figure 3.2b, the attachment of the fairing curves to the wing is shown. A B-spline interpolation

between these fairing curves is performed in the same manner as is done for the cockpit curves. The resulting interpolated fairing curves are depicted in Figure 3.2c. As the two surfaces' fixed connection is essential for successfully generating the resulting aircraft geometry, the curves are not reflected through the $x - z$ plane. Building a lofted shell through the total collection of curves would cause a bad connection to the wing in the fairing center. Therefore, a shell is built through the starboard curves. This shape is then mirrored through the $x - z$ plane, and both halves are fused.

3.2. Design Workflow

The nose cone and the fairing are designed using existing numerical optimization strategies. In order to limit the number of simultaneously altered design parameters, the optimizations are decoupled, which decreases the number of function evaluations needed to converge in a single optimization significantly and enables the simultaneous optimization of both objects. Therefore, the influence that one of the optimizations has on the other is assumed to be negligible.

The design workflow for the nose cone geometry is displayed in Figure 3.3. Due to the extensive nature of the process, a disquisition of the visible workflow is given here. To begin with, it can be seen that the process starts at the optimization hub, which is a PC on which an instance of the optimization algorithm runs. On this PC, several web-hosted aircraft objects are generated as well. These objects are initiated using the *Flask-RESTful API* [46] which is incorporated in the ParaPy library. The web-hosted aircraft objects allow for maintaining multiple aircraft objects simultaneously, without the computational cost of generating a new aircraft for each function evaluation. The optimizer then applies a new design vector to each aircraft object.

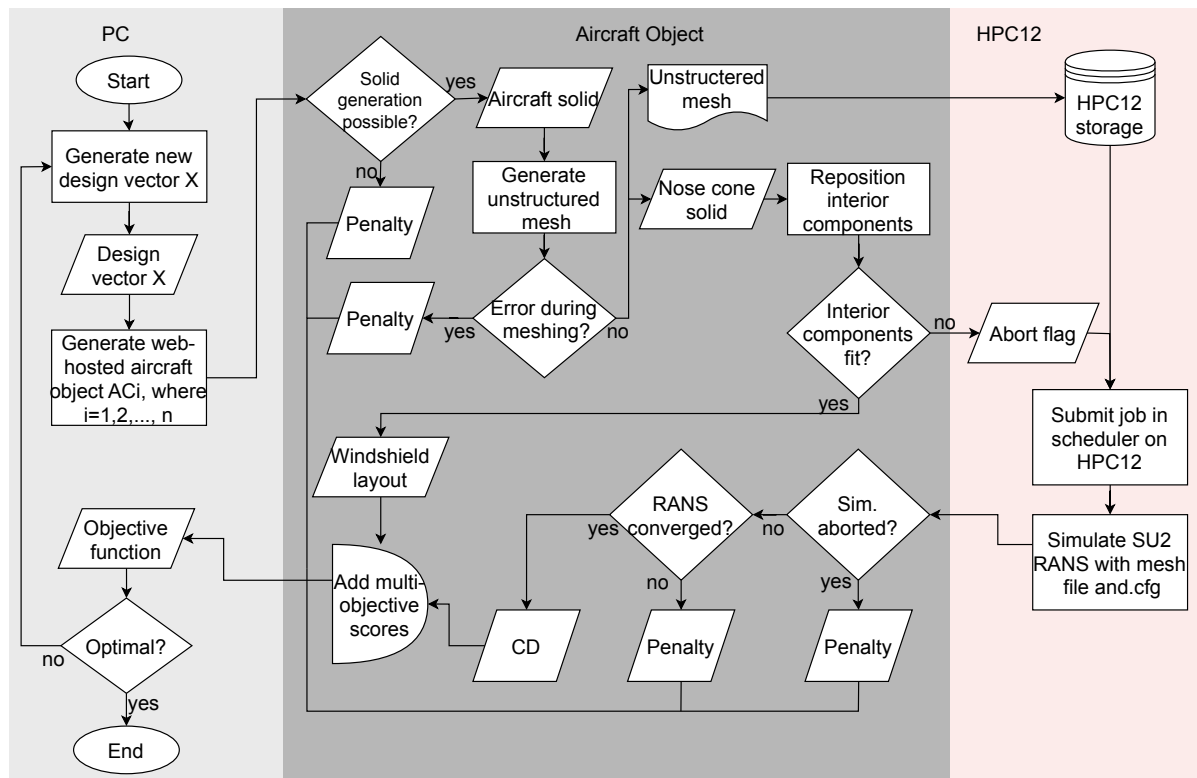


Figure 3.3: Workflow diagram of the nose cone optimization.

With the new design vector, the aircraft solid with a new nose cone is generated on each of the web-services. If an error occurs while generating the geometry, the process is halted, and a penalty is returned as the objective function, subsequently terminating the process. The penalty method used in this study is elaborated on in subsection 3.4.3. If the solid is generated successfully, it is passed to the automated meshing module. Similarly, if meshing is unsuccessful, a penalty is fed to the objective function, and the process ends. If the mesh is adequately generated, the unstructured mesh is sent to the High-Performance Computing (HPC) cluster at TU Delft, particularly HPC12. The use of HPC12

was included in the study in order to facilitate using the computationally costly RANS method in shape optimization. With each process allowing for parallel calculation over twenty cores, which account for 128 GB RAM on an Intel Xeon processor, the computing power is increased markedly compared to a typical home setup, as was used by Faggiano et al. [3] to perform a shape optimization using the Euler equations.

Meanwhile, the positions of radar, the NLG and the pilots are adjusted on each of the web-hosted aircraft objects. These repositioning steps are iterative processes and can take longer than evaluating the aerodynamic forces for some design vectors. Hence, both processes are performed in parallel. The optimization steps of these repositioning modules are discussed in section 3.3. To explain the workflow, it is important to note that when each component cannot be positioned in the nose cone at an adequate position, a message is sent to HPC12 to abort the current process. A penalty is sent to the optimization hub on the web-hosted aircraft, and the function evaluation is terminated.

The unstructured mesh is stored on HPC12, and a job to calculate the aerodynamic forces over the grid geometry is submitted to the job scheduler. Meanwhile, a download request is sent to HPC12 from the aircraft object at a constant interval. If the job is done and has converged well, the solution is downloaded to the optimization hub, where the drag coefficient is processed and sent to the objective function. However, a penalty is passed to the objective function if the solver could not converge to a solution within two hours. Furthermore, suppose during the flow simulation on the cluster a constraint violation is found in the aircraft object. In that case, a message is sent to the job scheduler on HPC12, telling it to abort the current simulation, avoiding unnecessary calculation time. Subsequently, in the aircraft object, a penalty is generated.

If no anomalies occur, figures of merit pertaining to the windshield dimensions are added together with the drag coefficient of the design at hand. This objective function is then fed back to the optimization algorithm.

The workflow of a single function evaluation of the fairing is portrayed in Figure 3.4. This process is more straightforward and does not contain the parallel evaluation of the constraints and the aerodynamics. This is enabled as evaluating the fairing constraints does not involve any iterative computations and can therefore be performed before calculating the forces on HPC12. After evaluating the constraints, a penalty is passed to the objective function if one or more constraints are violated. If all constraints are satisfied, an unstructured mesh is generated, checked, and submitted to the job scheduler, the same way as is done for the nose cone optimization. As the constraints have already been analyzed, the simulation is not aborted while running in the case of the fairing optimization.

3.3. Component Repositioning

As mentioned in section 3.2, the repositioning of the radar, the NLG, and the pilots has to be done at each function evaluation. The fitting of the components is done step-wise, as the pilot position depends on the location of the radar and the NLG. Each of the steps are represented by an evaluation of SciPy's `fmin` module [47], which employs the Nelder-Mead simplex algorithm [48]. This algorithm is suitable to finding a solution using a limited amount of function evaluations while having low memory requirements. The exact mathematical formulation of the objective functions of each of the repositioning modules is not essential to this report. However, a general formulation of the repositioning goals is given.

Figure 3.5 shows that the first component to be repositioned is the radar. The radar is fitted in the aircraft to install it as upstream as possible. This ensures that the radar is positioned in the nose of the aircraft. This enables the pilots to be close to the windshield while their feet stay behind the radar. The optimization is successful when the radar is as upstream as possible while still wholly included within the nose cone. A typical repositioned radar dish can be seen in Figure 3.6a.

For the NLG, the repositioning goal is to move the wheel as low in the cockpit as possible. Figure 3.6b shows a desirable position. As the cockpit floor is not allowed to coincide with the NLG, dragging the nose wheel down enables the pilot to be seated lower, allowing the optimizer to converge to geometry without a large headroom protruding on top of the cockpit.

Lastly, the pilot repositioning needs to be done to verify that the cockpit complies with the constraints inferred. An example of this change in positioning can be viewed in Figure 3.6c. In order to keep the windshield small, the pilots are positioned to achieve a correct viewing angle and distance from the windshield and the front pressure bulkhead, and a minimum overnose viewing pane area, and height. This forces the optimizer to converge towards a design with a windshield that allows for a large enough

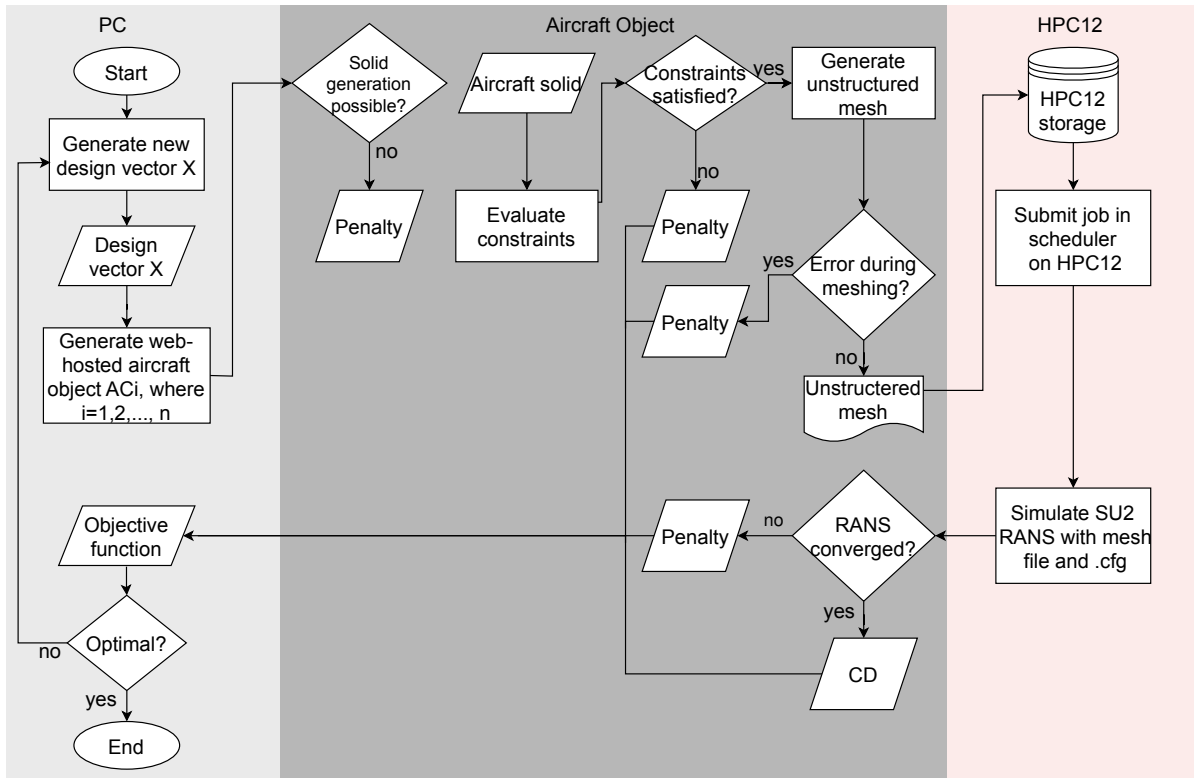


Figure 3.4: Workflow diagram of one function evaluation in the fairing optimization.

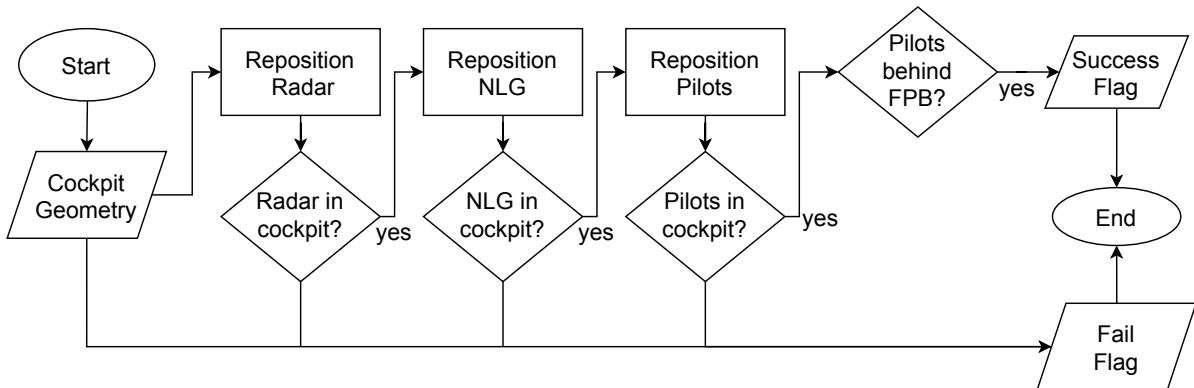


Figure 3.5: Workflow diagram of the repositioning of the radar, NLG and pilots.

visual segment at CAT IIIA approaches, as was discussed in section 2.2, without limiting the design space for the dashboard.

3.4. Optimization Definition

As was stated before, the optimizations of the fairing and the nose cone have been decoupled in this study. In short, the main goal of the optimizations is to minimize the absolute magnitude of the drag coefficient of the aircraft, C_D . The actual objective functions are, however, different. Furthermore, the (in)equality constraints assessed for each design have a different nature. The formal statement of the optimization goals and requirements are given in this section.

3.4.1. Nose Cone Optimization Problem Statement

The optimization of the nose cone is a multi-objective problem. Not only the drag coefficient is of importance for the final design of the cockpit, but also the windshield dimensions, which were introduced

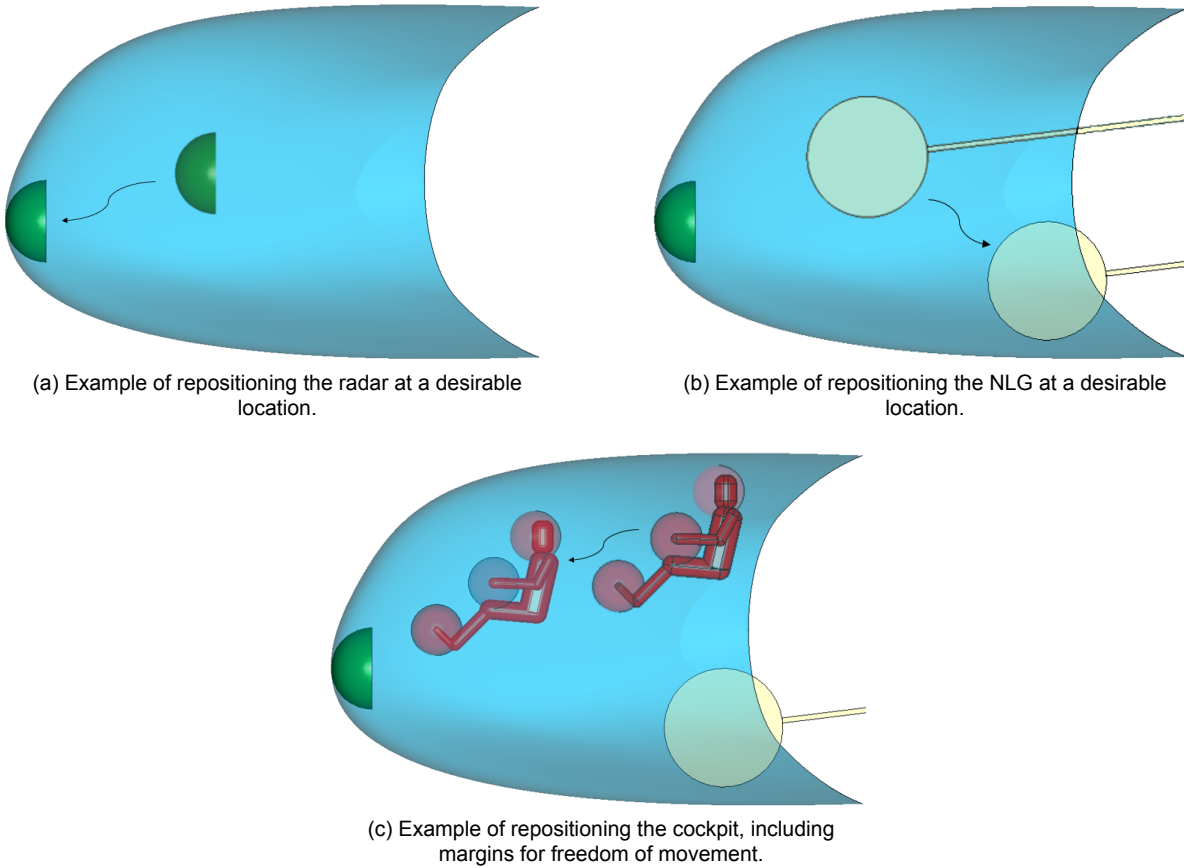


Figure 3.6: Visualization of the repositioning of the radar, NLG and pilot including margins.

in section 1.1. The formal definition of the objective function for the nose cone optimization is given in Equation 3.1. Here, the circumflex over the parameters denotes the normalization with respect to the values that correspond to the initial guess of the optimization.

$$\begin{aligned}
 \min_{\bar{X} \in \mathbb{R}} \quad & f(\bar{X}) = \frac{\sigma_{\hat{A}_{WS}}}{\sigma_{\hat{C}_D}} \hat{C}_D + \frac{\sigma_{\hat{A}_{WS}}}{\sigma_{\hat{h}_{ON}}} \hat{h}_{ON} + \hat{A}_{WS} \\
 \text{s.t.} \quad & g_i(\bar{X}) \leq 0 \quad \text{for } i = 1, \dots, n \\
 & h_j(\bar{X}) = 0 \quad \text{for } j = 1, \dots, n
 \end{aligned} \tag{3.1}$$

The three terms in the objective function have been given a proportion based on their standard deviations, σ , which are taken from an optimization test run. Using Equation 3.1, all three normalized quantities should be approximately equally important in the optimization, regardless of the magnitude of the differences.

Looking at the constraints, the equality and inequality constraints that are imposed on the nose cone optimization are primarily adopted from work done by van der Pluijm [30]. However, they are repeated explicitly in this report because of their significance for this study. Furthermore, some of the constraints are refined throughout this study. Hence, additional elaboration on these constraints is also presented in this section.

3.4.1.1. Outside View

For the overnose angle, this report deviates from van der Pluijm [30]. The overnose angle calculated there is equal to 31.5° . It is determined in the aircraft requirements that the FV should be able to land up to CAT IIIA approaches. Using the method described in section 2.2, the required overnose angle is found to be equal to 26° .

For the lateral angle of the overnose windshield pane, van der Pluijm [30] recommended an angle of

$\pm 10^\circ$. However, in this study, the recommendation of CS25.177(c) [32] is used. According to EASA, the sideslip angle β that can be expected during nominal operations can be calculated using Equation 3.2.

$$\beta = \arcsin(15.56/v) \quad (3.2)$$

In this equation, v is the calibrated airspeed. Using this relation, the recommended sideslip angle is equal to 12.7° . These constraints are used to calculate the windshield geometry of each design vector. Based on the windshield geometry, figures of merit are given to the cost function. This means that these pilot view constraints are not included in the penalty method, and a design vector is never rejected based on the view angles, as a windshield can always be generated.

3.4.1.2. Pilot Constraints

When looking at the pilots, the first constraint that comes to mind is their inclusion within the nose cone geometry after repositioning. The following equations [30] are the formal equality constraints that correspond to this notion:

$$h_{\text{pilot}}(\bar{X}) = \frac{(V_{\text{common}})_{\text{pilot,nose cone}}}{V_{\text{pilot}}} - 1 \quad (3.3)$$

$$h_{\text{margins}}(\bar{X}) = \frac{(V_{\text{common}})_{\text{margins,nose cone}}}{V_{\text{margins}}} - 1 \quad (3.4)$$

In Equation 3.3 V_{pilot} is the volume of the pilot model, which was built by van der Pluijm [30] in compliance with CS-25 standards, and $(V_{\text{common}})_{\text{pilot,nose cone}}$ indicates the common volume between the pilots and the nose cone solid. Similar definitions correspond to Equation 3.4, where ‘margins’ indicate spheres with a radius of 25 cm that were added around the pilot’s head, hands, and toes. This value has been based on the addition of room for the pilot to use aircraft controls and to be able to move his/her head. Another 10 cm has been added to this margin in order to account for the so-called insulation thickness as was prescribed by Roskam [49]. These margins can be seen in Figure 3.6c.

In practice, Equation 3.3 states that the geometry satisfies the constraint when the common volume between the cockpit and pilot solids is equal to the volume of the pilot solid. In other words, the design is accepted when the pilot solid is fully included inside the cockpit solid.

Additional constraints on the pilot position are conceived of the distortion effect that a slanted glass windshield has on the pilots’ visual of the outside. Torenbeek [50] set up a series of recommendations in order to maintain a clear visual of the surroundings. To summarize, it postulates that the DEP should be between 0.5 m and 0.6 m from the point where a horizontal from the DEP crosses the windshield. This distance is indicated by the viewpoint distance, l_{VP} . Moreover, at this same viewpoint, the angle between the horizontal and the tangent to the windshield, ϕ_{VP} , should be larger than 35° . As these are recommendations, they should not be seen as hard requirements. Furthermore, as the windshield area is included in the objective function, the hypothesis is formulated that the optimizer tends towards a cockpit in which the pilots are positioned further forward. In order to allow for this, the constraints regarding the distance of the DEP to the windshield are alleviated. The constraints relating the DEP to the windshield are formulated in Equations (3.5) to (3.7) [30].

$$g_{l_{\text{DEP,VP}_l}}(\bar{X}) \leq 1 - \frac{l_{\text{VP}}}{0.4} \quad (3.5)$$

$$g_{l_{\text{DEP,VP}_u}}(\bar{X}) \leq \frac{l_{\text{VP}}}{0.7} - 1 \quad (3.6)$$

$$g_{\phi_{\text{VP}}}(\bar{X}) \leq 1 - \frac{\phi_{\text{VP}}}{30^\circ} \quad (3.7)$$

3.4.1.3. Radar Constraints

Van der Pluijm [30] specified that the reference weather radar to be used for the cockpit optimization is the Honeywell flat plate antenna. Weather antennae are typically positioned in the aircraft nose, in the radome. The radome is separated from the pressurized part of the aircraft with the front pressure bulkhead (FPB), which is also where the radar is mounted and can be distinguished in Figure 1.3. Like

the pilot constraints, the first radar constraint specifies that the entire radar volume should be included within the nose cone solid. Mathematically this is represented by Equation 3.8 [30].

$$h_{\text{radar}}(\bar{X}) = \frac{(V_{\text{common}})_{\text{radar,cockpit}}}{V_{\text{radar}}} - 1 \quad (3.8)$$

To be able to construct the structure to which the weather radar is attached, it is assumed that the radar should be in front of the pilot's feet. Using an additional 15 cm for installation space, structural reinforcement, and the socket in which the antenna is allowed to rotate, the inequality constraint that corresponds to the position of the radar concerning the pilot position is given by Equation 3.9 [30].

$$g_{\text{radar,pos}}(\bar{X}) \leq \frac{x_{\text{radar}}}{x_{\text{pilot}} - x_{\text{margin,radar}}} - 1 \quad (3.9)$$

3.4.1.4. NLG Constraints

Again, an equality constraint is dedicated to ensuring the inclusion of the component within the cockpit volume after moving to the optimal position. The formal statement for this is given in Equation 3.10 [30].

$$h_{\text{NLG}}(\bar{x}) = \frac{(V_{\text{common}})_{\text{NLG,nose cone}}}{V_{\text{NLG}}} - 1 \quad (3.10)$$

Furthermore, as presented in subsection 3.2.3 of van der Pluijm [30], the cockpit floor position is a function of the height at which the pilot is seated. Therefore, to ensure that the NLG is positioned under the cockpit floor, the inequality constraint in Equation 3.11 is employed to enforce this.

$$g_{\text{below floor}}(\bar{x}) \leq z_{\text{NLGtop}} - z_{\text{floor}} \quad (3.11)$$

3.4.2. Fairing Optimization Problem Statement

The fairing optimization has a less complex nature than the cockpit optimization. The objective function does not have multiple objectives for this part of the study. It is given by Equation 3.12. It can be seen that the single goal of this minimization is to reduce the drag coefficient of the FV aircraft. Enlarging the center-body fairing would be a virtue, as the aircraft volume dedicated to fuel storage would increase. However, this is not added as a main goal of this study.

$$\begin{aligned} \min_{\bar{X} \in \mathbb{R}} \quad & f(\bar{X}) = \hat{C}_D \\ \text{s.t.} \quad & h_i(\bar{X}) = 0 \quad \text{for } i = 1, \dots, n \end{aligned} \quad (3.12)$$

The constraints that are to be imposed on the fairing geometry originate from the galley. Figure 3.7¹ gives an overview of which part of the galley intersects with the fairing geometry. Visible are the outlines of the FV aircraft in black and the outlines of the trapezoidal inner cabin in light blue. The point where the trailing edges of the cabin come together is used as the center point of the arcs that demarcate the galley.

Arc 1 denotes the part of the galley up until which the flight crew should be able to move around freely. In Figure 3.7, this area is colored red. The assumption is made that this would account for 2.25 m measured from the floor. With approximately 15 cm structural thickness, 2.1 m is left for emergency escape signs and walk passage. Arc 2 has a radius that is 1.2 m larger than the upstream arc. This arc marks off the area in which the outer mold line of the fairing should be at least 15 cm lower than the floor height to allow for structural reinforcement. The area that is affected by this requirement is colored blue in Figure 3.7. Here, the galley carts and cabinets are stored. Therefore, headspace is not important here, and the constraint for passage height is alleviated.

The same arcs are used to cut the upper and lower fairing skin. To assess whether the fairing is high and low enough for the galley, two instances of `HalfSpaceSolid` are generated. A `HalfSpaceSolid` is a native ParaPy class that demarcates all geometry protruding from an infinite plane. In the definition of the galley constraints, the planes are parallel to the xy -plane. All geometry that is above $z = 2.25$ m is within the upper `HalfSpaceSolid` and all geometry that is below $z = -0.15$ m is within the lower

¹Personal correspondence with Dr. R. Vos on 23-06-2021.

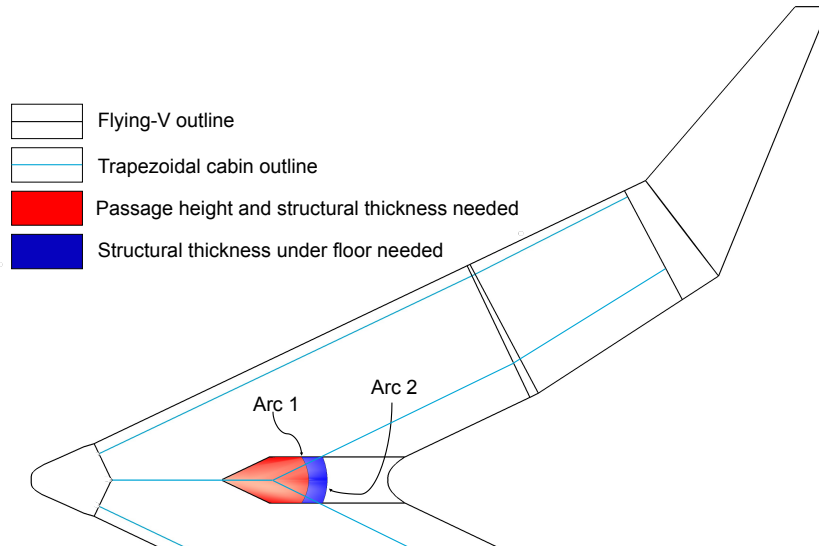


Figure 3.7: Floor plan of the FV with trapezoidal cabin. The colored regions denote parts of the galley that are affected by the constraints.

HalfSpaceSolid. The fairing stands tall enough if the upper galley surface is wholly included within the upper HalfSpaceSolid. Formally, this is represented by the equality constraint in Equation 3.13.

$$h_{\text{galley}_u} = \frac{(A_{\text{common}})_{\text{galley,HSS}_u}}{A_{\text{galley}_u}} - 1 \quad (3.13)$$

Similarly, the fairing is low enough to fit the floor in the galley, and additional space for structural reinforcement when the lower galley surface is entirely within the lower HalfSpaceSolid. This constraint is formulated in Equation 3.14.

$$h_{\text{galley}_l} = \frac{(A_{\text{common}})_{\text{galley,HSS}_l}}{A_{\text{galley}_l}} - 1 \quad (3.14)$$

3.4.3. Optimization Algorithm

For both of the optimizations, the pre-built Differential Evolution (DE) algorithm from the `scipy.optimize` API [47] is used. DE as an algorithm was developed by Storn and Price [51]. Similar to evolutionary algorithms (EAs), DE generates a first population using Latin Hypercube Sampling (LHS) [52] over the selected design space. LHS ensures that the selected design vectors are distributed evenly over the design space. Among the population, mutated design vectors are generated using features of multiple children. The parents with the highest ‘fitness’ propagate to the next generation of children, to which the same process is applied.

DE has been chosen for this numerical optimization for several reasons. To begin with, the objective function is costly. Exploring the possibility of performing RANS calculations in an optimization study, one function evaluation can take up to two hours. To increase the number of function evaluations possible per unit of time, the parallelized DE algorithm is employed, which is readily available in `scipy.optimize` [47]. Furthermore, the algorithm is robust in highly non-linear objective functions [53], which is assumed to be the case in the problem at hand. The independence of gradient evaluations because of the metaheuristic nature of the algorithm causes the optimizer to shift away from parts of the design space where constraints are violated or meshes cannot be generated.

For both the nose cone and the fairing optimizations, the population size is set to four times the number of design variables. Both optimizers run six parallel processes, and a maximum of thirty iterations is allowed.

The constraints in this optimization problem are represented by penalty functions, as was described in section 3.2. If the constraint evaluation method from `scipy.optimize` is used, the constraints and the function value are evaluated simultaneously. This is a feasible option for cheap objective functions.

In this case, however, where the objective function is costly, there is unprecedented efficiency in being able to skip the objective function evaluation immediately when constraints are violated or an error during geometry or grid generation occurs. For this purpose, penalty functions are used. De Melo and Carosio [54] established the concept of using penalty functions. They proposed to add a large penalty to the objective function to force the optimizer away from the infeasible regions of the design space. De Melo and Carosio put this strategy to the test combined with DE, which yielded promising results. This study's objective function is not evaluated with violated constraints; only the penalty function is passed. According to Michalewicz and Schoenauer [55], this is called the 'Death Penalty Method' and can yield quality results in combination with EAs. The mathematical definition of this notion is given in Equation 3.15, where $p(\bar{X})$ is the penalty given based on the design. In this study it is generally a value that is two orders of magnitude larger than the expected function value for an adequate design, in order to force the optimizer away from this part of the design space.

$$f(\bar{X}) = \begin{cases} f(\bar{X}), & \text{if feasible} \\ p(\bar{X}), & \text{if infeasible} \end{cases} \quad (3.15)$$

3.5. Aerodynamic Analysis

In this section, a disquisition of the aerodynamic analysis is given. The aerodynamic analysis presented is the same for both shapes and the selected settings are used in the numerical optimization.

3.5.1. Aerodynamics Solver

For each evaluation of the objective function during the numerical optimization, the aerodynamic forces of the current design are assessed by simulating the forces over the aircraft in the open-source Computational Fluid Dynamics (CFD) solver in the SU2 suite. SU2 is a proven solver built for CFD, which has grown to be a multidisciplinary platform for solving a variety of Partial Differential Equations (PDEs). The validation of the aerodynamics module of this solver is presented in section 4.4.

The compressible RANS equations are used to model the flow over the aircraft. Compared to other studies regarding the FV, where Euler was used to evaluate the aerodynamic forces, the RANS equations were chosen in this study for the capability of capturing viscous forces by simulating the boundary layer, which omits the need for an empirical viscous module as was done by Faggiano et al. [3]. In a high-Mach-number problem like the study at hand, the displacement thickness of the boundary layer can become significantly large, affecting the effective curvature, and subsequently the pressure distribution [33]. Furthermore, from the artistic mockup and the previous work done by van der Pluijm [30] on the cockpit, it can be seen that in order to comply with the constraints, the cockpit windowpanes could potentially become blunt and inclined in a close-to-perpendicular manner to the local flow direction. In addition, the fairing was added to the aircraft in order to alleviate the root effect. It has already been seen that a shock occurs at the center body of the current design. Therefore, it is deemed necessary to map the shock location and strength for optimization correctly.

To accelerate each function evaluation in the optimization, the Spalart-Allmaras (SA) turbulence model [56] has been used, which has been proven to perform well. This model needs a single additional PDE, which significantly reduces the computational overhead in comparison to widely used two-equation models, such as Menter's SST [57], which is also available in SU2. In order to promote robustness during the optimization process, the Jameson-Schmidt-Turkel (JST) convection scheme is used, as according to Faggiano et al. [3], it is more reliable and converges faster than Roe, at the cost of numerical accuracy.

3.5.2. Numerical Domain

The numerical domain over which the flow is solved in the aerodynamic analysis is set up using the dimensions as portrayed in Figure 3.8. A half-model of the FV is used to model the aircraft aerodynamics by imposing a symmetry boundary condition on the plane at the symmetry plane of the aircraft. The wing itself is modeled as an adiabatic no-slip wall. This is typical for solving viscous flows, as this boundary condition forces the advection velocity at the wall to be equal to zero, which is one of the characteristics of the velocity profile of the boundary layer. The far-field boundary condition that is incorporated in SU2 in order to mimic flight in freestream conditions has been used on all domain walls, excluding the symmetry plane. The dimensions of the numerical domain are established using

the method in van Arnhem et al. [58]. An example of the variations in Mach and pressure gradients have been plotted in Figure 3.9. It can be seen that the gradients already have negligible magnitudes at the annotated locations. These values have been used for the final domain size. The verification of the chosen domain size is presented in section 4.1.

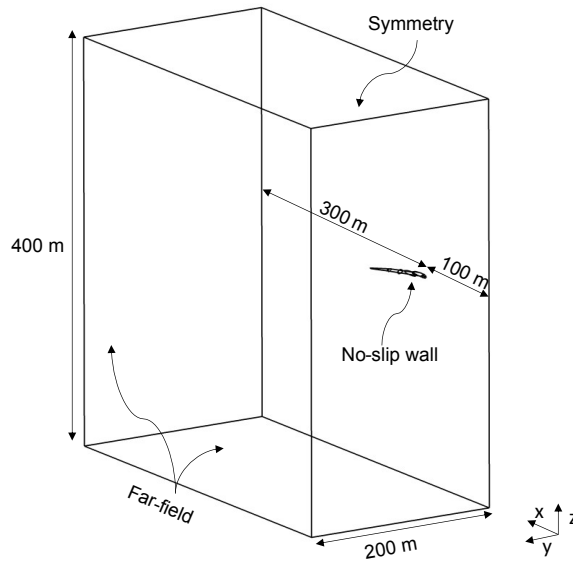


Figure 3.8: Visualization of the numerical domain, including dimensions and boundary conditions.

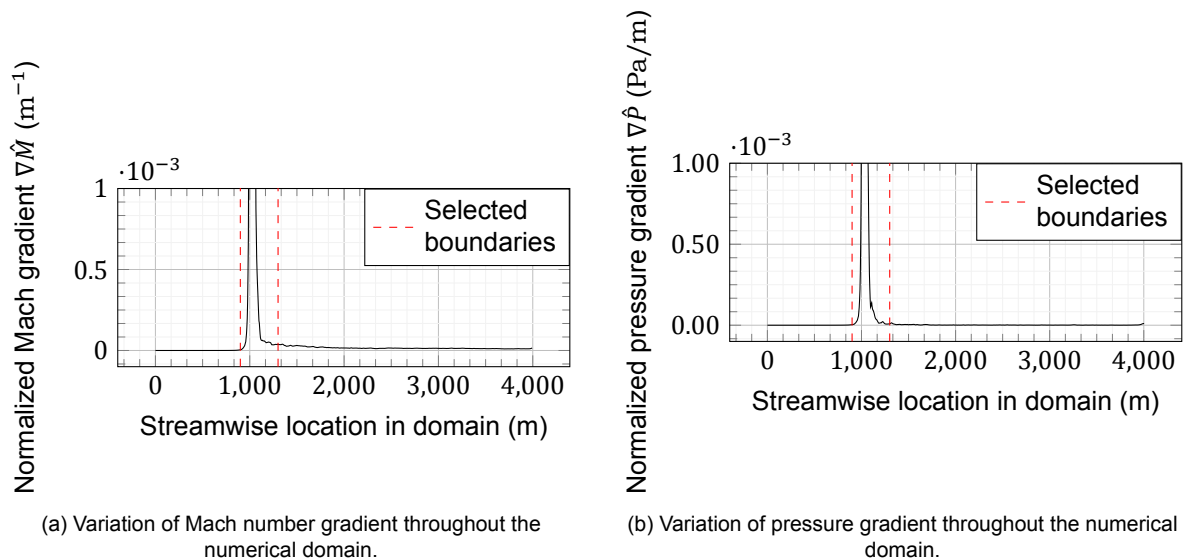


Figure 3.9: Example of required domain size study using the method of van Arnhem et al. [58].

3.5.3. Spatial Discretization

Using Salome Mesh, unstructured meshes are generated for every design. The aircraft surface has been overlaid with a triangular grid of which the triangles are allowed a maximum size of 0.14 m, which can be translated to '0.6% of the root chord length'. This grid size results in the densest mesh that could be reliably created over most of the design space. The domain walls are discretized with a surface mesh of which the triangles were allowed to grow up to 21 m, which is equal to 5% of the domain wall length. The volume of the domain is filled with a hybrid mesh. The hybrid grid comprises tetrahedron elements

and prism elements. In this hybrid grid, the tetrahedrons are permitted a maximum size of 21 m as well, in order to match the triangular mesh on the domain walls.

The prism elements are applied around the aircraft surface to capture the directional flow and the viscous effects in the boundary layer. First, in order to capture the viscous effects in the boundary layer, it is important to select a sufficiently thin first prism layer, starting from the aircraft surface. A commonly used metric to assess the boundary layer resolving is the non-dimensional first layer height, y^+ . In general, for numerical setups without wall functions, y^+ should be equal to, or less than one [59]. The SU2 RANS solver can output y^+ if desired. Using trial simulations, the dimensional thickness of the first layer was adjusted iteratively until the required value was achieved. This corresponded to a thickness of the first layer of $1.9\mu\text{m}$.

Moreover, to capture the flow throughout the entire boundary layer correctly, the structured prism layers need to enclose the boundary layer fully. As a first guess for the boundary layer thickness, the empirical relation for δ_{99} for a turbulent flat plate in Equation 3.16 [60] has been used.

$$\delta_{99} = 0.37 \frac{x}{\text{Re}_x^{1/5}} \quad (3.16)$$

δ_{99} is a measure for the boundary layer thickness and represents the position, measured from the aircraft surface, at which the velocity is equal to 99% of the local flow velocity. Furthermore, x is the streamwise position on the airfoil, and Re_x is the Reynolds number based on the local characteristic length. The equation shows that the thickest part of the boundary layer occurs at the trailing edge, which is in accordance with boundary layer theory. Based on this, it can be deduced that the largest δ_{99} is found at the trailing edge of the aircraft root. Inserting the correct values, the initial guess for the inflation layer thickness is equal to 0.17 m. This value is used over the entire wing surface.

With the initial guess in place, the inflation layer thickness was iterated using trial and error by increasing the total prism layer thickness for a small growth ratio of 1.15. The boundary layer was visualized during this process using the eddy viscosity ratio. This ratio is a measure of the turbulent nature of the flow. Generally, the eddy viscosity ratio is an order of magnitude greater within the boundary layer. Using this notion, the boundary layer is found to be fully resolved at a boundary layer thickness of roughly 25 cm. The prominence of the eddy viscosity ratio in the boundary layer has been visualized in the detail of the root trailing edge of the FV in Figure 3.10. It can be seen that the prism layers enclose the boundary layer until the point where the boundary layer merges with the aft wake and is not visible anymore.

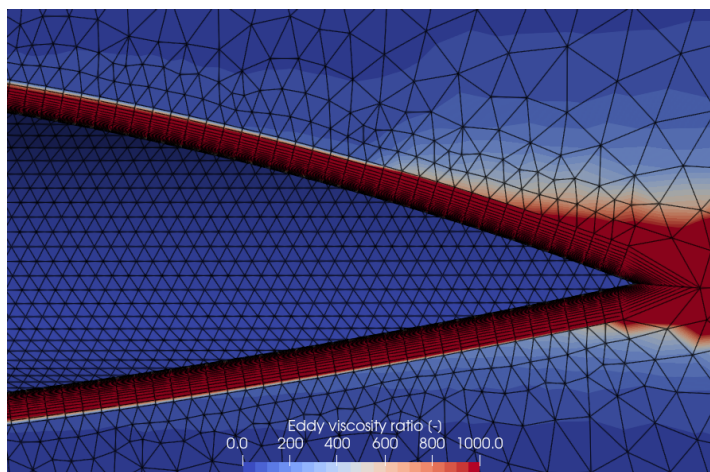


Figure 3.10: Visualization of the eddy viscosity ratio at the trailing edge of the wing root.

The inflation layer is constructed using the thickness of the first prism layer and the total thickness of the layers to capture the boundary layer. In selecting an adequate growth factor, the smoothness of the interface between the prisms and the tetrahedrons is taken into account. Reducing the difference in size between the prisms and tetrahedrons increases the accuracy of the simulation. Moreover, it increases the reliability of the automatic mesh generator used in this study. To avoid deviating too far from the recommended value of 1.25 or lower, a growth factor of 1.3 was used, which results in 40

layers to achieve the intended inflation layer thickness. A detail of the interface between the prism elements and the tetrahedrons around the cockpit geometry has been displayed in Figure 3.11.

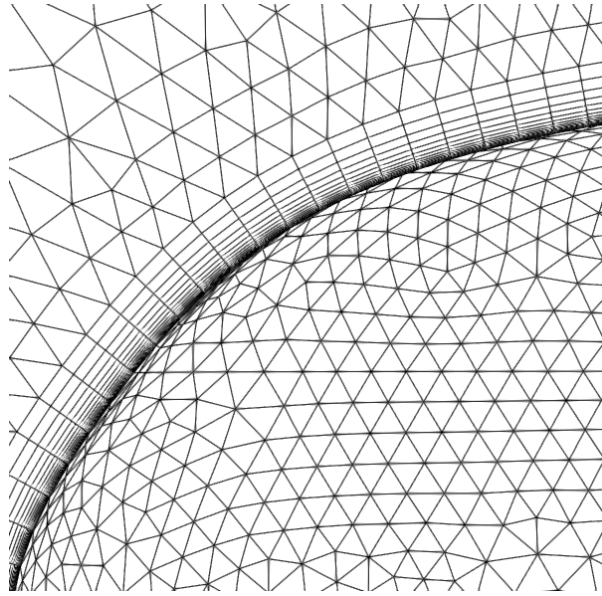


Figure 3.11: Detail of the inflation layer around the aircraft geometry and the interface between the prisms and the tetrahedrons.

4

Verification and Validation

This section presents the verification and validation results for the aerodynamic analysis performed in the optimization. A mesh suitable for RANS simulations without wall functions introduces the need for a very fine inflation layer, for which complex relations between the parameters exist. This chapter serves the purpose of showing that the forces are adequately resolved, starting with assessing whether the domain size does not influence the solution significantly in section 4.1, after which the convergence of the aerodynamic forces, with respect to varying grid density, is discussed in section 4.2. Next, the suitability of the chosen prism layer parameters is appraised in section 4.3. In order to verify that the aerodynamic method is sufficiently accurate, the section is concluded with an overview of the validation of the SU2 RANS solver section 4.4.

4.1. Domain Size

In order to verify whether the domain is selected sufficiently large, the forces are calculated using a numerical domain with dimensions that are ten times larger than the dimensions of the selected domain. This amounts to a parallelepiped with dimensions of $\{4000, 2000, 4000\}$ m and results in a volume mesh that is roughly a thousand times as large. In order to inspect the sensitivity to smaller domains than the selected one, another simulation using dimensions of $\{200, 100, 200\}$ m is performed.

With the desired dimensions in place, it has to be assessed whether the shrinking of the numerical domain has a significant or a negligible effect on the aerodynamic force coefficients. The errors of the force coefficients with respect to the large domain are tabulated in Table 4.1. It can be seen that the error does not exceed an absolute value of 1.0% for any of the force coefficients for the selected domain size. The influence on the forces is deemed negligible when considering the significant difference in domain size and the number of mesh volume elements. The selected domain is therefore considered acceptable. The errors introduced by the smaller domain are larger, the greatest being the error in pitching moment coefficient of 1.9%. It can be concluded that the loss in accuracy of the small domain hardly results in a smaller computational overhead, looking at the number of mesh cells. Therefore, the selected domain size from section 4.1 is deemed verified.

Table 4.1: Pitching moment and drag coefficient errors with respect to the force coefficients calculated on a numerical domain with dimensions equal to $\{4000, 2000, 4000\}$ m with 19.1×10^6 volume elements.

Domain dimensions (m)	ϵ_{C_m} (%)	ϵ_{C_D} (%)	$\epsilon_{C_{D_p}}$ (%)	$\epsilon_{C_{D_f}}$ (%)	Number of cells (-)
$\{200, 100, 200\}$	1.9	-0.68	-1.0	0.093	4.9×10^6
$\{400, 200, 400\}$	-0.033	-0.43	-0.78	0.33	4.9×10^6

4.2. Grid Density Convergence

In order to verify whether the forces are resolved sufficiently accurately, a mesh convergence study is conveyed. For a hybrid mesh like the one used in this study, the definition of the unstructured volume

and surfaces meshes are not only important. It is also essential to have a clear understanding of the performance of the inflation layer around the aircraft shape. After this section, in section 4.3, this is outlined. First, however, the effect of the triangle and tetrahedron sizes are evaluated. The results of this study are displayed in Figure 4.1.

To begin with, in Figure 4.1a it can be seen that the largest part of the variation in the drag coefficient is caused by the pressure drag component, C_{D_p} . The effect can explain this that the surface mesh density has an influence on the shape over which the solver finds a solution. A denser mesh results in a smoother surface that represents the actual shape more accurately. This changes the pressure drag component of the inviscid drag significantly. However, the wetted area does not change as much, and the inflation layer thickness and growth rate remain untouched during this evaluation. Therefore, it is not surprising that the relative error in C_{D_f} remains small for coarser meshes.

It can be seen that at triangle size of 0.1 m, C_{D_p} has converged well, going below 1.0% error from the finest grid size. Looking at the mesh size, however, it should be noted that the convergence mark corresponds to 9.8 million grid cells, which is deemed too expensive for this optimization study. The value used in this survey, being 0.14 m, has a larger error than the margins that Faggiano and Vos [3], Hillen [17], and Wilod Versprille [61] introduced. However, as mentioned in section 3.5, this mesh size resulted in a smaller amount of erratic grids for the cockpit geometry. This means that an error in inviscid drag equal to 11.9% is to be expected in the inviscid drag component throughout the optimization. An error of this magnitude is deemed acceptable in a study where the absolute value of the drag coefficient is not of importance. Instead, the optimizer should record the change with respect to the initial guess. Moreover, it is deemed tolerable to accept a greater error to enable fast calculations of the RANS equations to increase the feasibility of this study.

It can be seen that the forces converge quickly for maximum tetrahedron sizes of 21 m when looking at Figure 4.1b. The selection of this parameter value is therefore deemed a good choice.

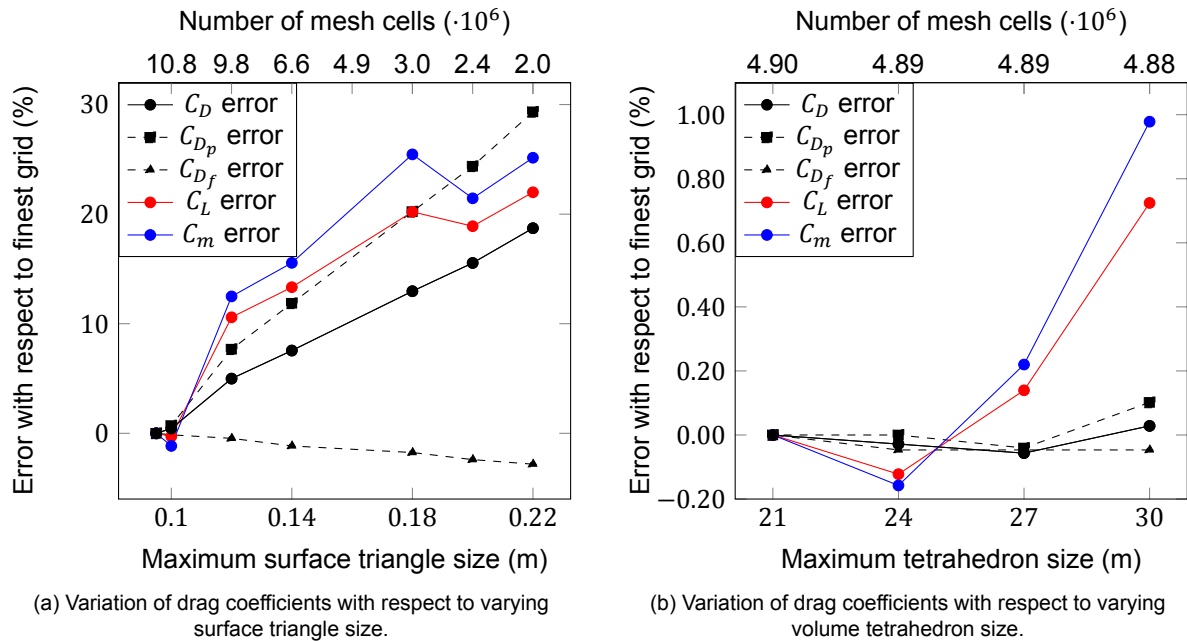


Figure 4.1: Variation of the aerodynamic force coefficients with respect to varying mesh triangle and tetrahedron sizes and number of mesh cells.

Furthermore, it should be verified that the position of the shockwave is predicted well with a lower mesh density. In order to assess this, the pressure distributions at the shocks of the solutions with a maximum triangle size of 0.14 m and 0.10 m are plotted in Figure 4.2. It can be seen that the shock position on the upper surface is predicted adequately for the coarser grid when looking at Figure 4.2a. Furthermore, it can be seen that on the downstream side of the airfoil, the effective curvature of both the upper- and lower surfaces is underestimated when simulated over the coarser mesh. The larger curvature for the grid with 0.10 m triangle size can be used to explain the underestimation of the lift of

the coarser mesh.

Moreover, looking at the pressure distribution at the outboard shock in Figure 4.2b, similar behavior can be noticed. In this plot, however, the position of the upper surface shock is estimated a small distance more downstream than with the mesh with a maximum triangle size of 0.10 m. The lower surface shock is predicted adequately. It can also be seen that the curvature is underestimated for this spanwise station, where this effect is already visible further upstream.

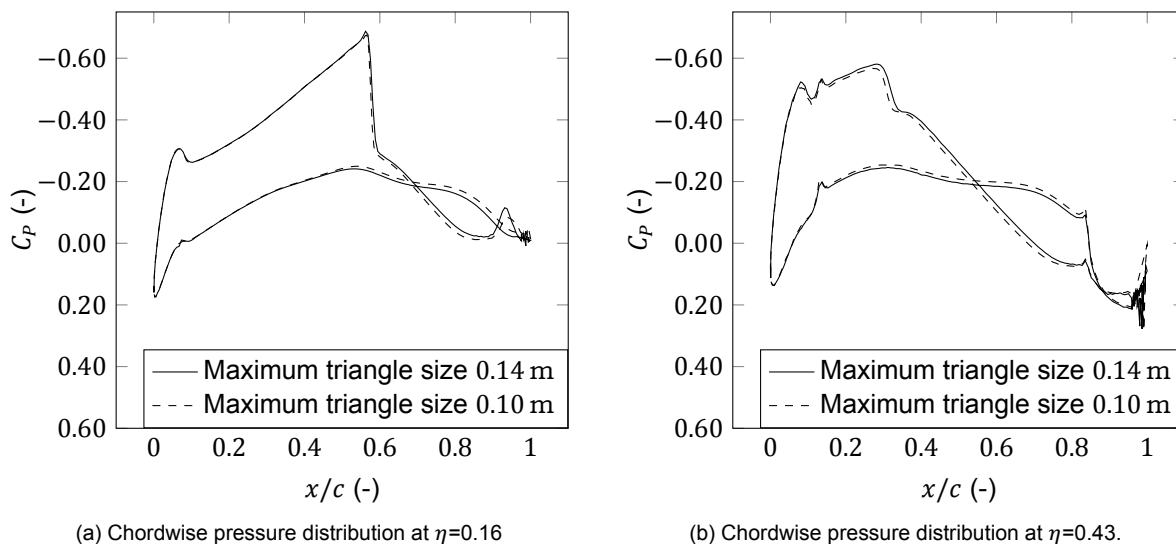


Figure 4.2: Comparison of pressure distributions between surface meshes with 0.14 m and 0.10 m maximum triangle sizes.

The more prominent role of the coarser mesh's decambering effect on the represented geometry of the outboard shock is explained by the difference in local chord length and thickness. The smoothing of the geometry by introducing a coarser mesh affects a smaller airfoil more. Therefore, the difference in pressure distributions increased.

4.3. Boundary Layer Solving

As is described in section 3.5, in order to capture the viscous effects, a y^+ below one is desirable for the mesh. The first prism layer is built, protruding from the surface mesh. Each surface triangle, therefore, has a corresponding prism element. The non-dimensional first layer heights are taken from the surface solution. An overview of the first layer height encountered throughout this survey is given in Figure 4.3. Its values are represented in a histogram in Figure 4.3a. From the figure, it can be seen that all values are below 1.0. Looking at the histogram, it becomes apparent that most of the cells in the first layer have a y^+ between 0 and 0.4. However, as a consequence of the inflation layer being constant over the entire surface of the aircraft, the thickness of the first cell of $1.9 \mu\text{m}$, causes the y^+ to increase to 0.83 at the trailing edge. The big variation in y^+ at the trailing edge is shown in Figure 4.3b. Moreover, increasing the first layer thickness by small amounts showed a y^+ higher than 1.0 in these areas for some designs. Therefore, it is decided not to increase the first layer thickness.

Another prism layer parameter that influences the accuracy of a simulation is the growth factor. Figure 4.4 shows the variation of the aerodynamic force coefficients with respect to the smallest growth factor recorded. It can be seen that when moving away from the recommended growth factors, the accuracy deteriorates. However, it can be seen that the magnitude of the error is not detrimental yet. As the number of volume elements almost scales with the number of prism layers, it is deemed acceptable to use a slightly higher growth factor at the cost of numerical accuracy.

4.4. RANS Solver Validation

A test case distributed by the developers of SU2 is used to validate the aerodynamic solver. The SU2 Euler solver has already been validated in Faggiano et al. [3], but in this report, the validation of the RANS solver is presented. The same experimental results from Test 2308 from Schmitt and Charpin

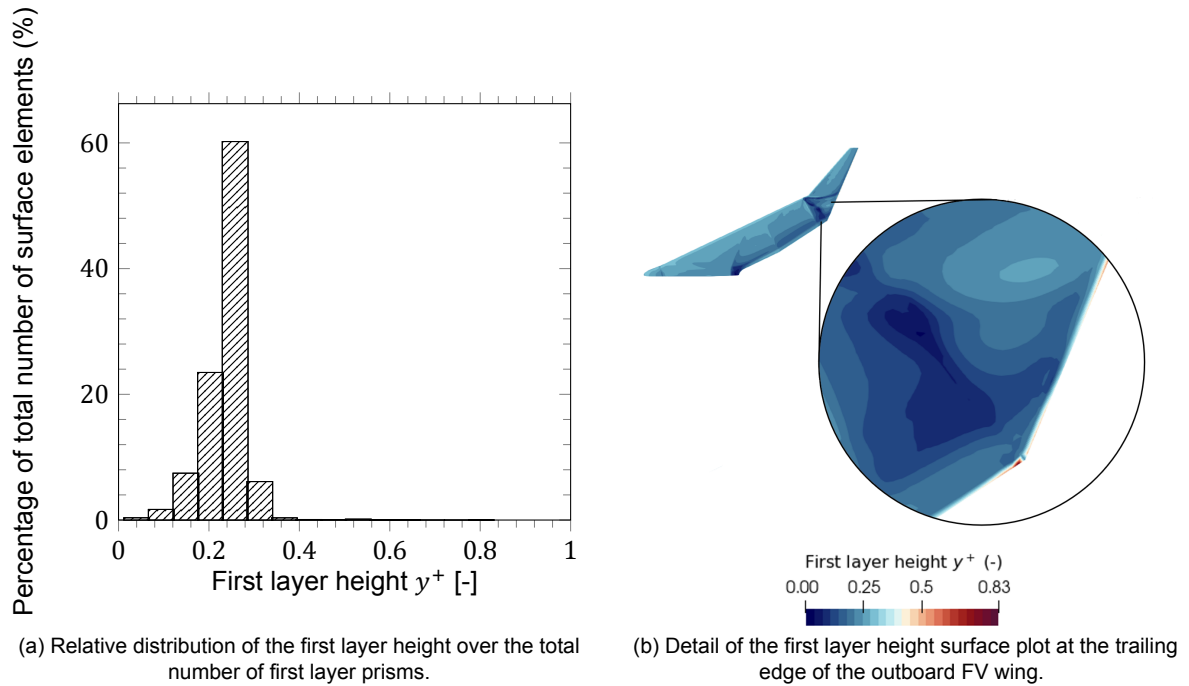


Figure 4.3: Overview of the distribution of the first layer height with histogram and detail of trailing edge at outboard wing.

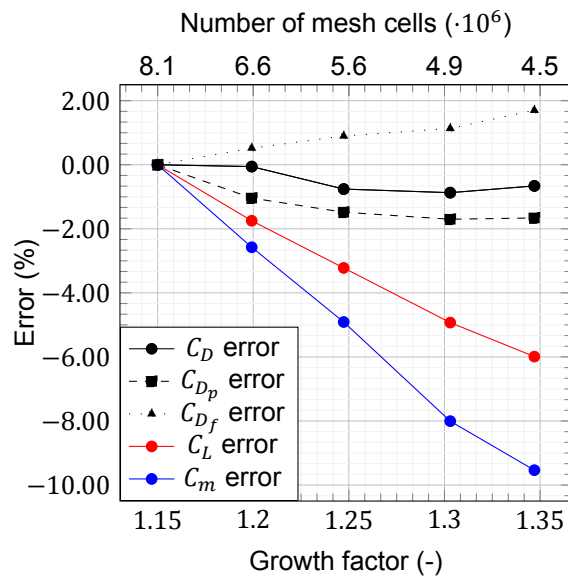


Figure 4.4: Error with respect to the smallest recorded growth factor. Throughout the evaluations, n_{layer} is allowed to vary and the total thickness of 25 cm is kept constant.

[62] are used to validate the solver. For spatial discretization, a grid with 315 thousand hexahedral elements that SU2 distributes is used. The flight condition at which the aerodynamic forces are recorded is at a transonic Mach number of 0.8395, an angle-of-attack of 3.06° , and a Reynolds number of 1.2×10^7 . Similar boundary conditions are used as in Figure 3.8. The wing is modeled as an adiabatic wall; far-field boundaries represent the walls that demarcate the numerical domain, and the wall in the symmetry plane of the wing is a symmetry boundary condition.

A comparison of the wind tunnel test data and the RANS simulation over the coarse mesh of seven of the simulated spanwise stations is presented in Figure 4.5. It can be seen that there is a discrepancy between the experimental data and the simulated pressure distributions. However, the general shapes

of the pressure distributions resemble the experimental data. Figure 4.5a displays a larger suction peak in the experimental data than in the simulation. This is the most inboard station and in the real wind-tunnel experiment, the ONERA M6 wing is clamped to a wall at this location [61, 63]. The higher suction peak can possibly be explained by the superposition of the supervelocities at the wing-wall junction.

In Figure 4.5c, it can be seen that the simulation does not capture the upper surface shock that occurred during the experiment. Also, the pressure recovery deduced from the data can not be distinguished in the simulated solution. It is assumed that this can be accounted to the coarse mesh that from SU2. At the trailing edge, the curvature is captured adequately, however. Another outlier is the pressure distribution in Figure 4.5g. This is the most outboard wing station, close to the wing tip. It can be seen that the solver does not capture the tip effects at the trailing edge of the wing section. It has been shown in literature that even with high fidelity meshes, these flow effects at the tip are inaccurately mapped for the ONERA M6 wing [61].

To conclude, the simulated pressure distributions resembles the experimental data as a whole to a satisfactory level. In spite of the accuracy not being high at all spanwise stations, the accuracy is deemed satisfactory, taking into account that the number of mesh cells for this RANS simulation is limited.

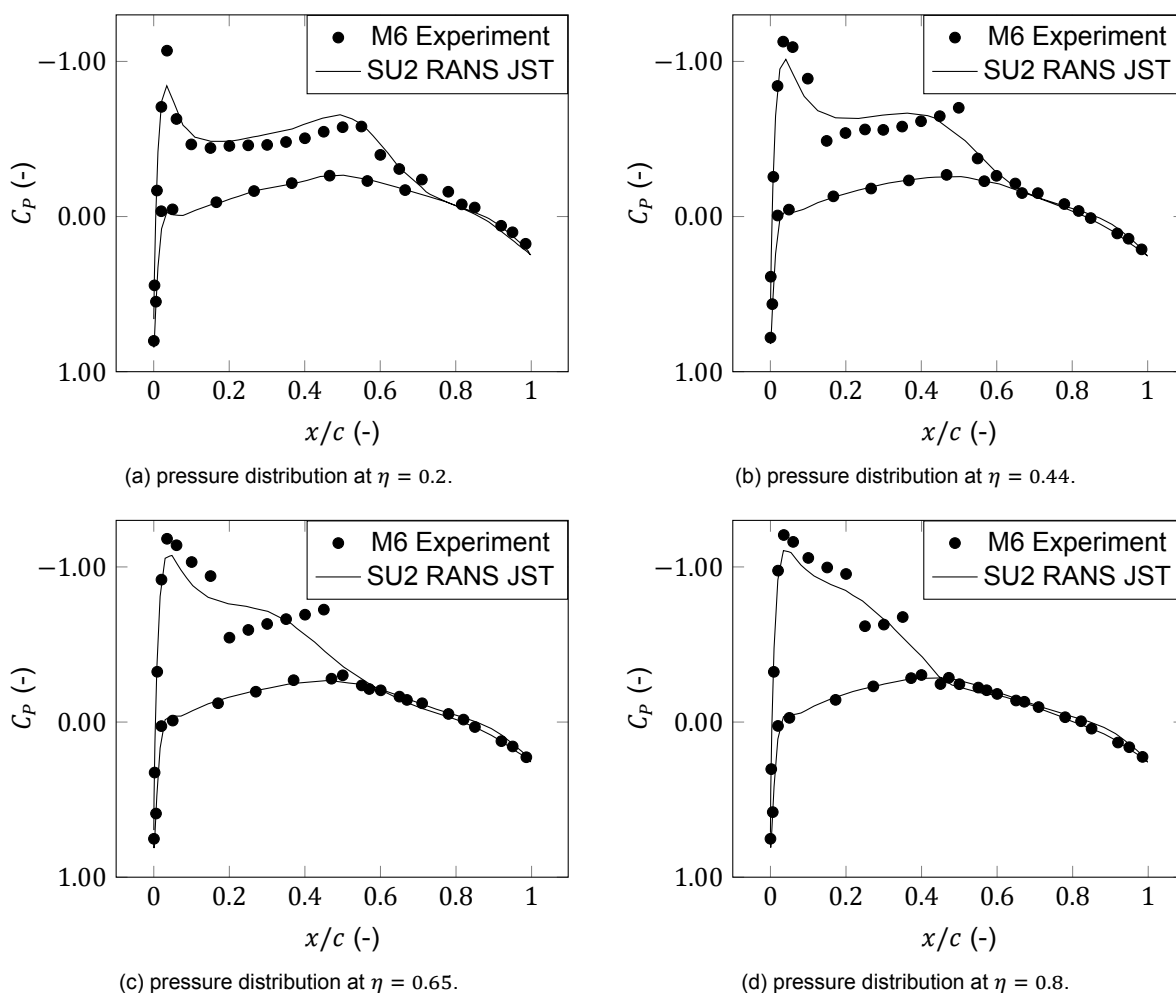


Figure 4.5: Pressure distributions of the SU2 RANS validation study using the ONERA M6 wing geometry.

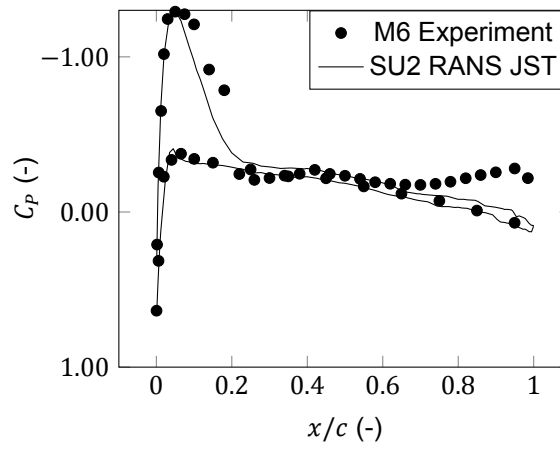
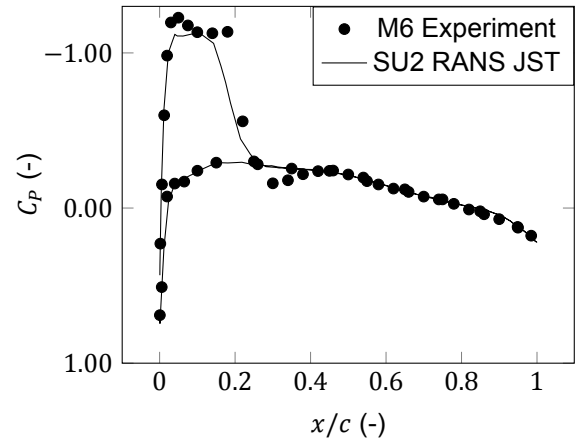
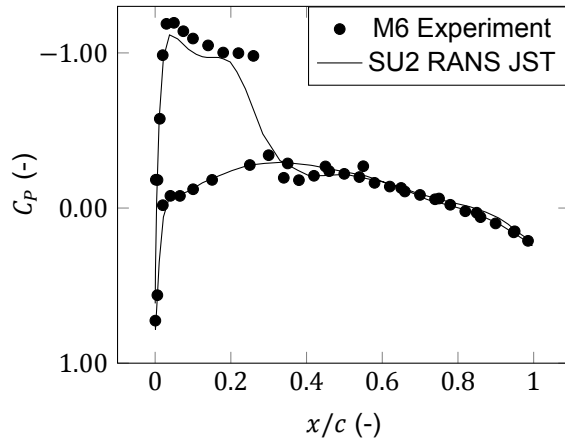


Figure 4.5: Pressure distributions of the SU2 RANS validation study using the ONERA M6 wing geometry.

5

Results and Discussion

The optimizations are performed at cruise conditions, where the aircraft is assumed to fly at a constant AoA of 3° . The conditions that are needed as inputs for SU2 RANS simulations are presented in Table 5.1. Here, Re is the Reynolds number, and T_∞ is the freestream temperature.

Table 5.1: Flight conditions used as inputs for SU2 RANS simulations.

Parameter	Value	Unit
α	3.0	deg
M	0.85	-
Re	8.4×10^7	-
T_∞	217	K

The Reynolds number regime is determined using the mean aerodynamic chord (MAC). Using a freestream viscosity, μ_∞ , of 1.4×10^{-5} Ns/m², a ρ_∞ of 0.27 kg/m³ at the cruise altitude of 13,000 m, and a v_{cruise} of 251 m/s based on the cruise Mach number Re can be calculated using Equation 5.1.

$$Re = \frac{\rho_\infty v_{\text{cruise}} \text{MAC}}{\mu_\infty} \quad (5.1)$$

The MAC, reference area, S_{ref} and x -location of the center-of-gravity, x_{cg} , used during the calculations are tabulated in Table 5.2. S_{ref} and MAC are calculated in ParaPy for the baseline design by Oosterom [19]. The center-of-gravity location is taken from his report. Note that each design's actual area and MAC in the optimization are different. However, to compare the dimensionless force coefficients, the reference values from Table 5.2 is used continuously.

Table 5.2: Reference values used throughout the calculations.

Parameter	Value	Unit
MAC	17.2	m
S_{ref}	796 .1	m ²
x_{cg}	26.3	m

The results of the optimizations of the cockpit and fairing shapes are presented in this chapter. First, the design steps are presented in section 5.1, after which the effects of adding an unoptimized nose cone and fairing to the baseline design will be discussed in section 5.2. This addition results in the unoptimized (UO) design. After that, the results of an optimization study, which is performed without the aerodynamics solver in place to construct a good first guess of a nose cone shape, are presented in section 5.3. This results in a nose cone that is only optimized to minimize the windshield dimensions, called the windshield optimized (WO) design. Subsequently, the optimized designs for both the nose cone (NCO) and fairing (FO) are given in section 5.4 and section 5.5, respectively. The

chapter is concluded by assessing the effect of combining both of the shapes in the aircraft geometry in section 5.6. This design is denoted by the combined optimized (CO) shapes design.

5.1. Design Stages

The aerodynamic design of the nose cone and fairing shapes have been conducted in a step-wise manner. This process is as follows:

1. The unoptimized nose cone and fairing shapes are added to the design. Existing aircraft designs inspire the nose cone, and the fairing is built not to favor an up- or down-swept trailing edge but to include the galley as stated in the requirements fully. The corresponding design vectors can be seen in Table 5.3 and in Table 5.4. The section numbers in the tables are taken from Figure 3.1b and Figure 3.2b.

Table 5.3: Overview of the nose cone design vector of the UO configuration.

Section	\bar{x}_{NC} (m)	\bar{z}_{NC} (m)
1	{1.92, 3.43, 3.78}	{2.02, 0.88, -1.86}
2	{1.68, 2.42, 4.26}	{1.85, 1.59, -1.56}
3	{1.54, 2.14, 3.17}	{1.60, -0.60, -1.25}
4	{0.51, 0.66, 0.91}	{1.19, -0.18, -0.80}
5	{-0.4, 0.0, -0.2}	{0.6, 0.05, -0.3}

Table 5.4: Overview of the fairing design vector of the UO configuration.

Section	x_{TE_F} (m)	z_{TE_F} (m)	\bar{x}_{u_F} (m)	\bar{z}_{u_F} (m)	\bar{x}_{l_F} (m)	\bar{z}_{l_F} (m)
1	23.8	-0.2	{17.0, 20.5}	{1.55, 1.5}	{17.0, 20.5}	{-1.5, -1.25}
2	23.7	-0.2	{18.0, 21.0}	{1.55, 1.5}	{18.0, 21.0}	{-1.45, -1.25}

2. The nose cone shape is optimized with the drag term in Equation 3.1 removed. This results in a nose cone that is purely optimized for the demands of shrinking the windshield area and the overnose windshield pane. The upper and lower bounds used for this optimization are tabulated in Table 5.5. Section 5 is kept unchanged throughout the optimization as its influence on the aerodynamic shape is small.

Table 5.5: Overview of the nose cone design vector bounds of the windshield optimization.

Section	Bound	\bar{x}_{NC} (m)	\bar{z}_{NC} (m)
1	Upper	{2.42, 3.93, 4.28}	{2.52, 1.38, -1.36}
	Lower	{1.42, 2.93, 3.28}	{1.52, 0.88, -1.86}
2	Upper	{2.18, 2.92, 4.76}	{2.35, 2.09, -1.06}
	Lower	{1.18, 1.92, 3.76}	{1.35, 1.09, -0.56}
3	Upper	{2.04, 2.64, 3.67}	{2.10, -0.10, -0.75}
	Lower	{1.04, 1.64, 2.67}	{1.10, -1.10, -1.75}
4	Upper	{1.01, 1.11, 1.41}	{1.69, 0.32, -0.30}
	Lower	{0.01, 0.11, 0.41}	{0.69, -0.68, -1.30}

3. Using the WO design as an initial guess, the nose cone is optimized again. This time, however, the drag term in Equation 3.1 is included in order to improve the aerodynamics of the feasible WO design. This optimization results in the NCO design. The bounds on the design space for this optimization step are given in Table 5.6. Again, section 5 is kept unchanged
4. From another PC, the fairing optimization runs. The nose cone geometry is kept constant, as in the UO design. The optimization of the fairing is performed using Equation 3.12 and results in the FO design. Table 5.7 displays the upper and lower bounds used.

Table 5.6: Overview of the nose cone design vector bounds of the nose cone optimization.

Section Number	Bound	\bar{x}_{NC} (m)	\bar{z}_{NC} (m)
1	Upper	{2.15, 4.05, 4.45}	{2.35, 1.15, -1.78}
	Lower	{0.65, 3.30, 3.70}	{1.35, 0.15, -2.78}
2	Upper	{2.05, 2.69, 4.46}	{2.87, 1.28, -1.30}
	Lower	{1.30, 1.94, 3.71}	{1.87, 0.28, -2.33}
3	Upper	{2.76, 3.48, 4.43}	{2.65, 0.24, -0.11}
	Lower	{2.26, 1.98, 2.93}	{1.65, -0.76, -1.11}
4	Upper	{1.83, 1.62, 1.80}	{1.51, 0.45, -0.33}
	Lower	{0.33, 0.11, 0.30}	{0.51, -0.55, -1.33}

Table 5.7: Overview of the fairing design vector bounds of the fairing optimization.

Section	Bound	x_{TE_F} (m)	z_{TE_F} (m)	\bar{x}_{u_F} (m)	\bar{z}_{u_F} (m)	\bar{x}_{l_F} (m)	\bar{z}_{l_F} (m)
1	Upper	27.0	0.3	{18.0, 21.5}	{2.05, 1.95}	{18.0, 21.5}	{-0.95, -0.65}
	Lower	23.0	-0.7	{16.0, 19.5}	{1.05, 0.95}	{16.0, 19.5}	{-1.95, -1.65}
2	Upper	27.0	0.3	{19.0, 22.0}	{2.05, 1.95}	{19.0, 22.0}	{-0.95, -0.65}
	Lower	23.0	-0.7	{17.0, 20.0}	{1.05, 0.95}	{17.0, 19.0}	{-1.95, -1.65}

- Finally, both optimized shapes are combined in the NCO design, and the forces are evaluated. It is important to assess the implications of the optimizations' decoupling.

5.2. From Baseline to Unoptimized Design

To begin with, the step in aerodynamic behavior when introducing the fairing and the cockpit shapes to the baseline design is presented here. The contents of the design vectors of the fairing and nose cone shape can be found in Table 5.3 and Table 5.4. However, as this step moves away from the flying wing concept and introduces bulkier parts to the aircraft, the pressure distribution does not improve necessarily.

From Figure 5.1, in Figure 5.1b, it can be seen that the shock strength of the most inboard shock is increased compared to the baseline design in Figure 5.1a. This is explained by the addition of the unoptimized fairing to the geometry. The shape has to accommodate the galley, which means that the rear part of the root airfoil also is increased in thickness, which increases superelevations over the rear part of the center-body. Another effect of the addition of the fairing is displayed by a slight decrease in suction in Figure 5.1b, halfway along the root chord at the streamwise attachment edge of the fairing. It can be seen that the root chord in the UO design is already extended.

Looking at the effects of the nose cone's addition on the upper surface pressure plot over the wing, similar behavior is observable at the attachment edge. Because of the non-continuous connection of the baseline wing and the new nose cone, a pressure peak along the attachment edge can be distinguished due to the concave geometry. Another notable change in the pressure distribution due to the nose cone is shown at the nose of the aircraft in Figure 5.1b. At the leading edge of the nose, high pressure is measured because of the stagnation in the flow at this point. Behind the stagnation point, the flow is accelerated over the crown of the nose cone. In the baseline design, the lift of the front part of the aircraft root is less prominent.

A comparison of the forces between the baseline and UO design can be made with the values organized in Table 5.8. It can be seen that C_D increases for the UO design. Notably, C_{D_p} increases more than C_{D_f} . This can be explained by looking at the pressure distributions in Figure 5.2. In Figure 5.2a, it can be seen that the shock moves aft, because of the high curvature of the fairing, and therefore increases in strength. The aft-moving of the shock causes an increase in aft suction, as a larger region of high superelevations is created. This causes an increase in pressure drag. At $\alpha=0.082$, which is a spanwise station outside of the nose cone and fairing geometries, the same effect of the shockwave moving aft can be seen, looking at Figure 5.2b. It can be seen that suction on the front of the wing is increased, because of the nose cone addition. However, looking at a wing station outside the nose cone shape, it can be seen that the aft suction stays prominent for longer.

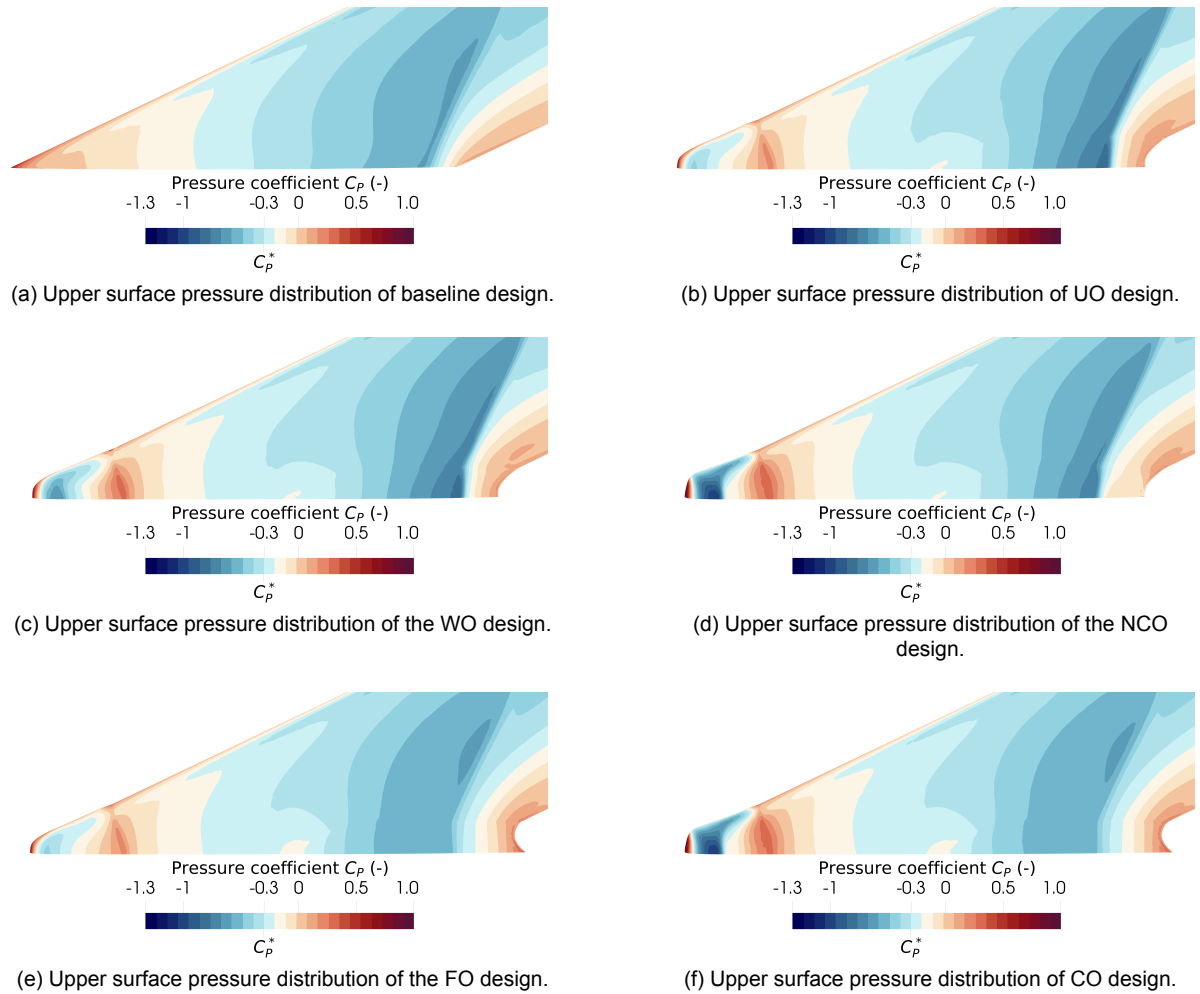


Figure 5.1: Comparison of the baseline, UO and optimized designs upper surface pressure distribution. Calculated at $M = 0.85$, $\alpha = 3^\circ$, $Re = 8.4 \times 10^7$. $C_p^* = -0.3$.

Table 5.8: Comparison of the aerodynamic force coefficients of the baseline, UO and optimized designs. Calculated at $M = 0.85$, $\alpha = 3^\circ$, $Re = 8.4 \times 10^7$.

Configuration	C_D (cts)	C_{D_p} (cts)	C_{D_f} (cts)	C_L (-)	C_m (-)	L/D (-)	S_{wet}	x_{CoP} (m)
Baseline	137.4	94.6	42.8	0.138	0.0700	10.07	880	23.5
UO	139.2	96.2	43.0	0.121	0.0574	8.71	882	22.1
WO	139.3	96.5	42.8	0.120	0.0567	8.64	883	21.9
NCO	135.9	93.1	42.8	0.114	0.0543	8.40	883	22.1
FO	133.7	90.1	43.0	0.125	0.0636	9.38	883	23.4
CO	134.6	91.7	42.9	0.126	0.0639	9.32	884	23.4

The small increase in friction drag can be interpreted as the result of a slight increase in wetted area that is introduced by the cockpit and fairing surfaces. Looking at Figure 5.3, it also becomes apparent that the large increase in overspeeds causes an increase in friction coefficient, which is counteracted by the large deceleration at the kinks. Furthermore, the pitching moment coefficient is decreased significantly. Looking at Figure 5.2b, a possible explanation is the more upstream occurrence of the upper surface shock than the lower surface shock. This causes a large lift loss at the rear part of the wing, shifting the pitching moment forward. Additional lift loss can be distinguished at the attachment edges of the nose cone and the fairing. The addition of the unoptimized shapes to the baseline design caused a significant L/D decrease of 1.3.

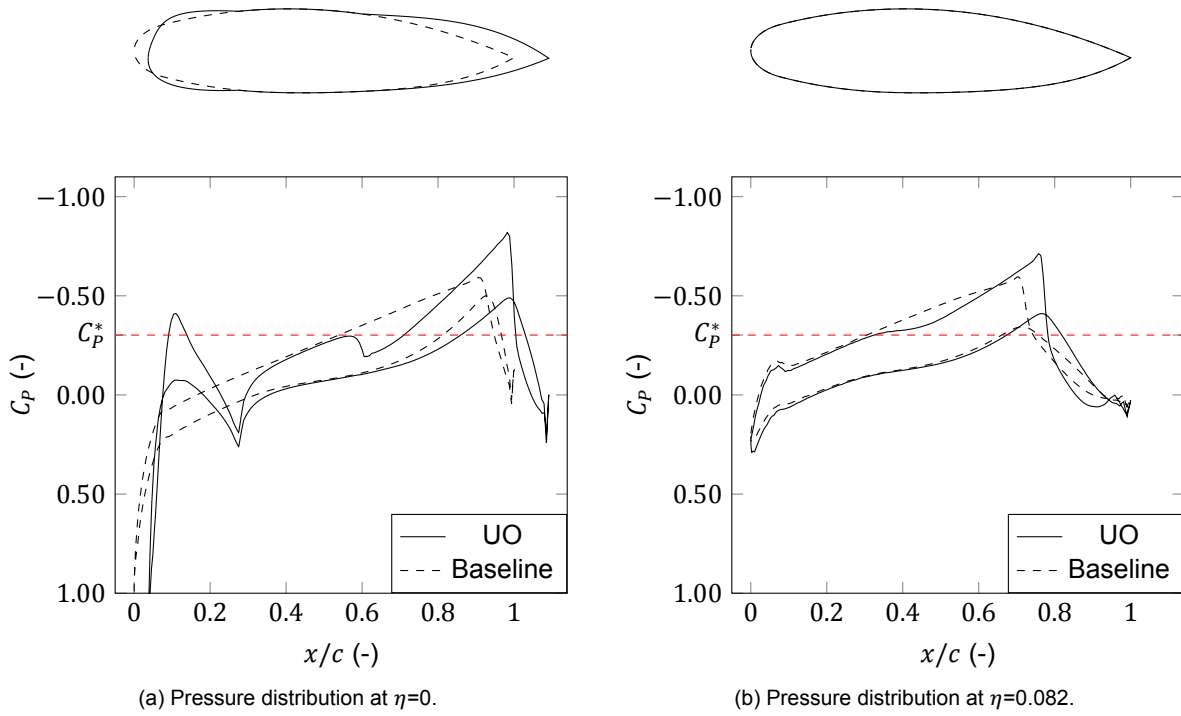


Figure 5.2: Pressure distributions of baseline design and UO design at two spanwise stations. Calculated at $M = 0.85$, $\alpha = 3^\circ$, $Re = 8.4 \times 10^7$. $C_p^* = -0.3$.

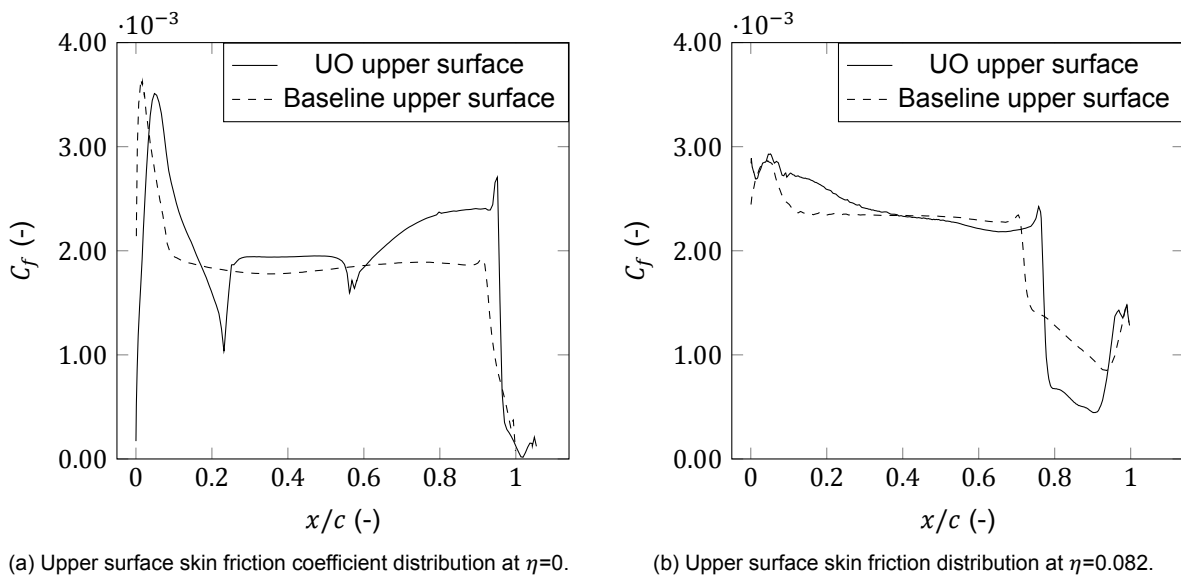


Figure 5.3: Upper surface skin friction coefficients of baseline design and UO design at two spanwise stations. Calculated at $M = 0.85$, $\alpha = 3^\circ$, $Re = 8.4 \times 10^7$.

Looking back at Figure 5.3a, it can be seen that the absolute magnitude of the friction coefficient decreases to close to zero after the shock for both the baseline design and the UO design. This behavior seen at the root can be ascribed to trailing edge separation and potentially increases the drag by the low pressure wake that trails the wing. Figure 5.3b shows that at a $\eta = 0.082$, the shock decreases the velocity and therefore the friction coefficient, but it does not result in separation.

5.3. Windshield Optimization

The first configuration of the nose cone shapes discussed is the WO design. Table 5.9 shows the design parameter values of the optimized nose cone geometries. In Figure 5.1c, the upper surface pressure distribution of the WO design can be seen. It is apparent that the curvature of the nose cone crown is increased when looking at the front of the aircraft. The pressure peak due to the junction between the nose cone and the base wing geometry is increased, indicating a larger kink due to the increased curvature of the crown. Moreover, it can be noted that the shape that resulted from the windshield optimization does not alter the shape of the isobars on the rear center-body. The shock is positioned at the same location, and the severity did not increase.

Table 5.9: Overview of the nose cone design vectors of the UO and the NCO designs.

Section Number	Windshield Optimized		Nose Cone Optimized	
	\bar{x} (m)	\bar{z} (m)	\bar{x} (m)	\bar{z} (m)
1	{1.40, 3.30, 3.70}	{1.85, 0.65, -2.28}	{1.71, 2.60, 4.20}	{2.00, 0.56, -2.00}
2	{1.30, 1.94, 3.71}	{2.37, 1.28, -1.83}	{1.04, 2.34, 4.00}	{2.23, 1.48, -2.06}
3	{2.01, 2.73, 3.68}	{2.15, -0.26, -0.61}	{2.27, 2.78, 3.25}	{2.27, -0.16, -1.65}
4	{1.08, 0.87, 1.05}	{1.01, -0.054, -0.83}	{0.39, 0.20, 1.30}	{1.83, 0.25, -0.88}

The increase in crown curvature can also be deduced from the front view of the nose cone pressure plot in Figure 5.4b when comparing it to Figure 5.4a. It can be seen that the crown is raised, creating an area of higher overspeeds on the top surface. The remainder of the nose cone pressure distribution is similar to the baseline design in Figure 5.4a.

It can be seen that the aerodynamic forces are similar to the values that were found for the baseline design when looking at the aerodynamic forces in Table 5.8. The largest change can be found in the C_L . From the pressure distributions in Figure 5.5, it becomes apparent that the reason for this is the increased lift loss at the junction between the two surfaces. The pressure distribution further downstream can be seen to be roughly equal to the baseline design, as is observed in Figure 5.1d. The suction peak is raised considerably with respect to the UO design, and larger overspeeds are acquired. However, the suction gain on the front is not enough to counteract the momentum loss from the shock that it introduces. It can be seen that at $\eta = 0.082$, the influence of the WO shape on the front suction is negligible.

In Figure 5.6a it can be seen that the skin friction after the kink is smaller for the WO design, indicating smaller velocities. This can be explained by the deceleration that occurs due to the larger kink. Moreover, the same trailing edge separation can be seen for the WO design as C_f plummets to zero.

In Table 5.10, the dimensions of the windshield and the viewpoint distance and angle of the three configurations are compared. It can be seen that the cockpit with the WO shows a significant decrease in all three of the windshield dimensions. The WO design has an increase of roughly 30% in windshield dimensions with respect to the A320 and A350 [30]. Looking at the image of the WO design, including the components in Figure 5.7b, it can be deduced that the optimizer converged towards a geometry in which the pilot is seated higher than in the baseline, with a blunter nose, in order to minimize the height of the overnose window pane. However, looking at the aerodynamic shape, it is not expected that the slits under the nose cone shape are aerodynamically favorable. For images of the realistic windshields for the optimized nose cones, the reader should refer to Appendix B.

Table 5.10: Windshield dimensions and pilot view parameters of the different nose cone configurations.

Configuration	$S_{WS_{min}}$ (m ²)	$S_{WS_{real}}$ (m ²)	$S_{WS_{SON}}$ (m ²)	$h_{WS_{SON}}$ (m)	l_{VP} (m)	ϕ_{VP} (deg)
UO	4.2	4.7	0.73	0.49	1.07	45
WO	2.0	3.0	0.28	0.042	0.59	35
NCO	2.3	3.5	0.27	0.057	0.61	36

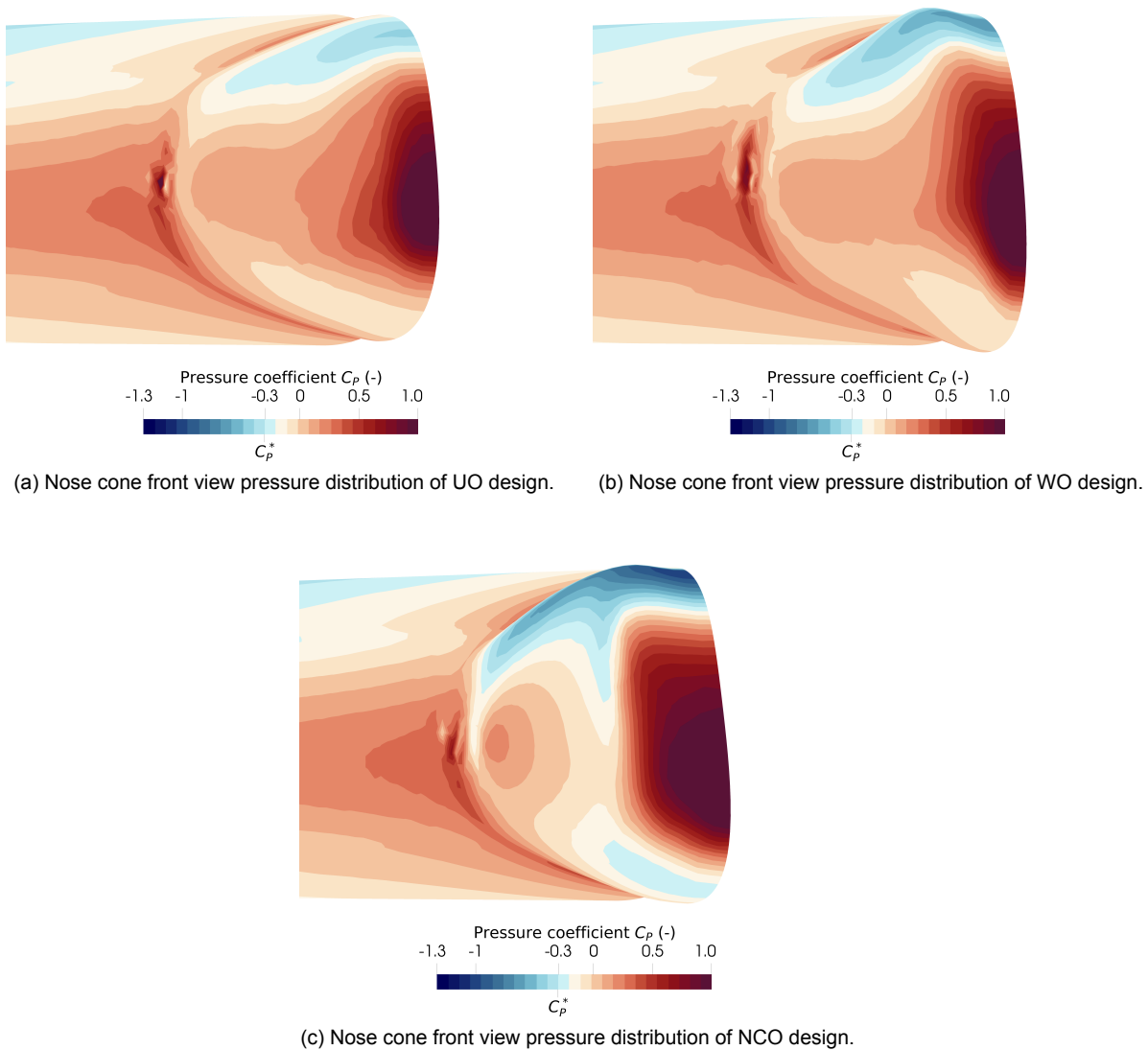


Figure 5.4: Comparison of the pressure distributions of the three nose cone designs. Calculated at $M = 0.85$, $\alpha = 3^\circ$, $Re = 8.4 \times 10^7$. $C_p^* = -0.3$.

5.4. Nose Cone Optimization

The design vector for the NCO design can be seen in Table 5.9. The upper surface pressure distribution of the FV aircraft with the NCO can be seen in Figure 5.1d. It becomes evident that the suction over the crown of the nose cone is increased with respect to both the baseline design and the WO design. The pressure peak at the junction is also increased, which indicates that the optimizer prefers increasing the curvature to improve suction on the front and create a higher seating spot for the pilots, which reduces the window pane size, as is seen with the WO design. The large overspeeds on the crown are confirmed in Figure 5.1d. It can be seen that this design has a blunter center, which is beneficial for achieving the required overnose angle. On the side of the nose cone, the optimizer has chosen a more aerodynamically shaped geometry, which can be deduced from the lower pressure coefficients in Figure 5.1d when compared to Figure 5.1b and Figure 5.1c.

Looking back at Table 5.8 a significant decrease in C_D can be seen. From the pressure distributions in Figure 5.5, it can be seen that the addition of the NCO causes a significant increase in suction peak height on the front of the wing, which contributes to the reduction in pressure drag. The pressure coefficients around the semi-chord are almost identical to the baseline. Furthermore, towards the rear of

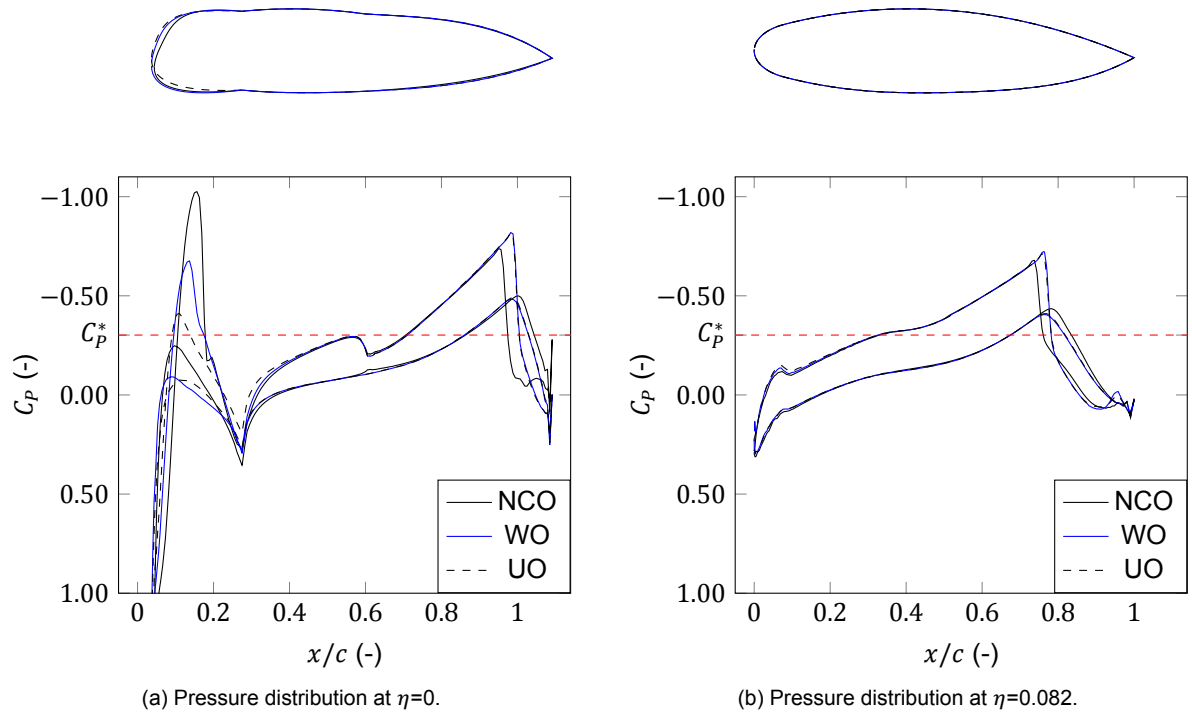


Figure 5.5: Pressure distributions of UO, WO and NCO designs at different spanwise stations. Calculated at $M = 0.85$, $\alpha = 3^\circ$, $Re = 8.4 \times 10^7$. $C_p^* = -0.3$.

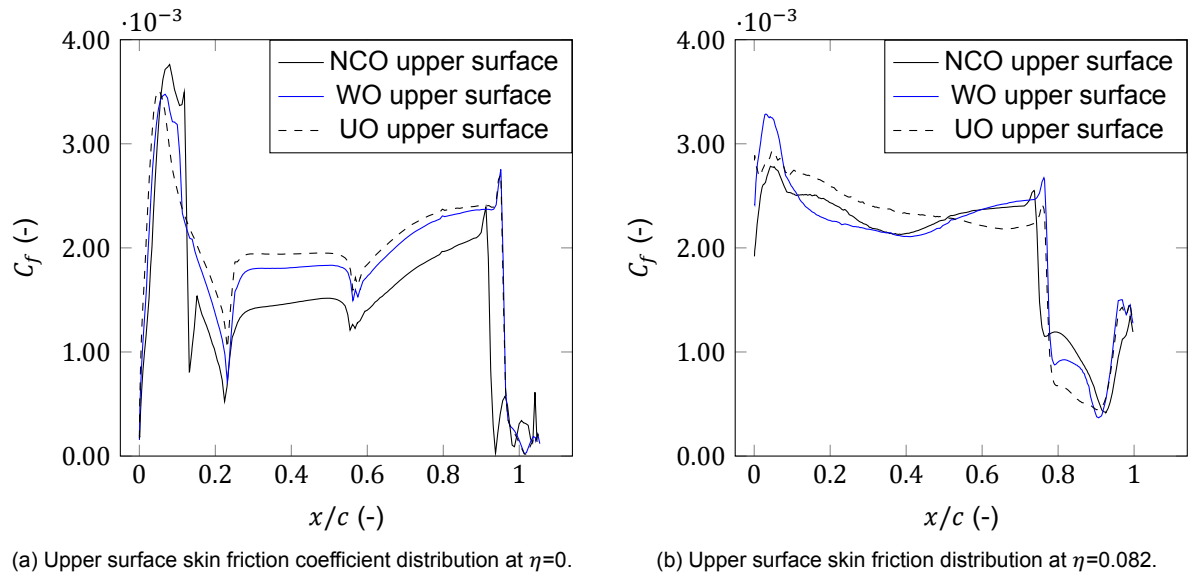


Figure 5.6: Upper surface skin friction coefficients of UO, WO and NCO designs at two spanwise stations. Calculated at $M = 0.85$, $\alpha = 3^\circ$, $Re = 8.4 \times 10^7$.

the wing, the pressure lines trail the same path. However, the upper surface shock is shifted upstream, shifting the isobars forward. The upstream shift indicates lower superelevations upstream of the shock, which can be attributed to the large kink's adverse pressure gradient at the large kink. The reductions in aft suction and shock strength decrease both the pressure drag and the wave drag. Even at the station outside of the nose cone geometry, as is shown in Figure 5.5b, these effects can be seen. A significant part of the lift reduction in Table 5.8 can be accredited to the upstream shift. The lower surface flow is terminated in a shock later than the upper surface flow. This creates a big lift loss on the

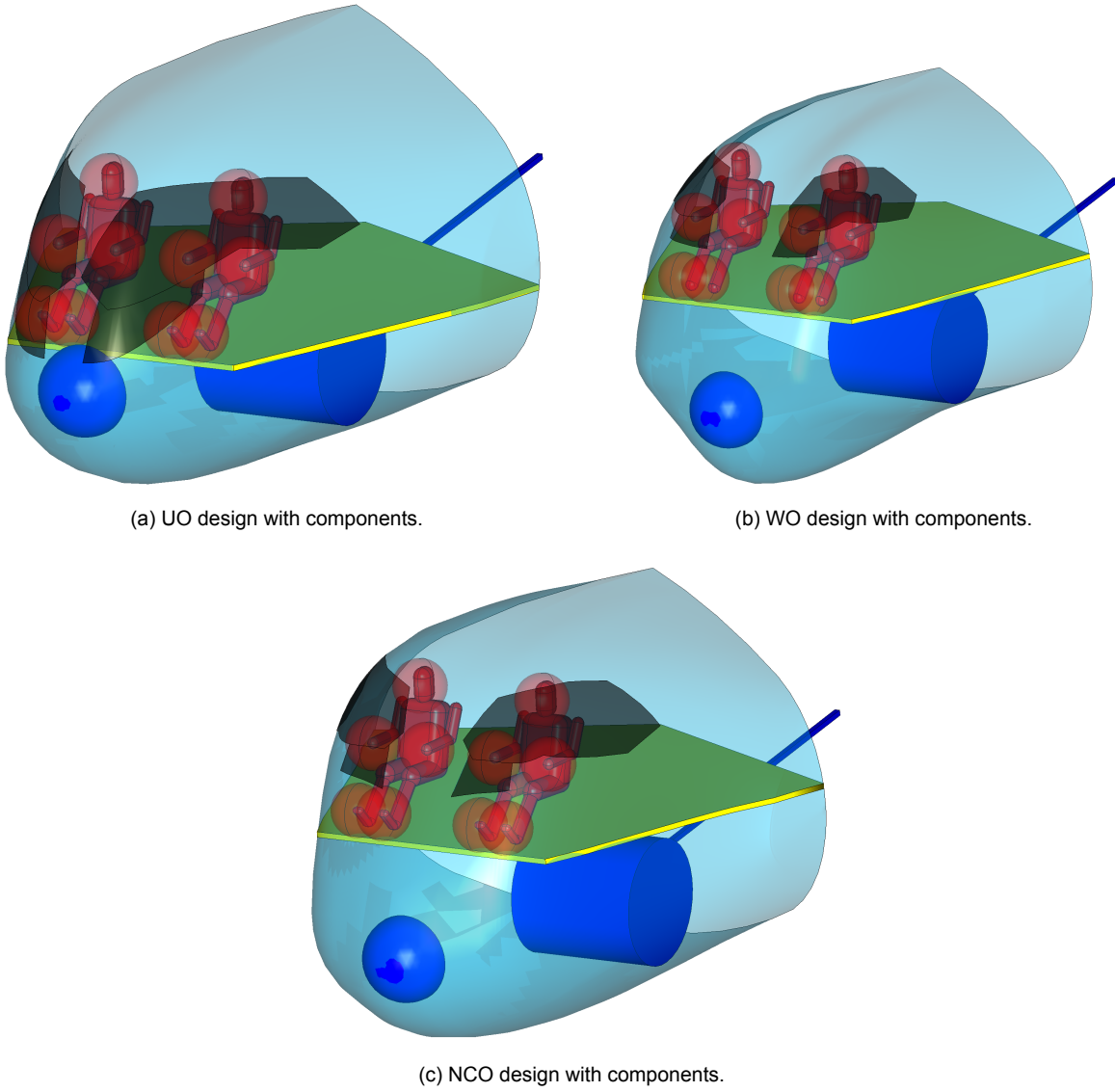


Figure 5.7: Overview of three different nose cone configurations.

rear wing. Even though this causes the CoP to be further upstream, the reduction in lift still accounts for a significant reduction in the positive pitching moment coefficient.

The instantaneous deceleration can deduce from Figure 5.6a that the suction peak over the crown is terminated in a shockwave. As C_f does not go to zero here, it can be derived that no separation occurs. After the rear shock, however, separation can be seen. Figure 5.5a confirms this as the rear upper surface pressure line does not follow the contours of the geometry anymore. Furthermore, it occurs more upstream than for the UO and WO designs. This indicates a larger drag contribution of the low-pressure wake that trails the rear wing. However, the force coefficients show that this is counteracted by the increase in front suction and the forward sweeping of the shockwave.

Looking at Table 5.10, it can be seen that S_{WS} and $h_{WS_{ON}}$ have increased with respect to the windshield optimized configuration as the multi-objective cost function used for the nose cone optimization also incorporated the drag coefficient. Despite that, it does show an appreciable decrease in windshield size with respect to the baseline design, which can also be seen in Figure 5.7c. This shows that the desirable geometries for minimizing the windshield area and the drag coefficient are not strictly conflicting. Moreover, looking back at the theory from section 2.1, it can be seen that the increased thickness of the front of the wing is also a virtue for root design.

5.5. Fairing Optimization

Moving towards the fairing design, the optimal shape design vector can be seen in Table 5.11. Looking back at Figure 5.1, the upper surface pressure distribution of the optimized fairing is plotted in Figure 5.1e. It becomes apparent that the optimizer made an effort to reduce the strength of the inboard shock. It can be seen that the rapid decrease in pressure coefficient is less apparent, and the part of the wing over which the suction is highest is more spread. Moreover, the root chord is extended and curves upward, resulting in a small upswept tail, which is in line with applying negative camber for improving root aerodynamics, as was introduced in section 2.1.

Table 5.11: Overview of the fairing design vector of the FO configuration.

Section Number	x_{TE}	z_{TE}	\bar{x}_u	\bar{z}_u	\bar{x}_l	\bar{z}_l
1	24.94	0.20	{16.97, 19.84}	{1.76, 1.34}	{17.13, 20.59}	{-1.67, -1.17}
2	23.94	0.40	{17.52, 20.32}	{1.70, 1.06}	{18.11, 21.00}	{-1.65, -1.25}

Looking at the comparison of the baseline design and the FO pressure distributions in Figure 5.8, it is confirmed that the optimizer has converged towards a solution in which the aft loading is decreased notably. Evidently, from the pressure distributions, it can be deduced that the convexity of the lower surface is increased as the aft pressure coefficient is lower. The shock on the upper surface has shifted forward and has decreased in size significantly. The decrease in aft lift contributes to the omittance of the pressure drag. Furthermore, the decrease in suction on the rear wing also contributes to reducing C_D by lowering the pressure drag. Finally, the reduction in shock strength hints at a smaller momentum loss. All effects protrude towards stations outside of the fairing geometry, which is indicated in Figure 5.8b. It is interesting to note that the influence of the fairing shape on outer stations is more prominent than for the nose cone.

The small lift increase for the FO design can be accredited to a decrease in lift loss on the rear wing. By shifting the shockwave forward, the upper and lower surface shocks move closer, alleviating the negative lift.

Looking at the skin friction coefficient curve of the upper surface in Figure 5.9a it can be seen that the trailing edge separation in the UO design has been fixed for the FO design. This suggests that an additional reduction in pressure drag is experienced. The skin friction curve at $\eta = 0.082$ is similar to the UO design, as can be seen in Figure 5.9b.

5.6. Coupled Performance

Finally, the upper surface pressure distribution of the FV aircraft with both optimized shapes is plotted in Figure 5.1f. The effects that can be distinguished for the decoupled shapes can also be found in this graph. The high overspeeds over the crown of the nose cone can clearly be distinguished from the contour plot and the reduction of the shock strength over the fairing surface.

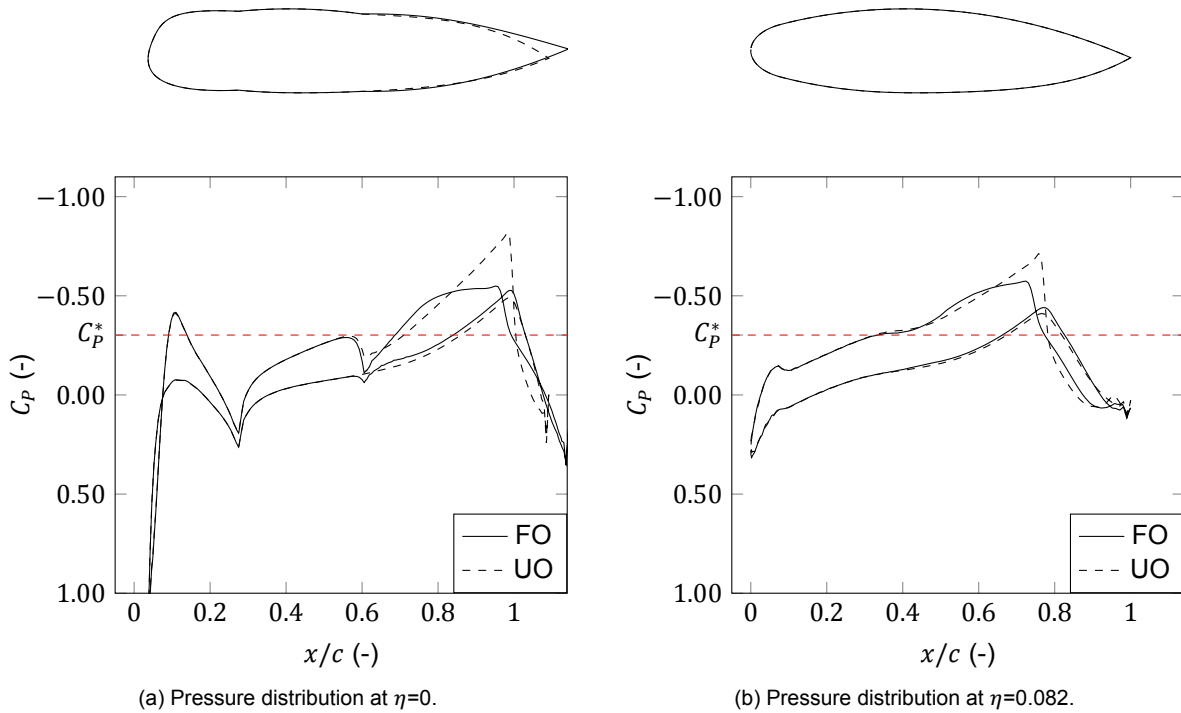


Figure 5.8: Pressure distributions of UO and FO designs at two spanwise stations. Calculated at $M = 0.85$, $\alpha = 3^\circ$, $Re = 8.4 \times 10^7$. $C_p^* = -0.3$.

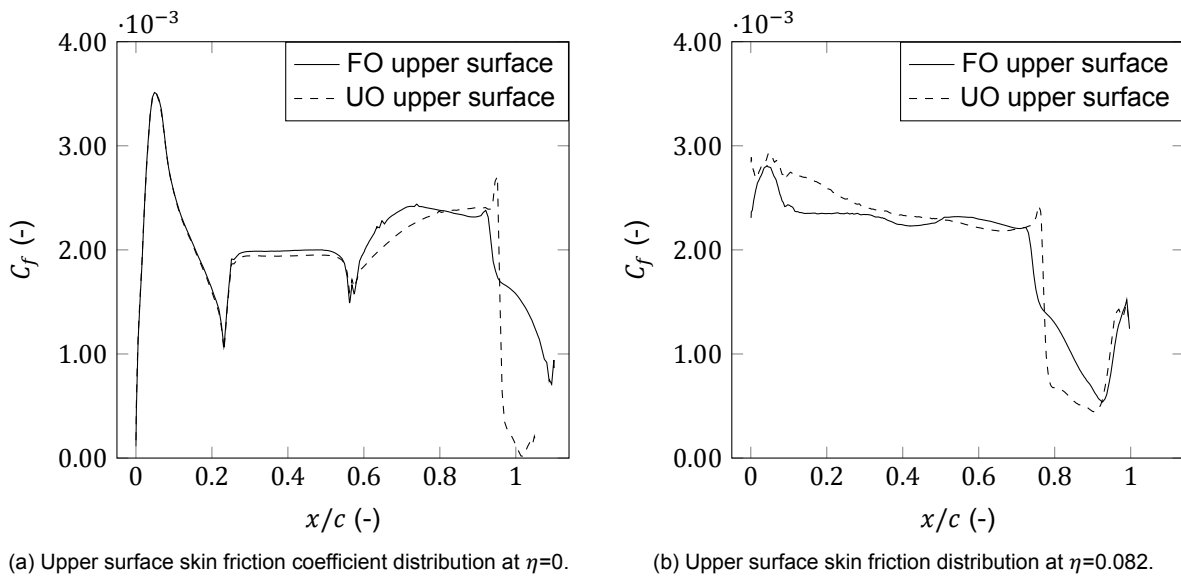


Figure 5.9: Upper surface skin friction coefficients of UO and FO designs at two spanwise stations. Calculated at $M = 0.85$, $\alpha = 3^\circ$, $Re = 8.4 \times 10^7$.

Looking at the pressure distributions in Figure 5.10, it can be seen that the pressure curves of the combined optimized shapes follow the distribution from the nose cone for the front part of the wing. Around $x/c = 0.4$, the pressure distribution transitions and tends towards the FO lines. Also, this behavior is apparent for the spanwise station outside of the nose cone and fairing shapes. It can be deduced that the coupled configuration combines the high suction of the nose cone crown and the reduced aft loading from the fairing. However, the addition of the nose cone shape does not shift the shock upstream as visibly as it did for the UO design.

Looking at Figure 5.11a, it can be seen that for the majority of the root section, the skin friction curve follows the shape of the NCO skin friction curve because of the large deceleration at the kink geometry. Furthermore, the skin friction coefficient goes to zero at the trailing edge, indicating separation. This notion can be used to verify the increase in pressure drag of the CO design with respect to the NCO and FO designs. This setback with respect to the FO design, which has the most favorable drag coefficient, can be attributed to the rapid growth of the boundary layer behind the shockwave at the crown.

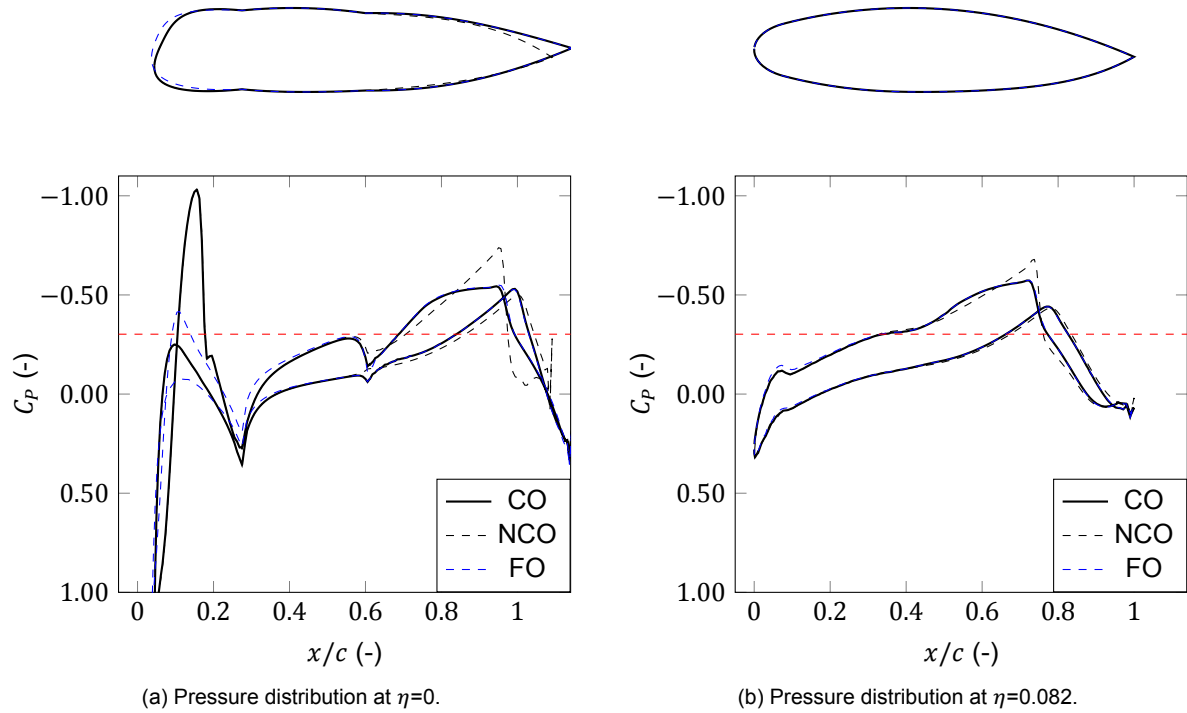


Figure 5.10: Pressure distributions of CO, WO and NCO designs at two different spanwise stations. Calculated at $M = 0.85$, $\alpha = 3^\circ$, $Re = 8.4 \times 10^7$. $C_p^* = -0.3$.

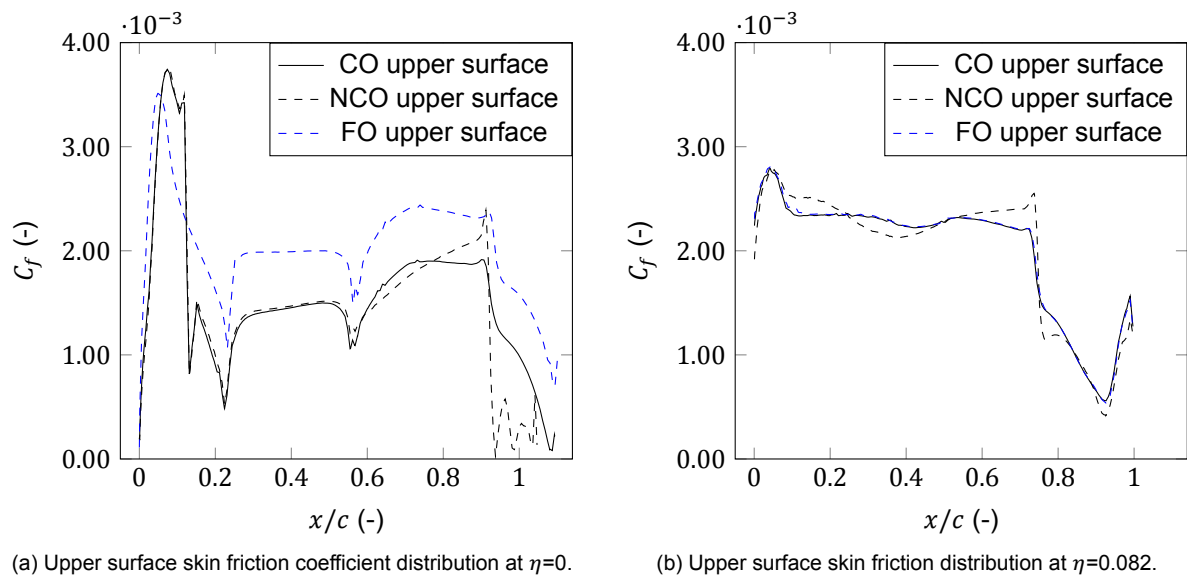


Figure 5.11: Upper surface skin friction coefficients of CO, WO and NCO designs at two spanwise stations. Calculated at $M = 0.85$, $\alpha = 3^\circ$, $Re = 8.4 \times 10^7$.

5.7. Mesh Density Sensitivity

A brief study is performed on the sensitivity of the numerical optimization solution to spatial discretization. It was already discussed in chapter 4 that a considerable error is introduced in the aerodynamic analysis in this project, making it essential to verify whether it has influenced the results.

A summary of the force coefficients of the various designs is given in Table 5.12. It can be seen that the drag coefficient of the CO design is increased when compared to the UO design. Both the NCO and FO designs show a decrease in the drag coefficient. However, it can be seen that the drag coefficient values converge toward each other, and the aerodynamic gains become smaller. Therefore, it can be noted that the optimizer depends on the spatial discretization chosen. Furthermore, looking at these values, together with the values from Table 5.8, it becomes questionable whether the aerodynamic design of a highly constrained nose cone and a fairing with a small span can change a lot in the aerodynamics.

Table 5.12: Comparison of the aerodynamic force coefficients of the baseline, UO and optimized designs. Calculated at $M = 0.85$, $\alpha = 3^\circ$, $Re = 8.4 \times 10^7$ and a volume mesh with 10 Million cells.

Configuration	C_D (cts)	C_{D_p} (cts)	C_{D_f} (cts)	C_L (-)	L/D (-)
Baseline	133.0	89.8	43.2	0.140	10.5
UO	130.1	87.6	43.3	0.109	8.3
NCO	128.7	85.5	43.2	0.104	8.1
FO	129.0	86.3	43.3	0.129	9.9
CO	131.5	88.2	43.3	0.130	9.9

Looking at the pressure distributions that compare the CO design for the original mesh and a finer mesh in Figure 5.12, it can be seen that the mesh error does not originate from the incorrect resolving of the shock. Instead, the curvature is changed by a small amount. It can therefore be concluded that the added modifications, which were in line with the theory from section 2.1, are still a virtue and that the optimizer functions as it should.

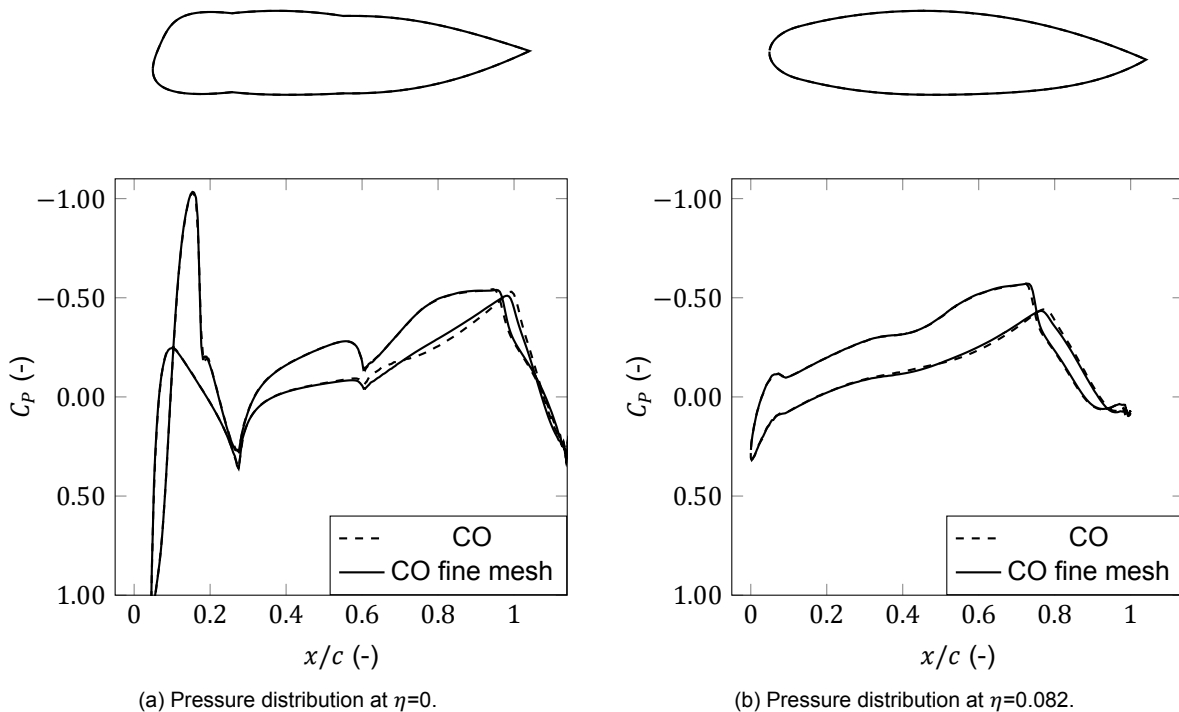


Figure 5.12: Pressure distributions of CO design with comparison of coarse and fine mesh. Calculated at $M = 0.85$, $\alpha = 3^\circ$, $Re = 8.4 \times 10^7$ and $S_{ref} = 398 \text{ m}^2$. $C_p^* = -0.3$.

6

Conclusions and Recommendations

This study aims to design a nose cone and a trailing edge fairing using a numerical optimization that employs the RANS equations. In order to achieve this, a method is established that runs aerodynamic analyses on a High Performance Computing cluster at TU Delft. Numerical flow simulations and constraints are simultaneously evaluated, on a PC and HPC12, respectively. This enables numerical optimization with the RANS equations, where the maximum time spent on one evaluation is set to two hours.

A parametric model for both of the shapes is established in this effort. Being based on the native ParaPy class `BSplineCurve`, the models are robust and readily extensible for future research. The nose cone is modeled using 24 design variables, and the fairing with 20 design variables in this study.

The design space of the nose cone is bound by the pilot seating position, the windshield area, and the inclusion of the pilots, nose landing gear, and weather radar. In order to accurately assess the constraints, these components are repositioned at each function evaluation in simplex optimizations. The fairing is only bound by the center-body galley size constraints, which can be evaluated with a more conventional approach.

In parallel, the shapes are optimized at two different PCs. The differential evolution algorithm decreases the drag coefficient at a Mach number of 0.85 and a cruise altitude of 13,000 m. The improved nose cone shape resulted in a 2.4% decrease in drag with respect to the unoptimized design and a 1.3% decrease with respect to the baseline Flying-V. In addition, the overnose windshield pane was decreased by 88% in comparison to the unoptimized design. This results in a total windshield area that is 50% larger than for typical windshields in reference aircraft.

The optimal fairing shape invokes a drag reduction of 4% with respect to the unoptimized design and 2.7% with respect to the baseline Flying-V. Because of the optimal fairing shape, the trailing edge separation seen for the baseline design is omitted, which largely explains the drag reduction.

Coupling the two shapes results in a drag reduction of 3.3% compared to the unoptimized design and 2.0% compared to the baseline Flying-V. Trailing edge separation is introduced back into the aerodynamic phenomena. This is attributed to the thicker boundary layer due to the shock over the highly curved nose cone crown, which was not present in the optimal fairing design.

A brief study examines how sensitive the results of the optimization are to the mesh density. It is shown that the drag coefficients of the various designs converge toward each other. The differences in the aerodynamic gains from the optimal fairing and the optimal nose cone become smaller, and the drag coefficient of the coupled shapes is not smaller than the unoptimized design. It can be seen that achieving aerodynamically good designs with a highly constrained nose cone and a thin fairing is challenging. This should be considered when opting to do further research on these shapes.

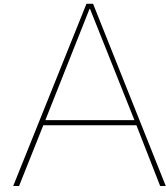
6.1. Recommendations

To improve a future nose cone and fairing design the following recommendations are postulated:

- The parametric models are built to make them easily extensible to generate more complex geometries and potentially open the opportunity for a smoother continuity between the nose cone -

wing and the fairing - wing connections, despite the large curvatures required by the constraints. Furthermore, additional design control could be gained by including the y -positions of the nose cone and fairing curves in the numerical optimization.

- ParaPy is a fast-improving platform. Curve classes that enforce continuity are already available, but they are not suitable for numerical optimization because of the considerable computational cost. However, pre-built classes for more complex shapes are constantly added, with the latest addition being the `GordonSurface` class. Gordon surfaces are used to generate more complicated shapes through a collection of curves. These classes can be employed to improve the connection of the nose cone and the fairing with the base wing geometry. Improving the outer wing with GordonSurfaces also enables analysing the off-design aerodynamics accurately in future studies.
- To ensure a smooth connection between the wing geometry and the center-body shapes, a complete redesign of the center body airfoils can be performed. The early down curving of the mid-airfoil curves is then avoided by performing a conventional airfoil design study with the galley and cockpit constraints included.
- It is shown that spatial discretization can introduce a considerable error for a RANS study. Furthermore, it is demonstrated that the sensitivity of the results to the mesh density can be significant. Therefore, in a subsequent shape optimization that employs a similar method to couple RANS simulations with HPC12, more time should be allocated to the optimization runtime. This allows for considering denser meshes and therefore mitigating the error.
- The pilots are seated high in the nose cone to decrease the overnose windshield pane size. However, the overnose windshield pane is not entirely omitted, and the dashboard should not obstruct viewing through this pane. In order to verify the feasibility of such a cockpit design with high seating and an unconventional dashboard, a detailed study of the interior of the cockpit should be conveyed.
- Structural design of the windshield is not included in this study. However, to form an understanding of the implications of structural reinforcement and the introduction of additional weight that corresponds to that, an in-depth study on the penetrability of the glass windshield should be performed.
- In order to alleviate the need for a high overnose angle that was demonstrated, research needs to be done on methods that allow for alleviating the approach visual requirements. Possible innovations that can accelerate this are, for instance, augmented vision landings or nose cameras. For now, these methods are not certifiable yet.



Additional Pressure Distributions

This appendix displays the pressure distributions that were seen in chapter 5 and compares them to other spanwise stations. This gives a better insight into the spanwise shape and performance of the nose cone and fairing shapes. Because of the similarities in the pressure distributions they were intentionally removed from the text.

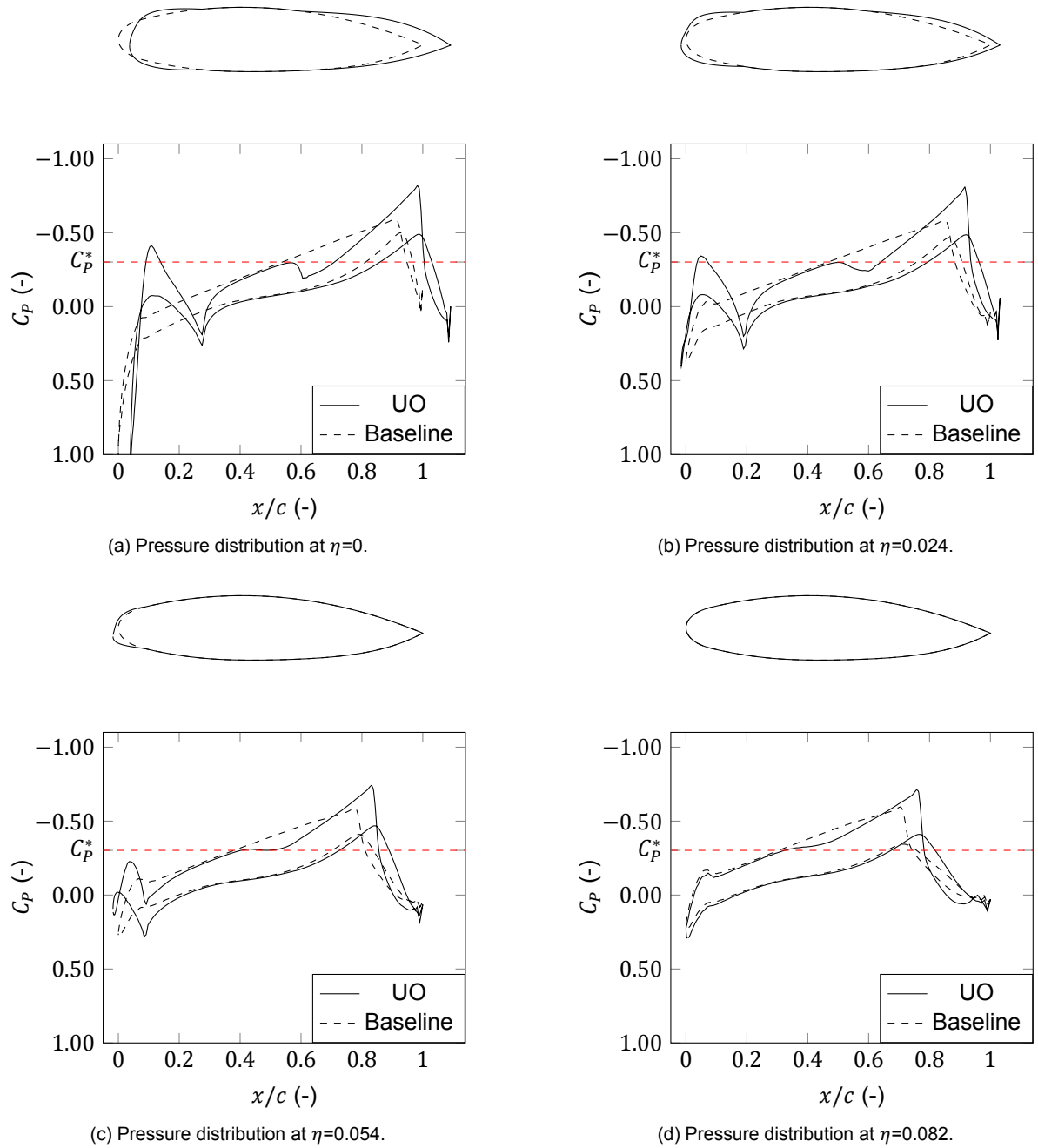


Figure A.1: Pressure distributions of baseline design and UO design at different spanwise stations. Calculated at $M = 0.85$, $\alpha = 3^\circ$, $Re = 8.4 \times 10^7$. $C_p^* = -0.3$.

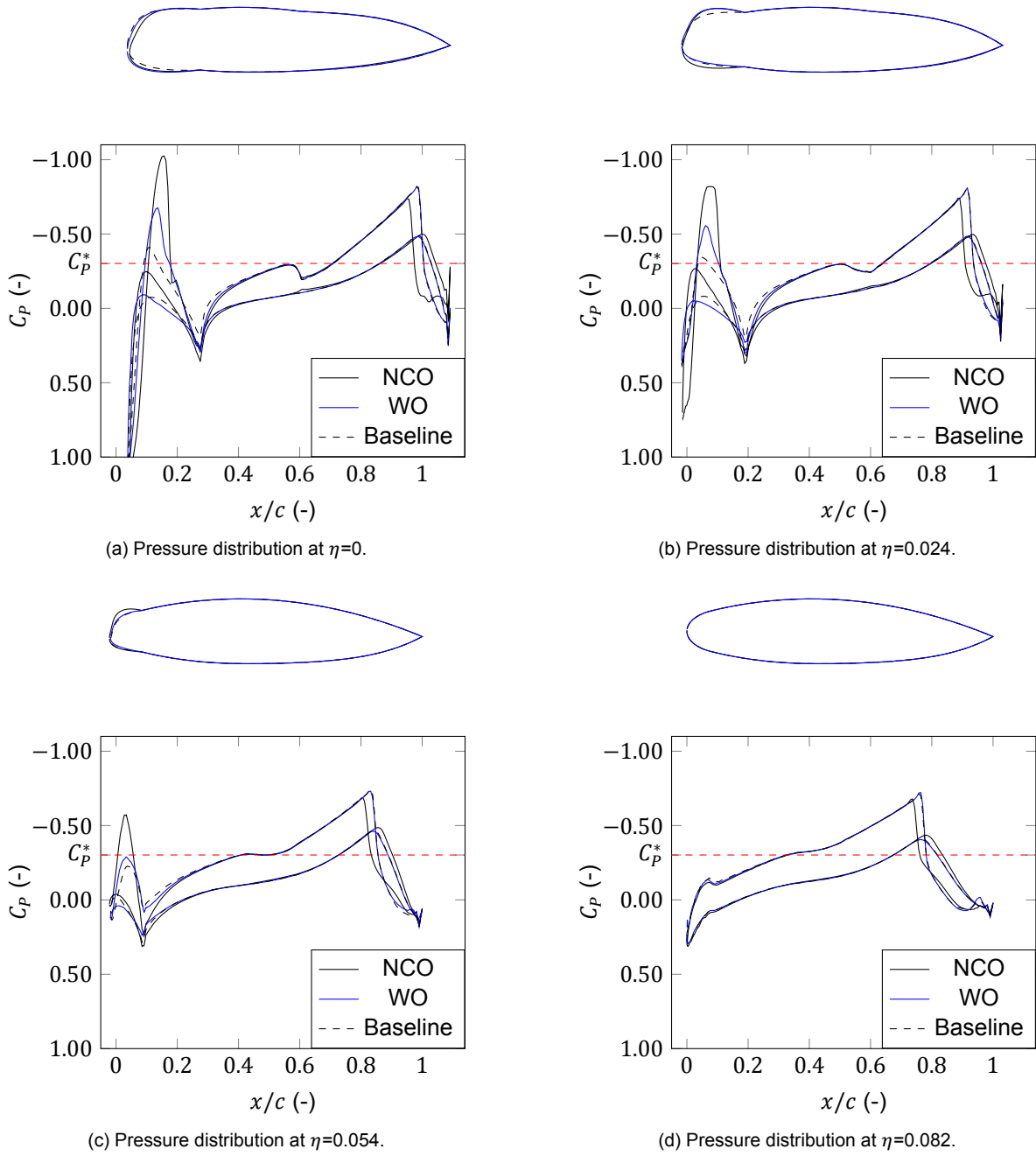


Figure A.2: Pressure distributions of UO, WO and NCO designs at different spanwise stations. Calculated at $M = 0.85$, $\alpha = 3^\circ$, $Re = 8.4 \times 10^7$. $C_p^* = -0.3$.

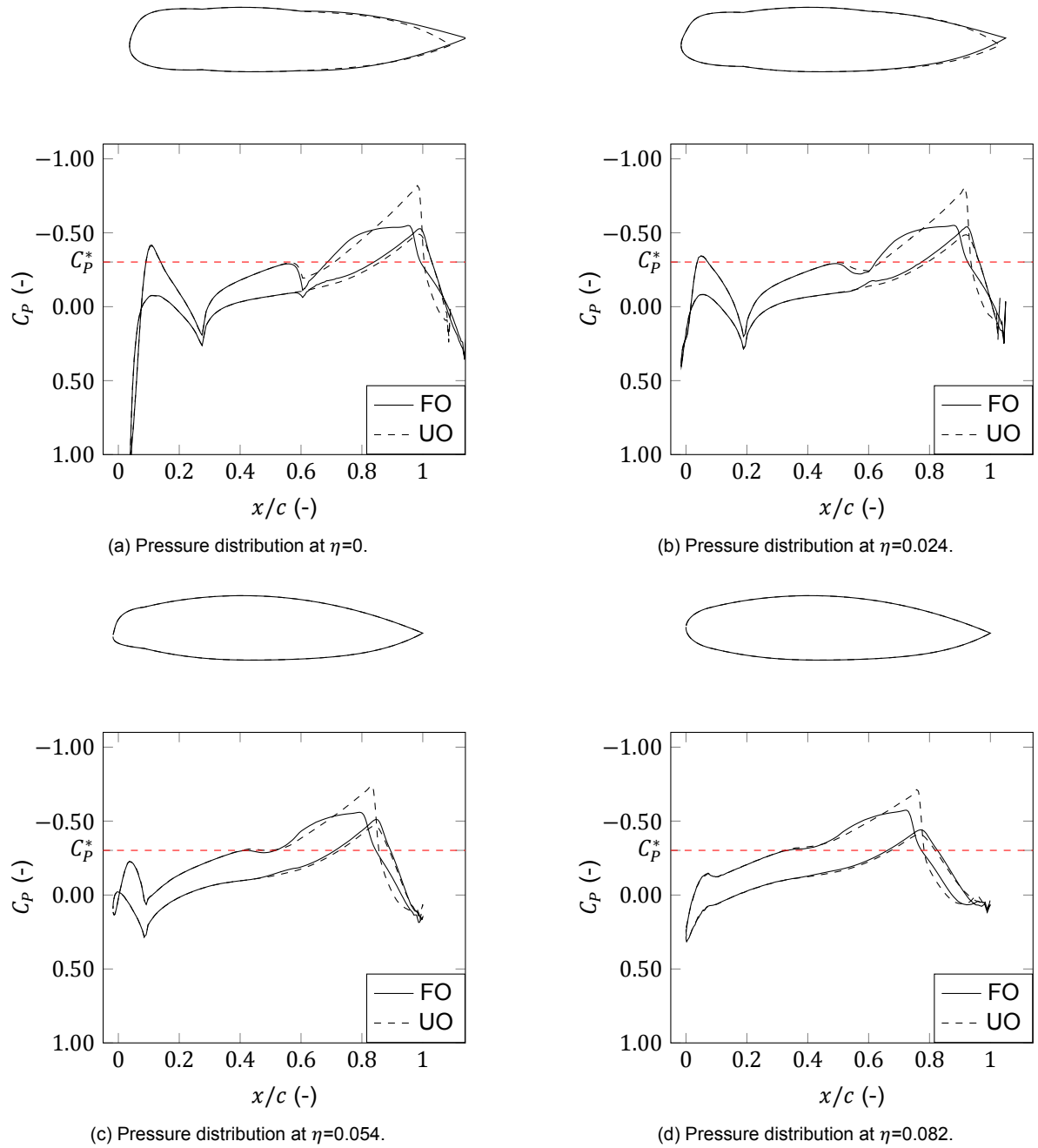
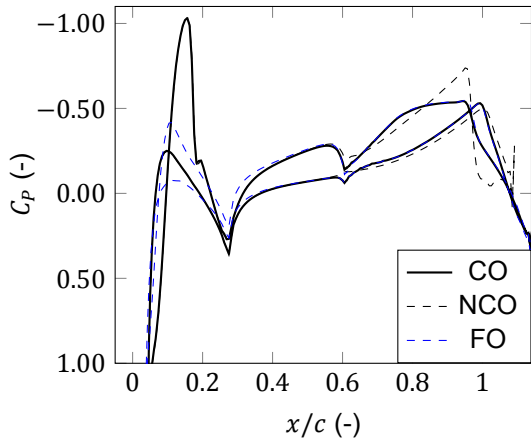
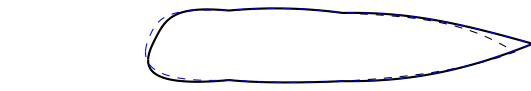
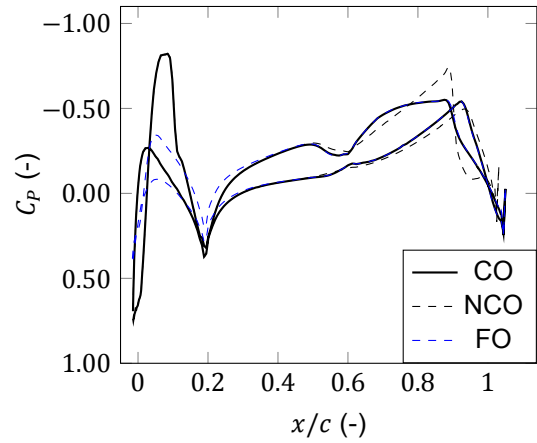
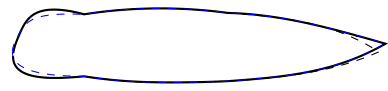


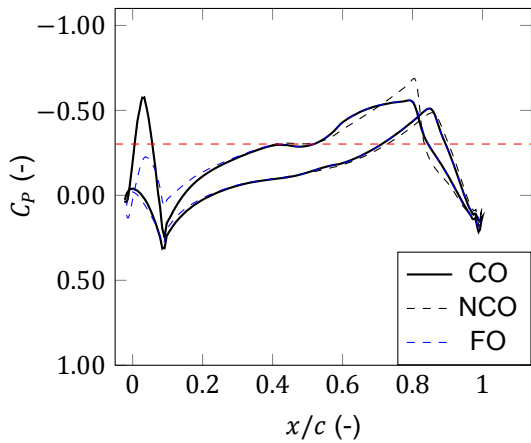
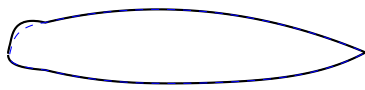
Figure A.3: Pressure distributions of UO and FO designs at different spanwise stations. Calculated at $M = 0.85$, $\alpha = 3^\circ$, $Re = 8.4 \times 10^7$. $C_p^* = -0.3$.



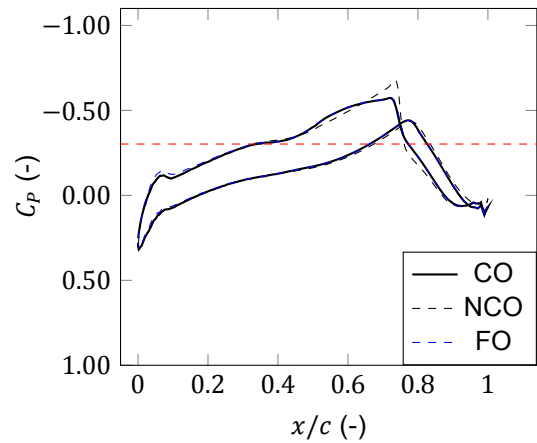
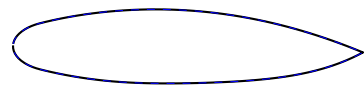
(a) Pressure distribution at $\eta=0$.



(b) Pressure distribution at $\eta=0.024$.



(c) Pressure distribution at $\eta=0.054$.



(d) Pressure distribution at $\eta=0.082$.

Figure A.4: Pressure distributions of CO, WO and NCO designs at different spanwise stations. Calculated at $M = 0.85$, $\alpha = 3^\circ$, $Re = 8.4 \times 10^7$. $C_p^* = -0.3$.

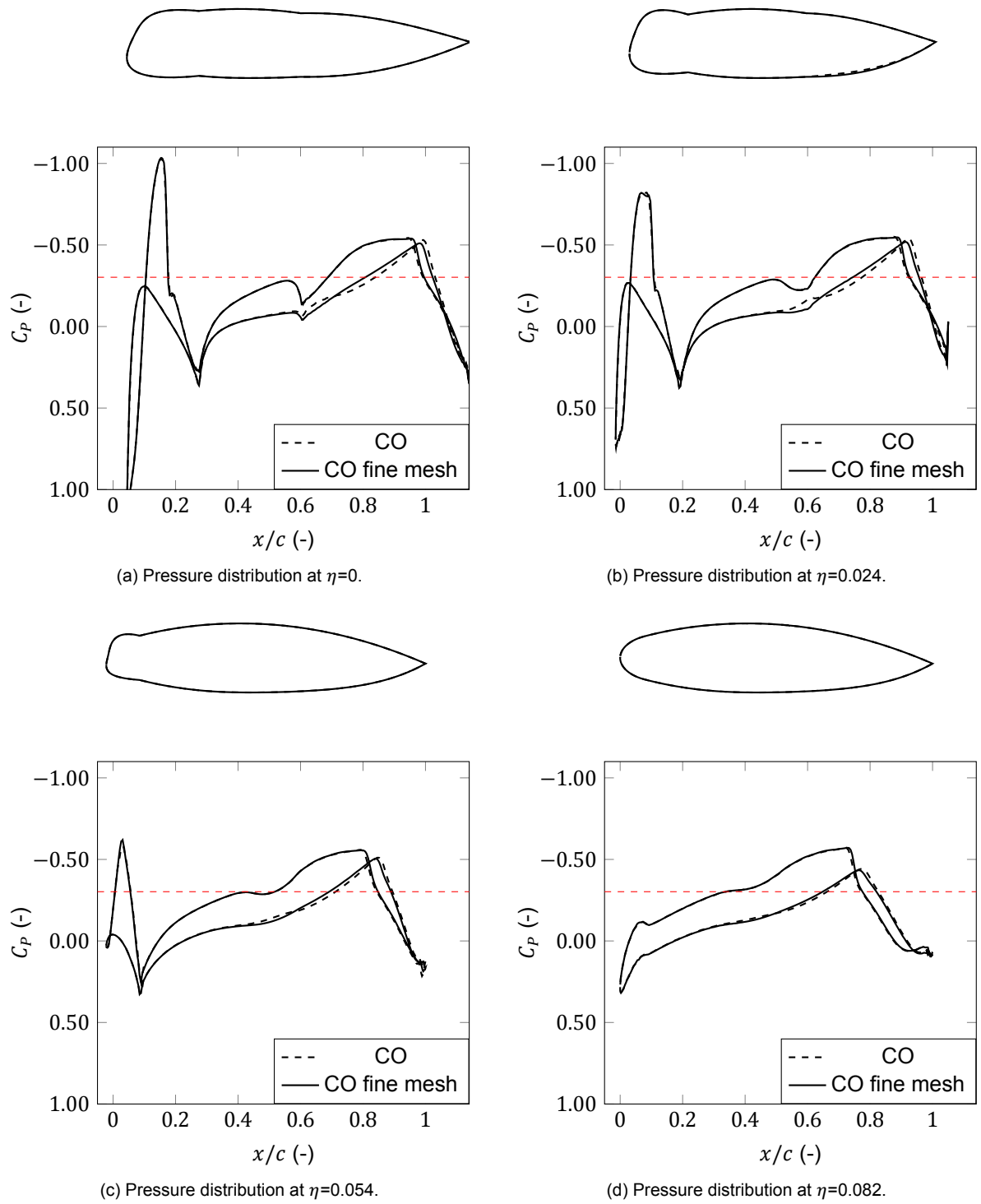


Figure A.5: Pressure distributions of CO design with comparison of coarse and fine mesh. Calculated at $M = 0.85$, $\alpha = 3^\circ$, $Re = 8.4 \times 10^7$ and $S_{ref} = 398 \text{ m}^2$. $C_p^* = -0.3$.

B

Realistic Windshields

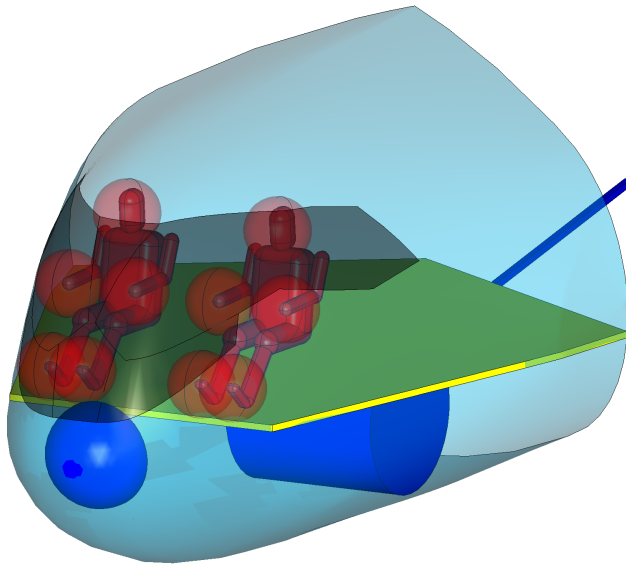


Figure B.1: Picture of UO cockpit layout with realistic windshield.

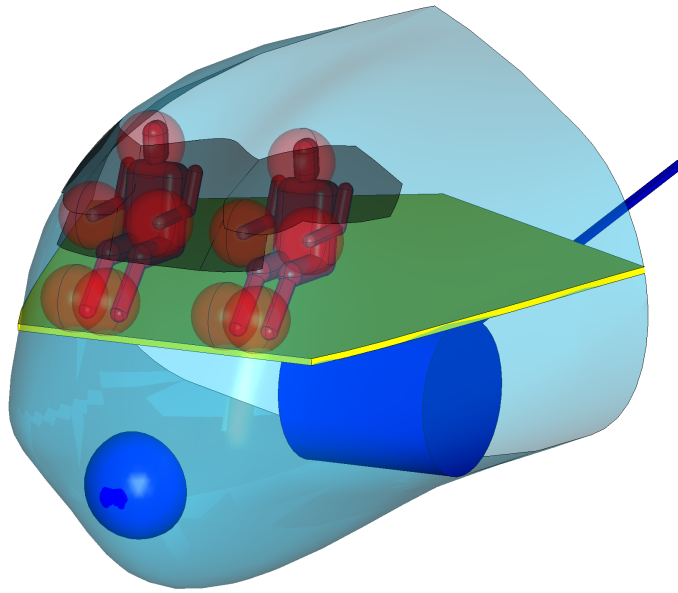


Figure B.2: Picture of WO cockpit layout with realistic windshield.

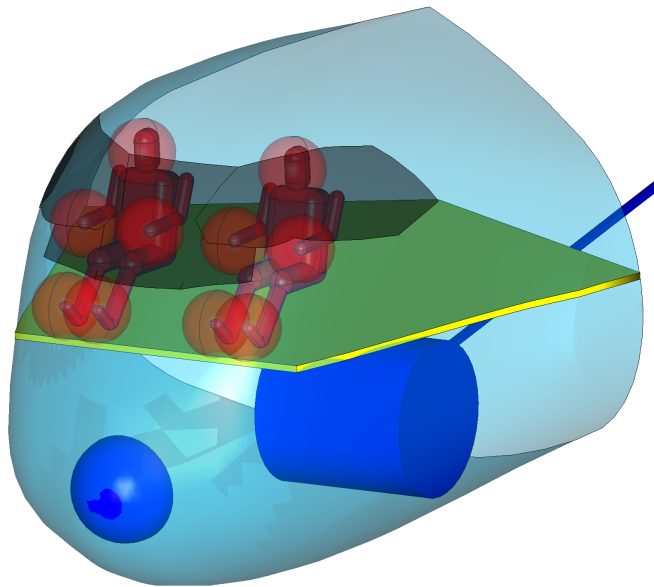


Figure B.3: Picture of NCO cockpit layout with realistic windshield.

Bibliography

- [1] R. Liebeck. Design of the blended wing body subsonic transport. *Journal of Aircraft*, 41(1), February 2004. doi: <https://doi.org/10.2514/6.2002-2>.
- [2] R. Martinez-Val, E. Pérez, J. Puertas, and J. Roas. Optimization of planform and cruise conditions of a transport flying wing. *Proceedings of the Institution of Mechanical Engineers, Part G: Journal of Aerospace Engineering*, 224(12):1243–1251, March 2010. doi: <https://doi.org/10.1243/09544100JAERO812>.
- [3] F. Faggiano, R. Vos, M. Baan, and R. van Dijk. Aerodynamic design of a flying v aircraft. In *17th AIAA Aviation Technology, Integration, and Operations Conference: 5-9 June 2017*. American Institute of Aeronautics and Astronautics Inc. (AIAA), June 2017. doi: <https://doi.org/10.2514/6.2017-3589>.
- [4] R.L. Schwader. The development of the flying wing. *Journal of Aviation/Aerospace Education & Research*, 8(1), 1997.
- [5] P. Okonkwo and H. Smith. Review of evolving trends in blended wing body aircraft design. *Progress in Aerospace Sciences*, 82, February 2016. doi: <https://doi.org/10.1016/j.paerosci.2015.12.002>.
- [6] R. Wood and S. Bauer. Flying wings / flying fuselages. In *39th AIAA Aerospace Sciences Meeting & Exhibit*. American Institute of Aeronautics and Astronautics Inc. (AIAA), January 2001. doi: <https://doi.org/10.2514/6.2001-311>.
- [7] M.A. Potsdam, M.A. Page, and R.H. Liebeck. Blended wing body analysis and design. In *15th Applied Aerodynamics Conference*. American Institute of Aeronautics and Astronautics Inc. (AIAA), June 1997. doi: <https://doi.org/10.2514/6.1997-2317>.
- [8] R. Liebeck, M. Page, and B. Rawdon. Blended-wing-body subsonic commercial transport. In *36th AIAA Aerospace Sciences Meeting and Exhibit*, 1801 Alexander Bell Drive, Suite 500, Reston, Virginia 20191-4344, 1998. American Institute of Aeronautics and Astronautics Inc. (AIAA). doi: <https://doi.org/10.2514/6.1998-438>.
- [9] A.L. Bolsunovsky, N.P. Buzoverya, B.I. Gurevich, V.E. Denisov, A.I. Dunaevsky, L.M. Shkadov, O.V. Sonin, A.J. Udzhuhu, and J.P. Zurhinh. Flying wing—problems and decisions. *Aircraft Design*, 4(4):193–219, December 2001. doi: [https://doi.org/10.1016/S1369-8869\(01\)00005-2](https://doi.org/10.1016/S1369-8869(01)00005-2).
- [10] B. Mialon, T. Fol, and C. Bonnaud. Aerodynamic optimization of subsonic flying wing configurations. In *20th AIAA Applied Aerodynamics Conference*. American Institute of Aeronautics and Astronautics Inc. (AIAA), June 2002.
- [11] M. Zhang, A. Rizzi, R. Nangia, R. Amiree, and O. Amoignon. Aerodynamic design considerations and shape optimization of flying wings in transonic flight. In *12th AIAA Aviation Technology, Integration, and Operations (ATIO) Conference and 14th AIAA/ISSM*. American Institute of Aeronautics and Astronautics Inc. (AIAA), September 2012. doi: <https://doi.org/10.2514/MATIO12>.
- [12] N. Qin, A. Vavalle, A. LeMoigne, M. Laban, K. Hackett, and P. Weinerfelt. Aerodynamic studies for blended wing body aircraft. In *9th AIAA/ISSMO Symposium on Multidisciplinary Analysis and Optimization*. American Institute of Aeronautics and Astronautics Inc. (AIAA), September 2002. doi: <https://doi.org/10.2514/6.2002-5448>.
- [13] N. Qin, A. Vavalle, A. LeMoigne, M. Laban, K. Hackett, and P. Weinerfelt. Aerodynamic considerations of blended wing body aircraft. *Progress in Aerospace Sciences*, 40(6):321–343, August 2004. doi: <https://doi.org/10.1016/j.paerosci.2004.08.0018>.

- [14] R. Martínez-Val and E. Schoep. Flying wing versus conventional transport airplane: the 300 seat case. In *22nd Congress of International Council of the Aeronautical Sciences*. International Council of the Aeronautical Sciences (ICAS), September 2000.
- [15] R. Martínez-Val, E. Pérez, P. Alfaro, and J. Pérez. Conceptual design of a medium size flying wing. *Proceedings of the Institution of Mechanical Engineers, Part G: Journal of Aerospace Engineering*, 221(1), January 2007. doi: <https://doi.org/10.1243/09544100JAERO90>.
- [16] J. Benad. The flying v: a new aircraft configuration for commercial passenger transport. In *Deutscher Luft- und Raumfahrtkongress 2015*, 2015.
- [17] M. Hillen. Parametrisation of the flying-v outer mould line. Master's thesis, TU Delft, 2020.
- [18] F. Faggiano. Aerodynamic design optimization of a flying v aircraft. Master's thesis, TU Delft, 2016.
- [19] W. Oosterom. Flying-v family design. Master's thesis, TU Delft, April 2021.
- [20] L. van der Schaft. Development, model generation and analysis of a flying v structure concept. Master's thesis, TU Delft, 2017.
- [21] B. Rubio Pascual and R. Vos. The effect of engine location on the aerodynamic efficiency of a flying-v aircraft. In *AIAA Scitech 2020 Forum*. American Institute of Aeronautics and Astronautics Inc. (AIAA), January 2020. doi: <https://doi.org/10.2514/6.2020-1954>.
- [22] B. Rubio Pascual. Engine-airframe integration for the flying v. Master's thesis, TU Delft, 2018.
- [23] A.J. Santosh. Influence of ground effect on the flying v aircraft: A numerical investigation. Master's thesis, TU Delft, February 2020.
- [24] M. Palermo and R. Vos. Experimental aerodynamic analysis of a 4.6%-scale flying-v subsonic transport. In *AIAA Scitech 2020 Forum*. American Institute of Aeronautics and Astronautics Inc. (AIAA), January 2020. doi: <https://doi.org/10.2514/6.2020-2228>.
- [25] M. Palermo. The longitudinal static stability and control characteristics of a flying v scaled model. Master's thesis, TU Delft, 2019.
- [26] R. Viet. Analysis of the flight characteristics of a highly swept cranked flying wing by means of an experimental test. Master's thesis, TU Delft, March 2019.
- [27] A. Ruiz Garcia. Aerodynamic model identification of the flying v using wind tunnel data. Master's thesis, TU Delft, July 2019.
- [28] T. Cappuyns. Handling qualities of a flying v configuration. Master's thesis, TU Delft, December 2019.
- [29] S. van Empelen. Engine integration of the flying v: Quantification of engine integration effects using wind tunnel experiments. Master's thesis, TU Delft, June 2020.
- [30] R. van der Pluijm. Cockpit design and integration into the flying v. Master's thesis, TU Delft, 2021.
- [31] D.G. Hmiel. Pilot compartment view design considerations. Technical Report AC 25.773-1, Federal Aviation Administration (FAA), January 1993.
- [32] EASA. Easy access rules for large aeroplanes (cs-25). Technical Report Amendment 27, European Aviation Safety Agency, November 2021.
- [33] R. Vos and S. Farokhi. *Introduction to transonic aerodynamics*, volume 110 of *Fluid Mechanics and Its Applications*. Springer, 2015. ISBN 978-94-017-9746-7. doi: <https://doi.org/10.1007/978-94-017-9747-4>.
- [34] D. Küchemann and J. Weber. The subsonic flow past swept wings at zero lift without and with body. Reports and Memoranda 2908, U.K. Aeronautical Research Council (ARC), March 1953.

- [35] D. Küchemann. The distribution of lift over the surface of swept wings. *The Aeronautical Quarterly*, 4(3):261–278, August 1953. doi: <https://doi.org/10.1017/S0001925900000937>.
- [36] J. Weber. The calculation of the pressure distribution over the surface of two-dimensional and swept wings with symmetrical aerofoil sections. Reports and Memoranda 2918, U.K. Aeronautical Research Council (ARC), July 1953.
- [37] E. Obert. *Aerodynamic Design of Transport Aircraft*. IOS Press, Nieuwe Hemweg 6b, 1013 BG Amsterdam, NL, 2009. ISBN 978-1-58603-970-7.
- [38] EASA. Acceptable means of compliance (amc) and guidance material (gm) to annex viii specialised operations [part-spo] of commission regulation (eu) 965/2012 on air operations. Technical report, European Aviation Safety Agency, March 2017.
- [39] EASA. Easy access rules for aerodromes (regulation (eu) no 139/2014). Technical Report Regulation (EU) No 139/2014, European Aviation Safety Agency, June 2021.
- [40] A. Ruiz García, M. Brown, D. Atherstone, N. van Arhem, and R. Vos. Aerodynamic model identification of the flying v from sub-scale flight test data. In *AIAA SciTech 2022 Forum*. American Institute of Aeronautics and Astronautics Inc. (AIAA), January 2022.
- [41] Airbus Product Safety department (GS). Are you properly seated?, 2018.
- [42] Parapy. Parapy - knowledge based engineering platform. <https://www.parapy.nl/>, 2021. Accessed on 13/11/2020.
- [43] SALOME. Salome mesh user's guide. <https://docs.salome-platform.org/7/gui/SMESH/index.html>, 2016. Accessed on 15/11/2020.
- [44] SU2. Su2 - multiphysics simulation and design software 2020. <https://su2code.github.io/>, 2020. Accessed on 04/12/2020.
- [45] B.M. Kulfan. Universal parametric geometry representation method. *Journal of Aircraft*, 45(1), January 2008. doi: <https://doi.org/10.2514/1.29958>.
- [46] K. Burke, K. and Conroy, R. Horn, F. Stratton, and G. Binet. Flask-restful documentation. <https://flask-restful.readthedocs.io/en/latest/index.html>, 2020. Accessed on 17/03/2022.
- [47] The SciPy Community. Optimization and root finding. <https://docs.scipy.org/doc/scipy/reference/optimize.html>, 2022. Accessed on 17/03/2022.
- [48] J.A. Nelder and R. Mead. A simplex method for function minimization get access arrow. *The Computer Journal*, 7(4):308–313, January 1965. doi: <https://doi.org/10.1093/comjnl/7.4.308>.
- [49] J. Roskam. *Airplane Design Part III: Layout Design of Cockpit, Fuselage, Wing and Empennage: Cutaways and Inboard Profiles*. DAR Corporation, 1440 Wakarusa Drive, Suite 500, Lawrence, Kansas, 66049, 6 edition, 1986. ISBN 978-1-884885-56-3.
- [50] E. Torenbeek. *Synthesis of Subsonic Airplane Design*. Delft University Press & Martinus Nijhoff Publishers, Mijnbouwplein 11, 2628 RT Delft, Holland, 1982. ISBN 90-247-2724-3.
- [51] R. Storn and K. Price. Differential evolution - a simple and efficient adaptive scheme for global optimization over continuous spaces. *Journal of Global Optimization*, 23(1), January 1995.
- [52] R.L. Iman. *Encyclopedia of Quantitative Risk Analysis and Assessment*, chapter Latin Hypercube Sampling. John Wiley & Sons Ltd., September 2008. doi: <https://doi.org/10.1002/9780470061596.risk0299>.
- [53] K. Price, R.M. Storn, and J.A. Lampinen. *Differential evolution : a practical approach to global optimization*. Springer, Berlin, 2015.

- [54] V.V. de Melo and G.L.C. Carosio. Evaluating differential evolution with penalty function to solve constrained engineering problems. *Expert Systems with Applications*, 39(9), July 2012. doi: <https://doi.org/10.1016/j.eswa.2012.01.123>.
- [55] Z. Michalewicz and M. Schoenauer. evolutionary algorithms for constrained parameter optimization problems. evolutionary computation. *Evolutionary Computation*, 4(1), March 1996. doi: <https://doi.org/10.1162/evco.1996.4.1.1>.
- [56] P.R. Spalart and S.R. Allmaras. A one-equation turbulence model for aerodynamic flows. *La Recherche Aéronautique*, (1), 1994. doi: <https://doi.org/10.2514/6.1992-439>.
- [57] F.R. Menter. Two-equation eddy-viscosity turbulence models for engineering applications. *AIAA Journal*, 32(8), August 1994. doi: <https://doi.org/10.2514/3.12149>.
- [58] N. van Arnhem, R. de Vries, T. Sinnige, R. Vos, and L.L.M Veldhuis. Aerodynamic performance and static stability characteristics of aircraft with tail-mounted propellers. November 2021. doi: <https://doi.org/10.2514/1.C036338>. Accepted Manuscript.
- [59] von Kármán, T. Mechanische Ähnlichkeit und turbulenz. In *Nachrichten von der Gesellschaft der Wissenschaften zu Göttingen, Fachgruppe 1 (Mathematik)*, number 5, pages 58–76, 1931.
- [60] H. Schlichting. *Boundary-Layer Theory*. McGraw-Hill Book Company, 1979. ISBN 0-07-055334-3.
- [61] V. Wilod Versprille. Aerodynamic shape optimization of a liquid-hydrogen-powered blended-wing-body. Master's thesis, TU Delft, February 2022.
- [62] V. Schmitt and F. Charpin. "pressure distributions on the onera-m6-wing at transonic mach numbers," experimental data base for computer program assessment. Technical Report AGARD-AR-138, AGARD Fluid Dynamics Panel Working Group 04, 1979.
- [63] N. Durrani and N. Qin. Comparison of rans, des and ddes results for onera m-6 wing at transonic flow speed using an in-house parallel code. In *49th AIAA Aerospace Sciences Meeting including the New Horizons Forum and Aerospace Exposition*. American Institute of Aeronautics and Astronautics Inc. (AIAA), Jaunary 2011. doi: <https://doi.org/10.2514/6.2011-190>.